TECHNISCHE UNIVERSITÄT DRESDEN

MICROFABRICATION AND DEVELOPMENT OF MULTI-SCALED METALLIC SURFACES USING DIRECT LASER INTERFERENCE PATTERNING

Der Fakultät Maschinenwesen

der

Technischen Universität Dresden

zur

Erlangung des akademischen Grades

Doktoringenieur (Dr.-Ing.)

vorgelegte Dissertation

von

M.Sc. Alfredo Ismael Aguilar Morales

geboren am 20. Juni 1986 in Mexiko Stadt

Tag der Verteidigung:

07.04.2021

Selbstständigkeitserklärung

Alfredo Ismael Aguilar Morales   Dresden, den 20.04.2020

Abstract

Bringing specific functions on surfaces by modifying their topographies is an objective of surface engineering. Surface modification up to the nanometer range can be carried out through laser surface texturing technologies such as Direct Laser Interference Patterning (DLIP) and Direct Laser Writing (DLW). Thereby, defined and well-controlled patterns in the micro- and nanometre range can be produced on several surface materials. Furthermore, specific periodic topographies can be designed and replicated over large areas, which potentially guarantee the same surface property and enable to scale up the technology in industrial processes.

This thesis aims to investigate new approaches to improve micro- and nanosurface structures fabricated by DLIP and DLW on metals. DLIP experiments are carried out using the two-beam configuration either by infrared nano- or picosecond laser sources. In order to extend the opportunities in the enhancement of surface properties, the microfabrication of topographies with repetitive distances ranging from 0.2 µm up to 7.2 µm is explored. Subsequently, the impact of DLIP process parameters such as laser fluence, pulse-to-pulse overlap, hatch distance and spatial period, on the surface texture homogeneity is investigated. Thereby, a quantitative measurement scheme based on established parameters including mean structure height, standard deviation and kurtosis is introduced. Moreover, the fabrication of hierarchical line- and pillar-like microstructures using picosecond DLIP is investigated as a function of number of pulses and laser fluence. In addition to the microstructures that correspond to the interference patterns also Laser Induced Periodic Surface Structures (LIPSS) are simultaneously produced which results in hierarchical micro- and nanostructures. In the context of multi-scaled microstructures, DLW is employed to produce micro-cells ranging from 17 µm up to 50 µm. Afterwards, picosecond DLIP is used to fabricate micro- and nanostructures on the DLW micro-cells. The obtained topography consists of multi-scaled hierarchical micro- and nanosurface structures. In order to improve the throughputs in the DLIP process, an analytical ablation model is developed, it allows predicting the resulted microstructure depth in terms of DLIP process parameters. Calculated depths are supported with experimental results, showing a good agreement with the model. Furthermore, wetting assessment on pillar-like structures is carried out as a function of Filling Factor and the combination of hierarchical and single-scale structures. Thereby, a hydrophobizing agent is applied on the hierarchical DLIP structures in order to enhance the static water contact angles up to values of $152° \pm 2°$ and to decrease the contact angle hysteresis to values as low as $4° \pm 2°$. The optimised superhydrophobic pillar-like structures with spatial period of 5.20 µm are fabricated on the surface of a large aircraft part. In this framework, the possible impact of DLIP microstructures on fatigue properties for long term stress is investigated. Lastly, pillar-like structures show in the boundary lubricated regime a friction coefficient reduction of about 40 % compare to unstructured surfaces. Thus, the micro-pillars are considered as promising and feasible structures for surface functionalisation on metals.

Kurzfassung

Die Kontrolle physikalischer Phänomene auf Oberflächen durch bestimmte Topographien ist eines der Ziele oberflächentechnischer Verfahren. Die Oberflächentopographie kann durch oberflächenmodifizierende Verfahren wie Direkte Laserinterferenzstrukturieren (DLIP) und das Direkte Laserschreiben (DLW) verändert werden. Dadurch können definierte und kontrollierte Mikro- und Nanostrukturen auf verschiedenen Materialien erzeugt werden. Darüber hinaus können spezifische Topographien entworfen und großflächig nachgebildet werden, welche die gleichen Oberflächeneigenschaft gewährleisten können.

Diese Arbeit schlägt neue Ansätze zur Verbesserung der Mikro- und Nano-Oberflächenstrukturen vor, die durch DLIP auf Metalloberflächen erzeugt werden. DLIP Experimente werden in der Zweistrahlkonfiguration entweder mit infraroten Nano- oder Pikosekundenlasern durchgeführt. Damit werden die Möglichkeiten zur Verbesserung und Kontrolle von Oberflächeneigenschaften durch die Mikrofertigung mit Strukturperioden von 0,2 μm bis 7,2 μm erweitert. Anschließend wird die Homogenität der Oberflächentextur auf Basis der Pulsverteilung und der Laserparameter optimiert. Ein quantitatives Messschema der Homogenität, das auf etablierten Parametern wie mittlere Strukturhöhe, seiner Standardabweichung und Kurtosis basiert, wird vorgestellt. Darüber hinaus wird die Herstellung hierarchischer linien- und säulenartiger Mikrostrukturen mittels DLIP in Abhängigkeit von der Anzahl der Pulse und der Fluenz untersucht. Zusätzlich zu den Mikrostrukturen, die der Interferenzverteilung entsprechen, wurden gleichzeitig laserinduzierte periodische Oberflächenstrukturen (LIPSS) erzeugt, die zu hierarchischen Mikro- und Nanostrukturen führen. Überdies wird als weitere Technologie das DLW eingesetzt, um Mikrozellen im Bereich von 17 μm bis 50 μm zu generieren. Anschließen werden Mikro- und Nanostrukturen mittels DLIP auf den Mikrozellen hergestellt. Die finale Topographie besteht aus multiskaligen hierarchischen Mikro- und Nanostrukturen. Um den Durchsatz des DLIP-Verfahrens zu verbessern, wird ein Ablationsmodell entwickelt und mit experimentellen Daten verifiziert. Das Modell ermöglicht die Berechnung von Strukturtiefe in Abhängigkeit von optimalen Laserprozessparametern. Darüber hinaus wird die Benetzbarkeit auf den Mikrosäulen im Rahmen des Füllfaktors und der Kombination von hierarschischen und einskalen Strukturen ausgewertet. Dazu wird ein hydrophobes Lösungsmittel auf die hierarchischen Strukturen aufgetragen, um den Wasserkontaktwinkel auf bis zu 152 ° ± 2 ° und die Kontaktwinkelhysterese von 4 ° ± 2 ° zu erreichen. Mikrosäulen mit einer Periode von 5,20 μm werden auf einer Flugzeugtragfläche hergestellt. Auf diese Weise wird der mögliche Einfluss von Mikrostrukturen auf die Ermüdungseigenschaften untersucht. Schließlich werden Mikrosäulen mit ca. 40 % geringeren Reibungskoeffizienten als die Referenz in einem grenzflächengeschmierten Bereich getestet. Zusammenfassend kann ausgesagt werden, dass die durch DLIP erzeugten Mikrosäulen eine vielversprechende und gut realisierbare Struktur für die Oberflächenfunktionalisierung von Metallen darstellen.

Acknowledgments

Undertaking this PhD has been a rewarding experience for me and it would not have been possible to do without the support and guidance that I received from many people.

Firstly, I would like to express my sincere gratitude to Prof. Dr. Andrés Lasagni, for his encouragement and his guidance throughout this work. Without his supervision and constant feedback this PhD would not have been achievable.

I would like to express my gratefulness to my parents, Camilo Aguilar Nicolas and Estela Morales Cardenas for their unconditional love and support along my life.

I am also grateful to my family members and friends who have supported me along the way. In special to my wife, Raquel Martinez, who supported me throughout writing this work. My deep appreciation goes out to my brother and sister, Ivan Aguilar and Nayeli Aguilar, who I am thankful for always be there.

During the development of this investigation I had the opportunity of working with engaged scientists. I am thankful with Dr. Sabri Alamri for the support of fruitful discussions about the topics investigated. A special mention and thanks to Dr. Tim Kunze their professional feedback during the data analysis has made an invaluable contribution towards my PhD. I also appreciate the comments of Dr. Marcos Soldera which help to improve the content of this work. With a special mention and thanks to Dr. Bogdan Voisat for his support and accurate contribution. I want to thank to all my colleagues form the TU and IWS for the good times in the labs.

Symbols and abbreviations

Symbol	Description
α	Absorption coefficient
Θ	Angle of incidence between the normal and the laser beam or Young´s intrinsic angle
Θ_w	Apparent contact angle
λ	Wavelength
λ_{th}	Thermal conductivity
Λ	Spatial period
ρ	Material density
τ	Pulse duration
τ_R	Time required for a chemical reaction to occur
τ_T	Relaxation time
δ	Optical penetration depth
φ	Phase difference between two beams
$\varnothing$	Diameter of the laser interference area
ω	Angular frequency or radius of the interference area
C_p	Specific heat capacity
D	Mean structure depth
E	Electric field
E_0	Amplitude of the electric filed,
$Err\%$	Relative error
$Err\Lambda\ \%$	Relative error correlated to the DLIP periodic structure
f	Repetition rate
f_s	Liquid-solid contact fraction
F	Laser fluence
F_{th}	Laser fluence threshold
F_0	Laser peak fluence

h	Hatch distance
k	Extinction coefficient or Propagation constant
L	Ablated structure depth per pulse
m	Pulse number
n	Refractive index
N	Total number of laser pulses
p	Pulse-to-pulse distance
P_E	Pulse energy
r_{th}	Radius of the structured area
r_w	Roughness factor
R	Stress ratio
Ra	Average roughness
Rc	Mean structure height
RcΛ	Mean structure height produced by DLIP
RcMod	Mean height of second modulation
Rq	Root mean square of the absolute heights
Rku	Kurtosis
S	Incubation coefficient
Surf Err %	Surface error
t	Time
v	Speed
Zt	Heights of the *i* - profile elements

Abbreviation

AR	Aspect Ratio
CAH	Contact Angle Hysteresis
CoF	Coefficient of friction
DLIP	Direct Laser Interference Patterning
DLW	Direct Laser Writing
DOE	Diffractive Optical Element
EDX	Energy Dispersive X-ray spectroscopy
FF	Filling Factor
FFT	Fast Fourier Transform
FWHM	Full Width at Half Maximum
HSFLs	High Spatial Frequency LIPSS
IR	Infrared
LIPSS	Laser-Induced Periodic Surface Structures
LSFLs	Low Spatial Frequency LIPSS
OV	Pulse-to-pulse Overlap
SEM	Scanning Electron Microscopy
Sd	Standard deviation
SWCA	Static Water Contact Angle
UV	Ultraviolet
WCA	Water Contact Angle
WLI	White Light Interferometry
XPS	X-ray Photoelectron Spectroscopy

Content

1   Motivation

The understanding of physical phenomena on functionalised surfaces helps to develop novel devices to improve our life. In this framework, the numerous examples of hierarchical micro and nano features observed on plant and animal surfaces can be taken as inspiration since they promote the enhancement of specific functions and properties [1], [2]. Biological systems represent optimised solutions to particular environmental conditions. Subsequently, the term biomimetics, referred to the "imitation of life", has become popular in the fields of science and engineering due to the endless potential technological ideas for the improvement of surface functions [3].

The development of patterning techniques, which allow mimicking natural surfaces, has opened new prospects in surface functionalisation. For example, in the field of non-contact surface manufacturing processes, laser surface texturing techniques offer high throughput, productivity and adaptability to automation [4]. The efficiency of laser texturing is related to the single-step process, which permits producing unlimited combinations of arrangements with high processing speeds rates. Surface modification through laser-based methods has shown a considerably development, among them, Direct Laser Writing (DLW) and Direct Laser Interference Patterning (DLIP), which allows fabricating controllable topographies on different surface materials e.g. metals, polymers and ceramics.

Precisely, DLIP is based on the periodic intensity variation that occurs when two or more laser coherent beams are overlapped. This principle enables the creation of a periodic pattern which consists of minima and maxima positions of energy. As a consequence, a certain material quantity can be photo-thermally and/or photo-chemically ablated at local positions on a surface. Furthermore, DLIP allows adjusting the geometry of the produced patterns by means of tuning the laser wavelength, the number of laser beams, angles of incidence, pulse-to-pulse distance, pulse energy and/or laser polarization state. It represents an advantage over others laser-based methods and also covers the research gap of fabricating controllable and repetitive patterns in the range of 15 μm down to 200 nm by laser.

In this Ph.D. thesis, the DLIP and DLW techniques are utilised to develop and fabricate micro- and nanostructures on metals, which potentially can enhance surface properties. The main goals are to:

- Propose a quantitative scheme to assess the homogeneity of surface textures.

- Investigate the impact of the two-beam DLIP process parameters on the fabricated microstructure topography by using a picosecond laser source.

- Develop multi-scaled surface microstructures by the combination of DLW and DLIP techniques.

- Introduce an analytical model, which permits the optimisation of throughputs as a function of DLIP parameters for predetermined topographies.

- Elucidate the influence of microstructures on wetting behaviours, as well as the effects of novel geometries fabricated by DLIP on tribological and fatigue properties.

The thesis is organised as follows. Chapter 2 provides the fundamentals of laser-matter interaction, the principle of two-beam laser interference, as well as basic theory about wetting, friction and fatigue phenomena. Chapter 3 introduces the state of the art of properties of natural surfaces, the techniques used to fabricate micro- and nano-roughened surfaces, the laser surface texturing methods used to treat metals as well as their upcoming challenges. Lastly, the impact of micro- and nano-surface structures on the aforementioned phenomena is presented. Chapter 4 presents the materials used during the experiments, the description of the utilised laser setups and the characterisation methods employed to investigate the fabricated micro- and nanostructures. In chapter 5, the obtained results are discussed and analysed. The chapter is organised methodically by introducing the effects of a single-pulse nanosecond DLIP on titanium as a function of spatial period and laser fluence. Afterwards, the developed method to improve and quantify the surface homogeneity is introduced. Subsequently, the fabrication of hierarchical micro and nanostructures using picosecond DLIP on stainless steel is explored. Thereby, the control of nanostructure orientation is evidenced. Then, the fabrication of pillar-like structures which mimic the micro- and nanofeatures of leafs with superhydrophobic properties is presented. Moreover, the outcomes of the combination of DLW and DLIP technologies that permitted the fabrication of multi-scale periodic micro- and nanostructures are detailed. Finally, optimised DLIP topographies are fabricated on the surface of a large aircraft part; therewith its surface characterisation is presented. In chapter 6, the analytical laser ablation model, which describes the fabricated structure depth as a function of the picosecond DLIP process parameters, is introduced. Thereby, mathematical and experimental results are compared in order to determine the optimal DLIP parameters in terms of structuring speed. In chapter 7, the results of the surface properties correlated with wettability, friction reduction and fatigue, on topographies fabricated by DLIP are detailed and discussed. Finally, in chapter 8 the conclusions and outlook are stated.

2 Theoretical background

2.1 Laser-matter interactions

The concept of stimulated emission was introduced by A. Einstein in the 1917, he proposed that a radiation field causes an atom in the upper energy state to make a transition to the lower state at a rate proportional to the radiation density [5], to claim that Einstein almost invented the laser would be an exaggeration, but the laser´s underlying mechanism, stimulated emission of radiation, was a creation of his radiation theory [6]. It was until 1960 with the construction of the first ruby laser when the concept opened new fields of research and particularly for material processing [7]. The word laser is an acronym of Light Amplification by Stimulated Emission of Radiation. A laser consists essentially in an amplifier with a positive feedback in a gain cycle provided by stimulated emission. The basic form of a laser must include an optical resonator, an active medium, where the population inversion occurs, and a pump source, which is used to excite the active medium [4].

Light is a form of electromagnetic radiation in and around the visible region of the spectrum. For the purposes of practical laser interest, it spans the range from ultraviolet at 190 nm wavelength to the far infrared at 1 mm wavelength [8]. During the light-matter interaction, the wide-ranging optical properties observed in solid materials can be classified into a small number of general phenomena: reflection, propagation and transmission. If an incident light beam interacts on a solid, some of the light is reflected, while the rest enters the medium and propagates through it. During the propagation the absorption occurs if the light is resonant with the transition frequencies of the atoms in the medium. The absorption in a solid is quantified by its absorption coefficient (α) and it is defined as the fraction of the power absorbed in a unit length of the medium [9]. The amount of light transmitted is therefore related to the reflectivity and absorption, because only unabsorbed light will be transmitted through the medium. The reflection on a material surface is a strong function of the wavelength and it can be calculated using the Eq. 1 [4]:

$$R = \left[\frac{(1-n)^2 + k^2}{(1+n)^2 + k^2} \right] \tag{1}$$

where n and k are the refractive index and extinction coefficient, respectively.

Fig. 1 shows the reflectivity as a function of the wavelength for the specific case of iron, titanium and aluminium. The curves represent the percentage of reflected light on the material surface for a determined wavelength and for the angle of incidence of 0° respect to the normal. The optical constants n and k were taken from [10] and [11].
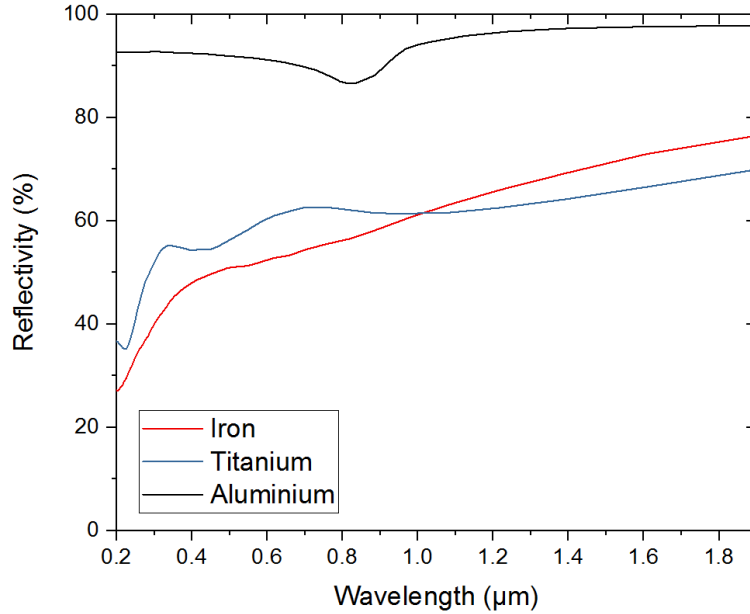
Fig.1. Reflectivity as a function of the wavelength for iron, titanium and aluminium.

In Fig. 1 can be observed that the reflectivity on aluminium is higher than 85 % for the ultraviolet, visible and short infrared ranges, while for iron and titanium it stays above 60 % for the short infrared, and decreases in the ultraviolet range to about 40 %.

Light interacts with atoms, ions or molecules only when the photon energy is close to the difference of two energy levels. In this context, it is instructive to consider an atom as consisting of a number of electrons orbiting around a nucleus. Electrons orbiting near to the nucleus are bound strongly since the Coulomb force law is obeyed. The outermost electrons are bound only weakly. As energy is added to the atom the outermost electron assumes a progressively larger orbit until, finally, sufficient energy is imparted to remove it completely from the nucleus, whereupon the atom becomes an ion. Corresponding to each orbit of the outermost electron, there is a definite energy level.

Molecules also exhibit energy levels due to electrons, but in addition, each atom can vibrate with respect to the others or rotate about a number of common axes. Both vibration and rotation give rise to energy levels [8].

In 1917 Einstein introduced A and B coefficients to describe spontaneous emission, absorption and stimulated emission. The A coefficient is defined in terms of the total rate of spontaneous emission W_{21} from an upper level 2 to a lower level 1 for a system of N_2 electrons in the upper level; this is described by Eq. 2:

$$W_{21}=A_{21}N_2 \tag{2}$$

If electrons in level 2 can decay only by radiative emission to level 1, then A_{21} must be the reciprocal of the spontaneous radiative lifetime t_{spon} of level 2, which is defined by Eq. 3:

$$A_{21}=1/t_{spon} \tag{3}$$

4

Finally, the B coefficients are defined in terms of the transition rates for absorption W_{12} and stimulated emission W_{21}, stated by Eq. 4 and Eq. 5 respectively:

$$W_{12} = B_{12} \rho_\omega N_1, \tag{4}$$

$$W_{21} = B_{21} \rho_\omega N_2, \tag{5}$$

where ρ_ω is the energy density per unit angular frequency interval in the region containing N_2 atoms in the upper level and N_1 atoms in the lower level. ρ_ω is assumed to be constant over the frequency range of significant absorption and emission between 1 and 2 transition [12]. In Fig. 2 is graphically represented the atomic processes of (a) absorption, (b) spontaneous emission and (c) stimulated emission, where the arrows represent photons and black points electrons.
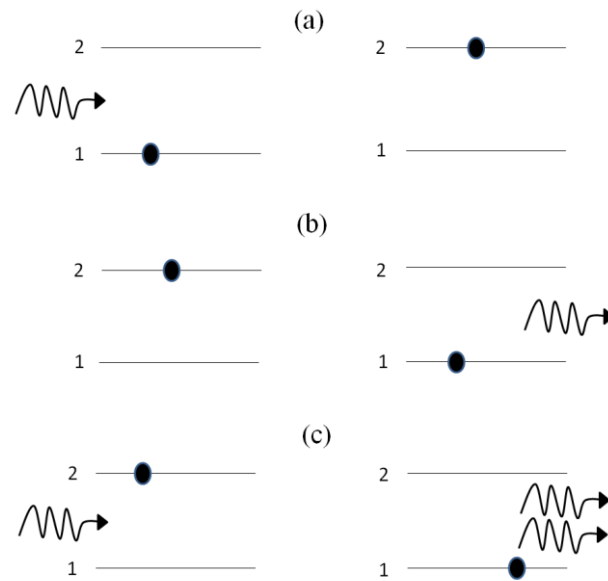
Fig.2. Schematic representation of the atomic processes: (a) absorption, (b) spontaneous emission and (c) stimulated emission.

In detail, the absorption causes an atomic electron transition from level 1 to level 2, it is represented in Fig. 2 (a). The probability of this event is given by the coefficient B_{12} (the suffix $_{12}$ means from level 1 to level 2).

For the spontaneous emission represented in Fig. 2(b), an electron is relaxed spontaneously from level 2 to level 1 emitting a photon randomly in time, phase and direction. The probability of this is given by the coefficient A_{21} (the suffix $_{21}$ means from level 2 to level 1)

Finally, in Fig. 2 (c) is represented an incident photon which stimulates the emission of a second photon causing an atomic electron transition from level 2 back to level 1. The stimulated photon has the property of being in phase with the photon that has induced the emission and therefore the radiation is temporarily coherent. The probability of this event is given by the coefficient B_{21} [8].

The laser-matter interaction on metals involves the energy transfer through the absorption of photons in a solid, which can results in melting, sublimation, ejection of atoms, shock waves, plasma

formation and its expansion. This interaction depends on the laser parameters and the material physical and chemical properties. The main laser parameters are wavelength, polarization, angle of incidence, pulse duration (τ) and fluence (F) (laser energy per area unit). The material absorption determines the ablation depth and it is in function of the laser parameters. In general, the physical mechanisms which lead to the material removal on metals can be thermal (photothermal) and non-thermal (photochemical). Material responses that exhibit both thermal and non-thermal mechanisms are typically referred to as photophysical [13].

In metals, light is almost exclusively absorbed by conduction band electrons within a layer of, typically, 10 nm. The time between electron–electron collisions is of the order of 10^{-14} to 10^{-12} s (10 fs to 1ps). Electron-phonon relaxation times, are much longer, due to the big difference between electron and ion masses [14].

Nowadays, short and ultra-short laser pulses are employed for confining high energy densities in a very short time. On metallic surfaces the importance of the pulse duration is connected with the mechanism of ablation. If nanosecond laser pulses are used to irradiate a metal surface, firstly, the laser energy deposited is transferred to free electrons [15], which leads to melting and vaporization of the material. In addition, the molten material can be ejected by means of the recoil pressure, which can become a primary factor for removing melt from the interaction zone under the regime of hydrodynamic flow [16]. Note that the vaporization of a surface requires much more energy than the melting. A main condition in a thermal process is: $\tau_T << \tau_R$, where τ_T is the relaxation time and τ_R is the time required for desorption of species from the surface, or, the time which characterises the initial step in a chemical reaction [14]. Furthermore, the dissipation time of the thermal and boiled energy is too short in comparison with pulse durations in the nanosecond range.

Moreover, the distance over which temperature changes propagate in the material in some characteristic time is determined by the thermal diffusion length (l_T). Typically, this time is considered to be the laser beam dwell time or temporal pulse width (pulse duration), in this case we can consider the thermal diffusion length as a measure of how far the energy spreads during the laser irradiation [13]. The thermal diffusion length is given by Eq. 6,

$$l_T = \sqrt{\frac{\lambda_{th}\tau}{\rho c_p}} \tag{6}$$

where τ is the pulse duration, ρ is the material density, λ_{th} is the thermal conductivity and c_p is the specific heat capacity.

As it can be inferred from Eq. 6, for a determined material the thermal diffusion length can be only shortened by reducing the pulse duration. This is the case of using ultra-short laser pulses (pico- and femtosecond lasers), where the physical mechanisms are linked with a lapse of time considerable shorter than the time required to transfer the energy between the free electrons and the lattice. This implies that when the laser pulse duration is shorter than the electron-phonon energy-transfer time,

then the electron and lattice have different temperatures, resulting in a non-thermal equilibrium state [17]. As a consequence, higher temperatures and pressures are produced. Afterwards, the target material reaches the boiling point without passing necessarily through the melting point temperature.

In addition, independently of the pulse duration, the first pulse that hits the target usually reduces the surface reflectivity [18]. Therefore, in multi-pulse irradiation, the absorptivity of the target increases with each new pulse [19]. In consequence, after each pulse a larger amount of laser energy is absorbed from the surface. That leads to more intensive surface melting, material expulsion/removal and evaporation. Thus, the morphological changes are pronounced and the concentration of oxides are commonly increased [20].

Particularly, the ablated structure depth per pulse (L) is given by Eq. 7 [21]. It is used for models which describe photochemical and photothermal ablation on several materials [22]:

$$L \approx \alpha^{-1}\ln(F/F_{th}) \tag{7}$$

where F is the laser fluence applied on the substrate and F_{th} is the ablation threshold. The inverse value of α is referred to the optical penetration depth $\delta = 1/\alpha$.

Additionally, a remarkable parameter linked with the multi-pulse ablation is the incubation coefficient (S). It has an impact on the F_{th} connected with the number of pulses (N). For example if fluences below the single-shot threshold are used, commonly, an effect of reduction in the ablation threshold with the increasing of incident laser pulses occurs [23], [24]. Thus, $S = 1$ means that incubation effects are not present and the ablation threshold is independent of N. Normally, the incubation coefficient adopts values from 0 to 1. The correlation between Fth and N is described by Eq. 8:

$$F_{th}(N) = F_{th}(1)N^{S-1} \tag{8}$$

2.2   Principle of interference

Interference phenomena occur when two or more waves overlap in space and time [25]. In order to observe interference in light waves, the light sources must be coherent, must maintain a constant phase with respect to each other and should be monochromatic (single wavelength). In a constructive interference, the amplitude of the resultant wave at a given position and time is greater than the individual wave, while in destructive interference, the resultant amplitude is less than the individual wave.

In laser material micro processing, this basic physical phenomenon can be used for producing periodic surface patterns on different materials if high-power laser systems are used. In this case, the method is called Direct Laser Interference Patterning and it permits to produce periodic patterns up to the sub-micrometer range.

The light is defined as an electromagnetic wave constitutes of electric and magnetic waves. In order to describe a monochromatic linear polarized plane wave, only the electric field (E) can be considered and it is described according to the Maxwell's theory by Eq. 9:

$$E = E_0 e^{i(kz-\omega t)},\qquad(9)$$

where E_0 is the amplitude of the electric filed, z is the coordinate in the propagation direction, t the time, ω is the angular frequency and k defined as the wave vector ($k = 2\pi/\lambda$) [9].

In the interaction of two electric fields, i.e. two laser coherent beams, the two-plane waves result in a field with different amplitude. In this case, if an evaluation along the x-axis is done, the superposition of two electric fields is given by Eq. 10:

$$E = (E_1 e^{i(kx\,sin\theta)} + E_2 e^{-i(kx\,sin\theta)})e^{-i(\omega t)},\qquad(10)$$

where Θ is the angle of incidence between the normal and the beam. Here, Θ is assumed to be equal for both beams. Besides, the two vectors are real and are polarized along the z-axes. The polarization is defined as the oscillation of the electric field in a determined plane. A substantial parameter is the spatial intensity distribution, given by Eq. 11:

$$I = \frac{c\varepsilon_0}{2}|E|^2,\qquad(11)$$

where c is the speed of light in vacuum and ε_0 the permittivity. Thus, when two beams interfere coherently, the intensity distribution of the electric field can be expressed according to Eq. 12 [26]:

$$I = I_1 + I_2 + 2\sqrt{I_1 I_2} \cdot \cos(\varphi)\qquad(12)$$

where φ is the phase difference between the two beams at that particular place. The phase difference is due to the angle between the two coherent laser beams. The two laser beams will only interfere over a distance where their phase-relation is constant [26]. This distance is called coherence length and depends on the bandwidth of the laser. Therefore, if the intensities are equal, $I_1=I_2$, and the phase difference equal to zero, the expression is simplified as shown in Eq.13 [27]:

$$I = 2I_0[1 + cos(\varphi)].\qquad(13)$$

Thus, the intensity I(x) is written as follows:

$$I(x) = 2C\varepsilon_0 E_0^2 cos^2(kx\sin\theta)\qquad(14)$$

Fig. 3 (a) shows the schematic representation of two-beam interference phenomenon. The energy density varies along the x-axis with a repetitive distance between each feature which is called spatial period (Λ). The intensity distribution of the pattern is represented in Fig. 3 (b).
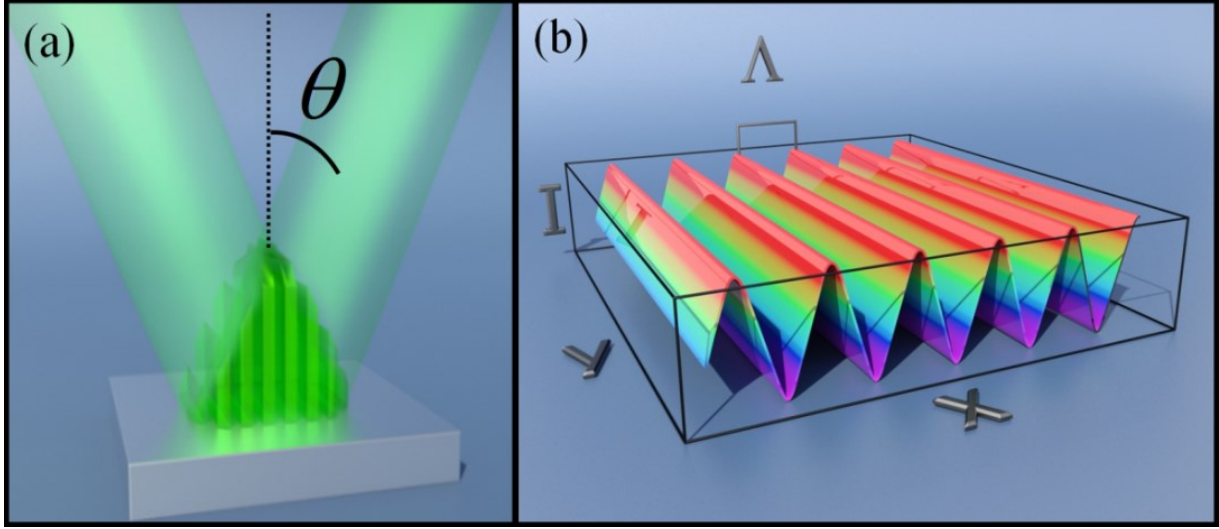
Fig.3. (a) Representation of two laser beams interfering on a surface, (b) line-like intensity distribution resulted with a determined spatial period (Λ) between two interference maxima positions [28].

Specifically, for a two-beam configuration a line-like pattern is created, the spatial period is given by Eq. 15:

$$\Lambda = \frac{\lambda}{2\sin(\theta)} \tag{15}$$

where λ is the wavelength of the laser beams. Accordingly, the spatial period can be controlled by varying Θ.

2.3   Wetting on solid surfaces

Self-cleaning and self-repellent surfaces have gained great interest in many different areas of everyday life, pharmacology, biotechnology and medicine. Their advantages in all these areas are questionless due the constantly interaction between surfaces, which has a strong connection with the energy consumption, tool wear, bacteria proliferation and finger print phenomenon. The main association between surface roughness and water-repellence were explained by Wenzel (1936) [29] as well as Cassie and Baxter (1944) [30]. The Wenzel model describes a wetting regime in which the liquid penetrates into the roughened surface (complete contact between liquid and solid surface always exists), whereas, in the Cassie-Baxter model air is trapped between the solid surface and liquid, creating a favourable condition for rolling droplets [31]. Specifically a superhydrophobic behaviour, that is, the capacity to repel water, is typically achieved if the Static Water Contact Angle (SWCA) exceeds 150°. In addition, the Contact Angle Hysteresis (CAH) also has to be considered, which is defined as the difference between advancing and receding contact angles (also known as the dynamic contact angle). Therefore, if the CAH values are below 10 ° and the SWCA above 150 ° the surface is considered superhydrophobic [32].

The basic effect of surface roughness on the contact angle is described by Wenzel´s equation; it is given by Eq. 16,

$$\cos \Theta_w = r_w \cos \Theta \tag{16}$$

which states that the apparent contact angle (Θ_w) of the droplet is related with Young´s intrinsic angle (Θ) on an ideal surface.

An ideal surface is smooth, homogeneous, rigid, insoluble and non/reactive with the contacting liquid. A value of r_w corresponds to the "roughness factor", given by the ratio of rough to planar surface areas. Thus, in the Wenzel´s equation is stated that wettability is improved by roughness for a hydrophilic surface ($\Theta_w < \Theta$ for $\Theta < 90$ °), but becomes worse for a hydrophobic one ($\Theta_w > \Theta$ for $\Theta > 90$ °). Different to the Wenzel model, the Cassie and Baxter model predicts the possibility of an apparent contact angle (Θ_w) larger than 90 ° even with an intrinsic contact angle < 90 ° which means that hydrophilic surfaces can be topographically modified to achieve a (super)hydrophobic state, if the topography results in trapped air. The Cassie and Baxter state is described by Eq. 17:

$$\cos \Theta_w = f_s (1 + \cos \Theta) - 1, \tag{17}$$

where f_s is the liquid-solid contact fraction (or solid fraction).

Consequently, the increase of Θ_w can be quantitatively explored as a function of the f_s values. To describe a superhydrophobic situation the rough surface can simply be assumed to be a surface composed of air pockets where f_s tend to zero and Θ_w will thus tend to 180 ° [33].

In addition, depending on the complexity of the topography, different wettability states can be exhibited, a distinguished one is the rose petal effect [34], [35], it is correlated with a high level of adhesion between the surface and the droplet, which leads to high SWCA and high CAH values due to a mixed stated wetting regime. In this regime a high CAH is measured if the water penetrates into the microstructure but no into the nanostructures and therefore a high solid-water adhesion occurs [36].

Finally, it is important to mention the impact of the surface energy on surface wetting. In a bulk material, chemical bonds exist between the molecules and certain energy has to be applied in order to break them. Molecules which do not form bonds at the surface have higher energy that those that form the bonds, this additional higher energy is called surface or interface free energy and is measured in the SI using J/cm^2 or N/m [37]. For the superhydrophobic state, the dry area should have lower surface energy than the wet area. The shape of a droplet on the superhydrophobic surface spontaneously assumes a more spherical shape to minimize its energy. Thus, the liquid-air interface is promoted. Therefore, the surface energy is a factor that cannot be ruled out in the wetting of solid surfaces.

2.4 Introduction to friction

Friction is the resistance to motion during sliding or rolling, that is experienced when one solid body moves tangentially over another with which it is in contact [38]. The develop of fundamental knowledge of friction, adhesion, wear, indentation and lubrication processes is addressed by the understanding of mechanisms and dynamics of interactions ranging from the atomic over the micro- up to macroscale of two contacting solids. The study of the interaction between surfaces in contact is referred to tribology [39].

Tribology is crucial to modern machinery which uses sliding and rolling surfaces, since ~ 20 % of the total energy production in the world is used to overcome friction [40], [41]. In general, there are two fields of study, the macrotribology, where the tests are conducted on components with relatively large mass under heavily loaded conditions. In these tests, wear is unavoidable and the bulk properties dominate the tribological performance. And the micro/nanotribology, where the tests are carry out on components with relatively small mass under lightly loaded conditions, in this situation, negligible wear occurs and the surface properties dominate the tribological performance. Hence, micro and nanotribological techniques are ideal ways to study the friction and wear processes of micro- and nanostructures [38].

Surface topography has a remarkable impact on friction in both dry and lubricating conditions [42]. Thus, using micro- and nanoscale topographies has been intensively investigated due to the fact that it offers interesting possibilities for friction reduction [43], [44]. For instance, the dimple surface distribution of a golf ball highly impacts the performance of the lift coefficient and drag effects [45]. Another example is the irregularities on the surfaces of rotary-shaft seals which are able of producing hydrodynamic pressure and therefore create a load carrying capacity [46]. As a consequence, micro and nanosurface geometries are the standpoint for control of tribological phenomena connected with the improving of load capacity, wear resistances, lubrication lifetime and reduction of friction.

2.5 Introduction to fatigue

In contrast to other types of material failures e.g. corrosion, wear, etc., fatigue failures occur often without prior indication of deteriorated performance of the structure. In this context, cyclic loaded parts can fail at stress amplitudes significantly below the static mechanical properties. The reason for this behaviour is connected with excess of stress. If the local mechanical capacity of a material is exceeded, crack initiation can occur. Located excess of stress can be geometrical dependent, e.g. notches, surface roughness or radius transitions, or material dependent, e.g. precipitates, phase or grain boundaries and pores. In consequence, due to the cycling loading, the crack propagates in the material with increasing cycles [47]. Therefore, since the fatigue behaviour is

strongly dependent on the surface characteristics, conventional surface modification methods, such a plasma treatment, thermal oxidation, etc., can reduce the fatigue strength and decrease the performance of vital applications, for instance, prostheses or fuselage of airplanes.

Fatigue tests are often carried out by the cyclic loading of a specimen at constant stress amplitudes and mean load. Subsequently, the amplitude is express as the stress ratio (R) value, which is the minimum peak load divided by the maximum peak load (R= $\sigma_{min}/\sigma_{max}$).

Conventionally, tests are carried out until an estimated amount of cycles or the specimen failure. The correlation between stress amplitude and reached cycles can be used to determine the stress-cycle curve. In this case, the establishment of a stress-cycle curve requires a high amount of specimens to be statistically validated [48].

A convenient approach for small sample quantities or preliminary investigation is the load increasing testing method. Thereby, the specimen is tested at a constant stress amplitude and mean load until an estimated amount of cycles or specimen failure is achieved. In the case of reaching the defined amount of cycles and the failure did not occur, the load is increased and the test is repeated in a new trial until the fracture occurs. The reached value allows setting the limits for the consecutive set of experiments. Moreover, it has to be mentioned, that the material properties can be affected by previous trials, e.g. strain hardening or weakening [49].

3 State of the art

3.1 Properties of natural surfaces

The study of surface interactions represents an important topic in the fields of tribology, wettability and adhesion. Regardless the length scale is essential to know that the basis of several interactions is located at the microscopic level. In this framework, nature has been able to develop effective and efficient biological topographies, which base their functions on the arrangement of surface structures with features sizes in the micro- and nanometre range. Some well-known examples include the hierarchical microstructures observed on leafs of the Nelumbo nucifera and Colocasia esculenta [50], [51], they are correlated with the self-cleaning functionality which in turn is based on the water-repellent property. Moreover, this property is not restricted to plants, it can be also observed on insect wings [52]. Other surface biological properties include the shark skin, which can suppress turbulence while moving underwater [53], [54]; the gecko foot, which has very high and adaptive adhesion; the water strider leg, which stays dry on top of a pool water; the darkling beetle, which collects dew using hydrophilic microspots; the sand skink, which reduces friction using nanothresholds [1], [37]; the moth-eyes with the antireflection function [55]; the rice leafs with anisotropy wetting properties [56] and the springtail skin with antiadhesive surface patterns which exhibit repellence to bacterial or fungal contamination [57], [58].

In general, the water repellence of leaves of plants is based on the micro and nanostructures together with a low surface free energy wax crystals [59], [60]. Precisely, the leaves with superhydrophobic properties possess a surface arrangement which is subdivided into a primary topography, with feature sizes in the range of 11 to 50 μm [61], [62], and a secondary one associated with an epicuticle wax layer, for instance on the lotus leaf, with sizes around 0.3 up to 1.0 μm and diameters of ~ 80 up to 120 nm [59], [63]. Thus, these surfaces are characterised by at least two-level surface structures, typically having pillars-like features in the microscale and hair-like structures in the nanoscale. Moreover, experimental studies carried out on the lotus leaf showed the importance of the nanoscaled hair-like structures, which were responsible of a SWCA increase from 126 ° to 142 ° [64].

In the field of tribology, studies demonstrated that hydrophobic surfaces exhibit lower drag [54], [65]. For example, the sharkskin recently has attracted attention due to the optimal hydrodynamic parameters which influence the drag reduction efficiency. In general, the bio-inspired shark skin can be approached in two kind of interfaces the solid-liquid and the gas-solid. From this viewpoint, the two interesting factors leading the high drag reduction of a superhydrophobic surface consist on the micro/nano hierarchical structures and on the promotion of gas-liquid interfaces. It leads to air bubbles in the cavity which in dynamic conditions are not steady and they can revolve at certain speed, as a result the function of bearing is provided and the reduction of the drag force on the surface is

promoted. It means that the gas-liquid interfaces can offer a larger drag reduction, compare with the created by a solid-liquid interface [66].

3.2   Texturing techniques for creating micro/nanoroughness

The techniques used to fabricate micro- and nanostructures, such as lithography, etching, deposition and templating represent routes to modify properties on material surfaces. An overview of the fabrication techniques is presented in Fig. 4. These techniques are used in areas such as photonics [67], plasmonics [68], optofluidics [69], stealth technology [70], solar energy absorbers [71], biomaterials [72], friction, wear [46], air retention and condensation [73].

Fabrication techniques for creating micro/nanoroughness

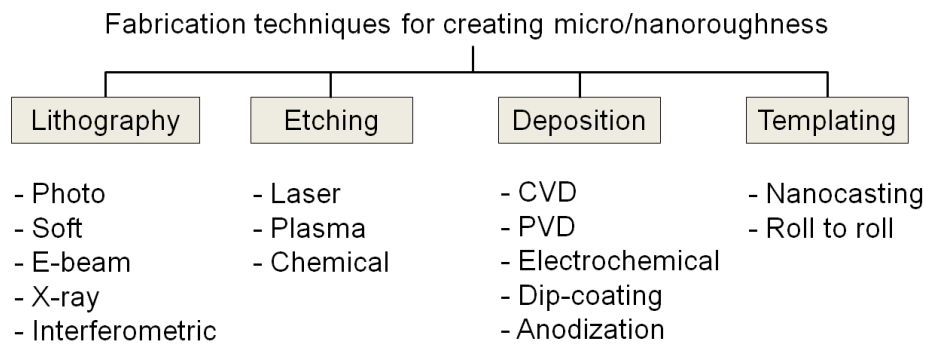| Lithography	Etching	Deposition	Templating
- Photo	- Laser	- CVD	- Nanocasting
- Soft	- Plasma	- PVD	- Roll to roll
- E-beam	- Chemical	- Electrochemical	
- X-ray		- Dip-coating	
- Interferometric		- Anodization	

Fig.4. Typical methods to fabricate micro/nano roughened surfaces.

Lithography is a well-established technique which can be divided in sub-techniques including photolithography, soft lithography, e-beam lithography [74], X-ray lithography and interferometric lithography [75]. In the conventional photolithography process, a light-sensitive polymer (or film of sensitive photoresist) and a photomask are used to form the desired pattern after UV (ultraviolet) illumination. For the soft lithography, elements like an elastomeric stamp (relatively soft polymer stamp), mold and/or mask allows transferring patterns up to the nanometre scale. Electron beam lithography uses a focused electron beams which enable to discard the use of a mask. X-ray lithography lays its difference on the type of source radiation. Lastly, the interferometric lithography technique is referred to a maskless exposure of a photoresist layer that uses two or more light beams.

Regarding the efficiency of large-area patterning, the e-beam lithography is not suitable due to the low exposure speed [76]. On the other hand, the interferometric lithography has a high large area capability, however it is more restricted in the types of patterns [26]. In general, lithography methods are able to fabricate well-defined microstructures and can reproduce many copies of the same pattern, however with relative high costs [77] and various step processes: preparation, exposition, developing, etching, cleaning.

Etching techniques include laser, plasma and chemical methods, which can increase the surface roughness [78]. For the plasma treatment the source gasses are require to react efficiently with

the materials. The process conditions must be controlled which means that this method requires a lot of effort to produce surface patterns with hierarchical roughness on large areas [79]. A simple surface roughening method is the chemical etching, which consist basically in immersing the substrates in an etchant. For crystalline metals the large numbers of dislocation defects are prone to be dissolved first by chemical etchants. In this case, the increased surface roughness is depending on the etching time. This route demonstrated that etched metallic surfaces can exhibit superhydrophobicity after the treatment with fluoroalkylsilane [80].

Typical deposition methods include Chemical Vapour Deposition (CVD), Physical Vapour Deposition (PVD) and electrochemical deposition. CVD techniques refer to exposing the selected substrate to a gaseous precursor in order to deposit a thin film. There are different variables on the process based on the pressure range at which is conducted, the type of reactants and whether some method to activate the reaction is used. The PVD techniques refer to vacuum deposition methods that produce the source gas by evaporation, sputtering or a related non chemical method. In general, these methods transfer kinetic energy to atoms in a solid or liquid which is sufficient to overcome their binding energy [81]. The electrochemical deposition process can be used to deposit films of a solid metal or its oxide onto electrically conductive substrates [82]. As important factor the morphology depends on the initial interelectrode distance and the voltage imposed [83]. This technique is extensively used in the fabrication of micro- nano hierarchical structures on metals due to advantages as simplicity and low-cost. It can achieves micro pores, e.g. on copper, with diameters varying from 10 µm to 100 µm cover with nanodendritic substructures [84].

Another deposition technique is the dip-coating method which consists in a substrate immersion in a solution in order to cover the surfaces with a slurry, where the withdrawing is carried out at a constant speed, this parameter determines the thickness of the coating. On polycrystalline alumina substrates, superhydrophobic surfaces can be produced by dip-coating them in a slurry containing nano-silica spheres. It is pointed out that after reacting the surface with fluoroalkytrischlorosilane the hydrophobicity increase with decreasing the area fraction of spheres [85], which supports the Cassie Baxter equation.

Anodization is considered to be a method in that nanofacets are formed on e.g. a bulk aluminium surface from the top down that induces direct the formation of an anodic oxide from the bottom. Anodizing operates under the same principle as electropolishing except that film growth is favoured instead of film dissolution [86]. Thus, enhanced functions can be attained, for instance, the creation of nanotubes on Ti6Al4V by anodization proved better performance on wear and corrosion resist [87].

Templating or transfer processes involves a template master, then molding the replica and removing the template. In this context, a copy of any surface can be made by filling it with a soft material, hardening it and removing the original. Copying natural surfaces such as leaves, insects, skin

of animals can be precisely achieved using these techniques. For instance, nanocasting method allowed obtaining a negative PDMS template using the lotus leaf as an original template. It was used to make a positive template, which results in a replica of the original lotus leaf. [88]. The feature size limitation that can be transferred is about 20 nm, in this length scale the operator requires to be very careful to avoid the damage on the replica and the template. Furthermore, an excessively complex micro- nanostructure can be challenging due to the peeling procedure.

A somewhat easier version of the nanocasting method is the nano-imprinting lithography (NIL). During the nanoimprinting process, a mold is pressed into a thin thermoplastic polymer film on a substrate that is heated above its glass transition temperature (a temperature at which it becomes soft). Above that temperature the polymer behaves as a viscous liquid and can flow under a pressure, thereby conforming to the mold [89]. Another type of this technology is the step and flash imprint lithography. It uses a substrate coated with a UV-curable resist which is cured by exposure to UV light after the mold is pressed into substrate. The resist is heated to above its glass transition temperature and the hard mold is pressed into the soft plastic. Afterwards, the pattern is hardened before the stamp is removed. The surface of the mold is covered with a release agent that allows the mold to be removed from the imprinted surface after the resist is cured. Thus, surface structures with resolvable features down to 5 nm can be produced [86].

In terms of productivity, the roll to roll processes can be really effective for mass production, they include the R2R (roll-to-roll) hot embossing and UV-based (R2R-UV-NIL), the main parameters of the process are embossing pressure, roller temperature, substrate preheating and roller speed [90], they can achieve speeds up to 20 m/min with high quality on the transferred microstructures [91]. These processes permit upscaling the fabrication of micro- and nanometre features sizes on flexible substrates as polymer foils [92].

Finally, it is worth to mention that the common feature of lithography and templating is embodied; they usually need a master piece and a replica substrate [82]. Therefore, those technologies are not necessarily independent on each other, but to the contrary, they can be used as a combination in order to enhance surface material properties.

3.3   Surface microstructuring of metals using pulsed laser sources

In this section are introduced the laser-based methods commonly used for structuring metallic surfaces, among them the Direct Laser Interference Patterning (DLIP), Direct Laser Writing (DLW) and Laser-Induce Periodic Surface Structures (LIPSS).

3.3.1 Direct Laser Writing

Direct Laser Writing (DLW) is an effective method for the fabrication of surface microstructures in a single-step process for a large range of applications [93], for instance, generation of high and low friction surfaces [94], wear reduction [95] and colour marking [96]. Novel microstructures can be obtained by controlling the laser intensity, polarization and incident angle of the laser beam [97]. Consequently, advanced surfaces morphologies such as microcells [98] and broccoli-like microstructures [99] can be achieved, which potentially can enhance surface functionalities related with wettability [35] and tribology [66]. Specifically, if nanosecond-pulsed laser sources are used to texture metallic surfaces, different thermal effects take place, resulting for instance in recrystallization, melting and/or evaporation of surface material [100]. The photothermal ablation on metals leads to redeposited material on the surface due to the recoil pressure of the vaporized phase [22]. This limits the smallest achievable feature sizes and especially the structure quality. Commonly, the microstructures fabricated by DLW are produced with laser systems having a Gaussian beam shape (TEM00 beam profile), where the parameter M^2 (beam quality factor) and the numerical aperture of the focal lens, influence the lateral resolution of surface features fabricated [101]. The resolution is usually limited to about 50 μm down to 10 μm [98], [102]–[104].

For the case of ultrafast laser sources (pico- and femtosecond laser pulses) the character for a precise micro processing of metals was demonstrated, in special using femtosecond laser pulses since the heat-affected zones are minimized [22]. Using the laser sources in these ultra-short time regimes interesting topographies can be fabricated, for instance, two-scale micro-nano-bumps on steel [105] and on Ti6Al4V [106] or dual scale hierarchical structures [107]. Furthermore, the capability of these laser sources have been effectively addressed in fields of antireflective surfaces [108] and superhydrophobic hierarchical structures [109].

3.3.2 Direct Laser Interference Patterning

Direct Laser Interference Patterning (DLIP) is an effective technique for texturing materials down to the sub-micrometer level, with high quality and throughput [110], [111]. The DLIP process makes use of interference patterns that are created by overlapping two or more high coherent laser beams and thereby, producing a periodic variation of the laser intensity. Thus, the material surface can be locally ablated at the interference maxima positions either by photo-thermal or photo-chemical processes, depending on the material properties, laser wavelength and pulse duration of the laser system. The versatility of the method in terms of pattern geometries has been studied by numerical simulations [112], [113]. The periodic patterns that can be produced are in function of the number of laser beams used, the laser light polarization, intensity and incident angles for each sub-beam. Thus, a controllable and predictable geometry pattern can be transferred on a surface. Furthermore, the

periodic surface patterns are produced in a one-step process. These characteristics allow DLIP to directly process different metallic surfaces for a wide number of investigations. For instance, the correlation between coefficient of friction and Aspect Ratio (AR) (quotient between structure depth and the spatial period) [114], [115] and spatial period on stainless steel [116], increasing of the SWCA in coronary stents [117], wetting properties in 100Cr6 (martensitic bearing steel) for controlling the lubrication phenomena [118], enhancement of optical absorption on stainless steel [119], tuning the wetting response on titanium [120], increasing the electrode life-time during welding of aluminium alloys [121], cell proliferation and viability on titanium implants [122], decoration based on structural diffraction colours on stainless steel [123] and nickel foils [124], as well as in the field of nanomaterials for the fabrication of variable-sized platinum nanoparticles [125], ZnO nanowires on GaN [126] for sensor arrays and the fabrication of gold nanowhisker supperlatice [127]. In addition, DLIP technology has already been used to treat large areas in 2D and 3D parts with periodic micro and nanostructures [92].

Explicitly on metallic surfaces the minimal achievable spatial period that can be transferred to a certain surface is controlled by the thermal properties of the material as well as laser wavelength and the laser pulse duration correlated with the exposure duration. For example, if nanosecond pulses are used to treat metals, the structuring mechanisms are based on thermal processes and it implicates physical mechanisms as the Marangoni effect [128] and the recoil pressure [129]. Furthermore, it was pointed out [130] that the minimal spatial period that can be fabricated with high homogeneity is about twice the thermal diffusion length. In particular, if the used spatial period of the interference pattern is in the same order as the thermal diffusion length (for example ~ Λ= 530 nm for stainless steel -1.4016-irradiated with 10 ns laser pulses), a low thermal contrast is observed (temperature difference between maxima and minima positions over the spatial period) which inhibits the local treatment of the material at the maxima positions and thus the material is molten over the whole irradiated area [131]. Additionally, for short spatial periods about < 2 - 3 μm, the structure heights are generally limited to a few hundred nanometres when using ns laser pulses [132]. Thus, based on Eq. 6 (introduced in Chapter 2), for a certain material the thermal diffusion length can be only shortened by reducing the pulse duration. Therefore, if picosecond pulses are used (i.e 10 ps), the material can be precisely heated at the interference maxima positions which reduces the amount of produced melt and allows fabricating patterns even in the sub-micrometre range [131] .

In addition to line-like patterns, a two-beam configuration can be also used to produce more complex pattern geometries. For example, if the target material is irradiated more than once and the substrates are rotated a certain angle (e.g. 90 °) between the irradiation steps, pillar-like patterns can be produced. However, due to the relative strong melting taking place when using nanosecond laser pulses on metals, the first structure is commonly erased by the second one [132].

3.3.3 Laser-Induce Periodic Surface Structures

Laser-Induce Periodic Surface Structures (LIPSS) consist of regular wavy surface structures, with amplitudes and periodicity in the sub-micrometre range. The first time they were reported was in 1965 on semiconductors [133]. Subsequently, they have been produced on metals [134], dielectrics [135] and polymers [136]. In general, if the spatial periodicity of the LIPSS is close to the laser wavelength and their orientation orthogonal to the polarization of the laser beam, the LIPSS are classified as Low Spatial Frequency LIPSS (LSFLs). Furthermore, ripples considerable smaller than the laser wavelength, are referred as High Spatial Frequency LIPSS (HSFLs). The orientation of the HSFLs can be either parallel or orthogonal to the laser beam polarization. However, HSFLs have been only produced using ultrashort laser sources. Experimentally, the HFSLs grow on metals irradiated at low fluence levels compare to LSFLs [137].

Additionally, if a large number of pulses is applied structures larger than the laser wavelength can be generated, they are called grooves [138]. Different models have been proposed in order to predict the formation of LIPSS, nevertheless, a complete understanding of the mechanisms involved is still missing. A common approach used to explain this phenomena lies in the interference effects of the incident laser radiation with surface electromagnetic waves, which produced surface plasmon-polariton waves on metals and a transient excitation of free electrons due to multiphoton or tunneling ionization for the case of semiconductors [139]. Furthermore, the LSFLs and HSFLs can be classified in the frequency domain depending on their signal associated with their feature size and orientation [140]. The interesting remark is the fact that LIPSS can significantly impact the wetting, friction and optical properties on metallic surfaces [141]–[143].

LIPSS formation has shown dependency on various micromachining parameters including: the laser beam polarization, angle of incidence, wavelength, scanning velocity, fluence and number of pulses [144]. Furthermore, interesting topographies can be fabricated, for instance hierarchical triangle structures via double-pulse irradiation consisting in interpulse delays of femtoseconds laser pulses [145] or multi-directional biomimetic structures by controlling the electric field symmetry of cylindrical vector laser beams [146].

3.3.4 Challenges for laser surface texturing methods

One of the main factors of the surface texturing processes is the cost effectiveness. From this perspective the combination of nanosecond laser sources and DLW technique offers an economic route to fabricate microstructures on metal surfaces. However, it is important to mention that the thermal effects are predominant and decisive on the final topography on metals when nanosecond laser pulses are used. In this case, the final surfaces are commonly correlated with one-scale microstructures. Furthermore, as aforementioned the feature size is limited to around 10 μm due to the

wavelength-specific diffraction limit. Some of these limitations can be overcome using ultra short laser sources, fabricating LIPSS or even using advanced laser techniques as DLIP. However, ultra-short laser sources are more expensive than laser sources emitting nanosecond pulses.

For manufacturing sectors the main success depends on the product quality in a predefined cost. In this context, the analysis of surface homogeneity for the structured surface materials must be considered. In general, microstructures fabricated by laser-based methods on metallic surfaces are produced with laser systems having a Gaussian beam shape (TEM00 beam profile). This beam profile distribution is usually connected with inhomogeneous microstructures. One possible solution is the use of top-hat profiles, which could enhance the homogeneity on the laser treated surface [147]. Furthermore, for periodic surface textures a characterisation method and surface parameters which defines a grade of homogeneity are still missing. These parameters would be helpful for a feedback in manufacturing laser texturing processes, which in conjunction with in-line monitoring systems would allow a successful evaluation of the fabricated surface texture and a the same time provide a quick feedback to the operator.

Laser-based texturing methods offer the possibility of use different laser system in more than one-step processes in order to fabricate topographies with various length scales and achieve hierarchical micro- nanostructures. However, the main objective is to make the fabrication process of periodic hierarchical micro structures as less complicated as possible. The accomplishment of this aim by one laser source could reduce the production time.

In the area of surface functionalization, wetting and drag control are surface properties that can be controlled by tuning surface topographies. Explicitly, anti-finger print, anti-fouling or anti-icing applications depict high potential based on the superhydrophobic effect. Therefore, broad the understanding of wettability in association with micro- and nanostructures would allow researches control the surface functions and scaling up them on technological materials. In this context, the fabrication of repetitive microstructures with separation distances smaller than 20 μm is of high interest in a wide range of applications since they provide generally a better performance on different surface functions [63]. For example, cell orientation, proliferation and differentiation can be stimulated on biomaterials, especially with feature sizes in the micro- and nanometre scale [148], [149]. In the field of wetting, larger SWCAs can be achieved using structures smaller than 10 μm, outcome attributed to the fraction of the solid contact area [19]. Furthermore, other researchers suggest that the performance of structured surfaces with periodic features below ~ 20 μm in conjunction with large ARs can potentially prevent ice accumulation [150] which represents a high value particularly for the aerospace industry. Low wettability surfaces promise a passive anti-ice or icephobic effect, nevertheless, water repellence is not enough to avoid the ice-accretion on aircrafts, since anti-icing surfaces require the ability of suppress ice nucleation in order to impede frost formation and reduce ice adhesion forces [151]. Moreover, the strictest challenge is the durability of a specific function on the

material surface. It involves the resistance to specific environments by means of surface robustness, in terms of erosion resistance and surface chemical control.

In the field of throughput, the laser surface texturing methods need shorter processing times in order to be competitive in industrial processes. Typical methods of machining with ultrashort pulses are carried out by raster scanning or machining of sequentially overlapping linear trenches, it represents a route to increase the structure depth and thereby the AR can be controlled by decreasing the pulse-to-pulse distance (d). In general, bringing several number of laser pulses on a certain area impacts the time processing. For example, on stainless steel by using fast galvanometer scanner systems in combination with femtosecond laser sources at 3.2 MHz and separation pulse distances of about 5 μm, rates of 250 cm^2/min have been achieved in order to fabricate diffraction patterns [152]. On the other hand, for the fabrication of spikes or microgrooves, which requires lower separation pulse distances with the combination of two-dimensional galvanometric mirrors, rates of 0.018 cm^2/min at 1 kHz have been reached [153]. Regarding the polygon scanning systems, experimental studies in the field of surface blackening shows throughputs of 0.033 cm^2/min using femtosecond laser sources with a repetition rate (f) of 2 MHz [154]. Note that the maximum available scan fields for polygon scanner systems range from 17 cm to 30 cm [155], [156], which in some cases could limit the large irradiation areas.

In Fig. 5 is represented the achievable micro- and nanostructure resolution (structure size) for different technologies as a function of the fabrication speed [123]. As one-step process, DLIP is pointed out with its actual fabrication speed and its objective in order to be industrially competitive.
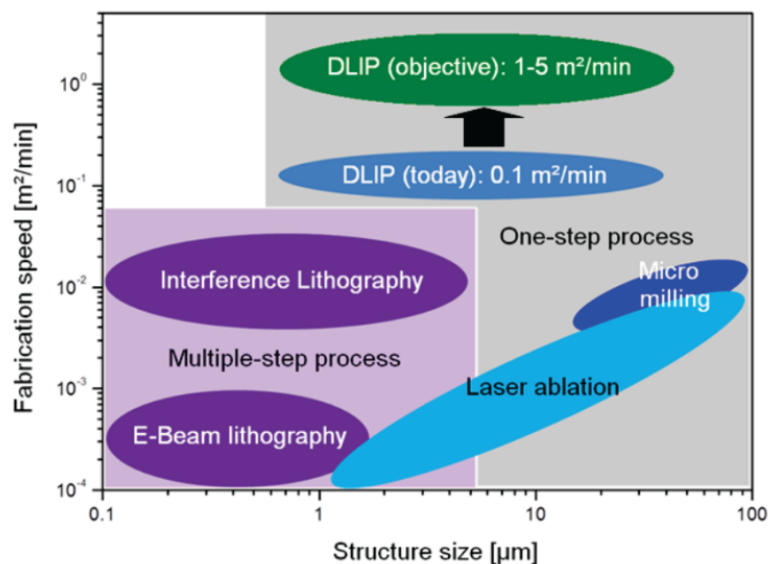

Fig.5. Fabrication speed as a function of structure sizes for different surface texturing methods [123].

Finally, for the DLIP process, the parameters which connect a desired topography surface with a certain surface property as a function of the feature size, AR and consequently with the throughput of the process are still under research.

The next frontiers are in two directions: 1) extending the structure sizes beyond the micrometre scale in accordance with the increasing in fabrication speed, which should offer the achievement of competitive industrial throughputs. As well as 2) research on durable multifunctional micro- nanostructures connected with a minor number of fabrication steps. It will offer more alternatives to be scale-up, which represent an interesting and potentially area of innovation. Therefore, a compromise is necessary between costs, surface homogeneity, fabrication speed, resolution of structure size and durability.

3.4   Surface properties affected by laser micro/nano texturing on metals

The fabrication of periodic and well-defined microstructures on metal surfaces has attracted attention due to the possibility of controlling surface properties for example, self-cleaning and friction reduction. This section gives brief descriptions of the phenomena linked to these surface properties and their limitations.

3.4.1   Impact of laser surface textures and chemistry on wettability

The capacity to repel water is associated to superhydrophobic surfaces. Conventionally on metals it can be achieved mainly by three methods: modifying the surface by low surface free energy materials [157]–[159], creating a rough structure on a hydrophobic surface (SWCA > 90 °) [160] and by a combination or both [161]. From the perspective of surface chemistry is important to consider that metals tend to be hydrophilic due to the formation of surface hydroxyls which are polar and interact with the molecules of water with polar forces. Surface hydroxylation and oxidation as well as their hydrophobicity are time-dependent [162]. Thus, a key point to reduce the wettability, or increase the SWCA is to reduce the polar content on the surface. For example, it has been proved that the hydroxyls on the oxide aluminium surface lead the reduction of wettability by reducing the polar component of surface free energy [163]. Furthermore, it is well known that the contact angle of a surface is not only dependent on the surface morphology and chemistry but also on the liquid. Due to the smaller surface tension for less polar liquids compared with water, the contact angles of water droplets can be much higher than droplets of less polar liquids (such as octane and methanol) on the same surface [164].

To ensure repellence of low surface tension liquids (e.g. organic liquids), the surface energy of the solid surface should be about few mJ/m^2 [165]. This requirement highlights the difficulty of fabricating super-oleophobic surfaces and limits the choice of coating materials. The lowest surface energy groups are ordered as $– CH_2 > –CH_3 > –CF_2 > –CF_2H > –CF_3$. The fluoromethyl ($–CF_3$) has the lowest value of surface energy (8 mJ/m^2) [166]. Thus, fluorinated components are one of the most commonly used materials for lowering the surface energy owing to their high content of $–CF_3$ and –

CF_2 groups [167]. These groups exhibit strong carbon-fluorine bonds; therefore, they are poorly susceptible to intermolecular forces (Van der Waals forces).

The modification of the surface chemical composition on metals by lowering the surface energy allows the preparation of anti-wetting and super-repellent surfaces by different deposition methods (e.g. dip-coating, CVD, electrochemical deposition). It has to be mentioned that most of these methods modify the surface topography in addition to the chemical modification. In an isolated approach, superhydrophobic surfaces were experimentally fabricated on aluminium alloy foils by a method which combines mechanical roughening and a post chemical etching with a solution of $Cu(NO_3)_2$. It must be pointed out that using the two methods separately cannot produce superhydrophobic surfaces. That means that the mechanical roughening, which produce large sized pits and reticular microstructures, and the chemical etching process promote together higher SWCAs [168].

Considerable efforts have been carried out in order to understand how microstructures impact the wettability [160], [169], [170]. Different physical simulations show that the wetting state of a droplet is in function of the feature size and the distance between microstructures (e.g. micro-pillars), where the addition of nanostructures on the microstructures affects significantly the WCA (Water Contact Angle), in certain cases inducing a transition from Wenzel to a Cassie state [171], [172].

In the field of laser surface texturing, if a metal surface is irradiated and topographically modified, a wettability transition as a function of the time from the hydrophilic to the hydrophobic state has been reported by different authors [173], [174]. For, instance, on aluminium samples (99.9 % purity), the transition is associated with the adsorbed organic compounds coming from the ambient air [175]. Frequently, these surface chemistry changes allow that after a determined period of time the surfaces achieve a superhydrophobic state. Additionally, on aluminium surfaces treated by laser, the atomic ratio C/Al and the relative amount of C-C (H) serve as an indicator of the surface polarity. Higher C/Al and C-C(H) (at %) values indicate a more nonpolar content on the surface which tends to be hydrophobic [176].

On other metals as stainless steel 316L, a large term evaluation of the SWCA allowed evidencing stable and unstable hydrophobicity states depending on the fluence applied by nanosecond laser pulses, which can be conclusive in order to reach a superhydrophobic state after a period of time [177]. Hence, also on stainless steel the structures cannot solely be responsible for the observed high contact angles. Different studies attribute this wettability change to the CO_2 decomposition reaction which takes place over time, it promotes that nonpolar carbon accumulates on the rough surface which potentially increases the SWCA [178]. This scenario evidence the importance of surface chemistry on the wettability phenomena on laser irradiated metal surfaces.

In the last ten years several surface geometries have been fabricated using pulsed laser sources, the main goal is to describe the correlation between the topography and WCA´s. In a brief

summary, Fig. 6 shows the SWCA as a function of the resolution geometry size fabricated by pulsed lasers on different metallic surfaces. The geometries include: micro cells [103], [179]–[181], micro holes [182], [183], micro grooves [184], [185], LIPSS [143], pillars- [186] and line-like patterns [187], [188].
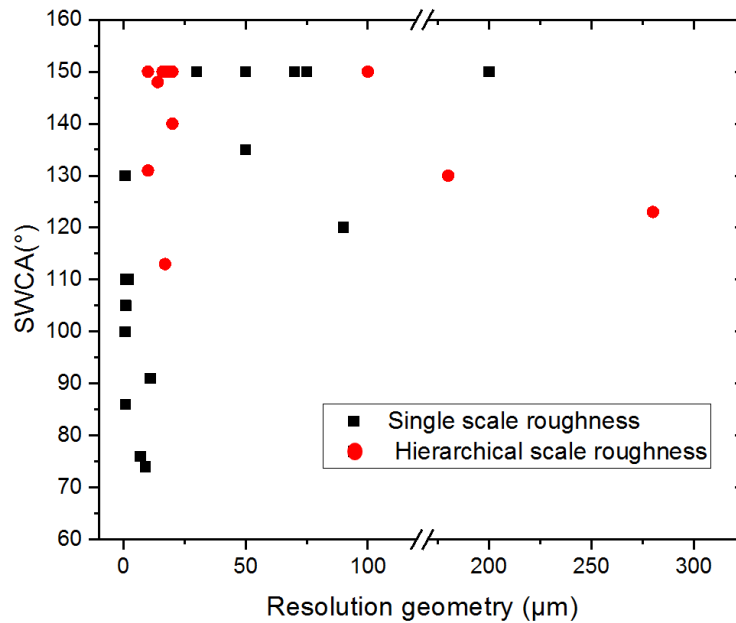

Fig. 6. SWCA achieved by microstructures fabricated by pulsed laser systems as a function of the resolution geometry achieved.

Regardless a determined geometry it is observable that topographies which promote a hydrophobic state are located in the range of 10 µm to 200 µm. In Fig. 6 the red points belong to publications which reported hierarchical microstructures, they usually consist of nano features which cover a main microstructure [180], [184], [189], [190], while the black points correspond to single scale microstructures [103], [187], [188], [191], [192]. Moreover, the microstructures associated to the points in Fig. 6. were fabricated using nanosecond [103], [182], [186], [188], picosecond [176], [190] and femtosecond laser sources [143], [180], [181], [184], [185], [189], their wettability trends depict that the SWCA results do not depend intrinsically on the laser source, but also in the resulted geometry. It is observable that single and hierarchical microstructures achieved the highest SWCA when they oscillated from 5 µm up to 70 µm in resolution geometry. On the other hand, single-scale structures smaller than 2 µm does not have a higher performance on the enhancement of hydrophobicity, as well as the hierarchical microstructures larger than 150 µm [186]. Besides, the superhydrophobic state was also achieved after a certain period of time on brass [187] and titanium [191]. Finally, for the included superhydrophobic surfaces in Fig. 6, the reported CAH measurements have not a clear trend, since values lower than 10° were reported on the single and hierarchical structures.

3.4.2   Control of the friction coefficient

On steel alloys, micro- and nanostructures fabricated by laser show an important impact in the control of friction. Usually, friction increase can be promoted by producing micro-dimples in the range of 50 µm to 140 µm [193] with AR larger than 0.21. On the other side, the reduction of friction reveal better performances if micro-structures in the range of 10 µm to 200 µm are used with AR ranged from 0.1 to 0.15. These outcomes were measured under hydrodynamic lubrication regimes [194]. It means that the microtextures on the surfaces have functions as micro-hydrodynamic bearings, micro reservoirs for lubricant retention or micro-traps for wear particles of sliding systems; they are applicable, for instance, in seals, pistons rings and thrust bearings.

For the assessment of topographies, different researches recorded Stribeck curves for unstructured and microstructures samples in order to investigate the influence of the micro features on different lubrication regions, such as boundary, mixed and hydrodynamic lubrication region [195]. Results show that circular dimples produced via laser surface texturing can be connected with an optimal dimple depth, which causes a dramatic decrease of the Coefficient of Friction (CoF) compared to the untreated material [196]. However, at high sliding speeds (< 0.2 m/s), the differences in friction during the tribological tests become insignificant, because the lubricant fluid film thickness increases. This implies that when the surface contact enters to the full fluid film lubrication regime, the surface texture is expected to play a minimal role in friction behaviour. In this case also a higher dimple density can resulted in high CoF [197].

3.4.3   Impact on fatigue performance

Experiments on Ti6Al4V evidenced that the fatigue crack initiates in the laser modified region, rather than at the edge of the rectangular specimens in the untreated condition. The investigated surfaces consist on LIPSS fabricated by femtosecond laser pulses [198]. It is argue that the fatigue resistance is diminished when notches are promoted by the laser treatment. Furthermore, crystallographic microstructure changes in the surface can also impact the fatigue properties; this was evidenced when continuous wave laser sources are used. The difference is highlighted by the laser affected region, it is about 9 nm in depth by using femtosecond laser pulses, and while using continuous wave lasers it achieves more than 500 µm in depth [199]. As a remarkable point, laser cut-edges have a significant influence on the mechanical properties. In this context, an important factor for producing a high quality laser cut-edge surface is the generation of striations. At high number of cycles the formed striations formed during the laser cutting process act as stress raisers which are the source of localised plasticity and consequently crack initiation [200]. It can be concluded that smooth surfaces are less prone to crack initiation, since the striations or laser surface modifications regions significantly influence the fatigue performance.

4   Materials and methods

4.1   Materials

The bulk metallic samples used in this work include: Ti6Al4V, stainless steel types 1.4016, 1.4301, 1.4112 and Al2024 clad with pure aluminium surface. Their material characteristics are described in this section. They were selected due to their high range of applications in technological areas such as aeronautics, bio-applications and home appliances, which are constantly in innovate processes to overcome technical issues i.e. ice accretion, biocompatibility and self-cleaning.

Flat samples of Ti6Al4V (VSMPO, Russia) were used in the experiments associated with nanosecond DLIP (ns-DLIP) in the investigations of surface homogeneity. The samples have a thickness of 2 mm and an average surface roughness (Ra) of 0.27 µm. The material's optical reflectivity at the wavelength of 1064 nm is 57 % for a normal angle incidence [201]. This alloy is used for instance in the aerospace industry as well as in bio-applications due to its lightness, non-magnetic and biocompatibility properties [202], [203]. In this context, a surface area of 380 cm^2 for the flight test was patterned with pillar-like microstructures fabricated by picosecond DLIP (ps-DLIP). The sample of 0.30 mm thick, has a surface of 40 x 12 cm in a curved form; nevertheless it was fixed and flattened during the ps-DLIP process.

Sheets of corrosion resisting ferritic steel type 1.4016 (also called X6Cr17), 0.98 mm in thickness were used during the ps-DLIP experiments and the wettability assessment. As-received, the samples were electro-polished obtaining a Ra = 60 nm. Prior to the laser process, the substrates were cleaned of contamination using isopropanol.

Sheets of corrosion resisting austenitic steel type 1.4301(also called grade 304), 0.7 mm in thickness were used during the ps-DLIP experiments related with throughput and analytical model. As-received the samples were electro-polished obtaining a Ra = 60 nm. The substrates were cleaned using ethanol before the laser experiments.

Martensitic stainless steel 1.4112 (also called X90CrMoV18) cut in a rectangular shaped parts of 16 x 6 x 2 mm were structured by ps-DLIP and assessed in tribological tests. As-received the samples were electro-polished obtaining Ra = 200 nm. The substrates were cleaned using ethanol before the laser experiments.

A standard aerospace aluminium alloy, Al2024 clad with pure aluminium surface, 2 mm in thickness was used in the DLW and ps-DLIP experiments. The samples have an initial Ra = 603 nm. The substrates were cleaned using ethanol before the DLW and ps-DLIP processes. The Al2024 alloy is extensively used for fabricating aircraft parts due to its light weight and resistance to corrosion.

4.2 Direct Laser Writing

The setup used to fabricate topographies by DLW is located in the UPM in Madrid, Spain. The experiments were carried out using a Q-switched pulsed Spectra-Physics nanosecond solid-state laser source that generates pulses with duration of 15 ns. The laser allows using repetition rates in the range of 20 kHz up to 100 kHz, emitting the fundamental wavelength of 1064 nm which is frequency-tripled by a nonlinear optical conversion to deliver pulses at the wavelength of 355 nm. The laser beam was focused on the sample at normal incidence angle with a 250 mm focal lens to generate a spot size diameter of 15 μm. The beam size was retrieved using the Beer-Lambert law and plotting the dimension of the ablated area as a function of the laser pulse energy [204]. The position and relative motion of the sample was controlled using a translational x and y stage with a resolution of 0.1 μm, using speeds ranging from 10 mm/s to 80 mm/s.

The strategy to fabricate squared shaped micro-cells consists in a succession of lines intersecting themselves at 90°. The distance between each micro-cell was varied in the range of 30 μm up to 50 μm, with a laser power ranging from 100 mW up to 490 mW.

4.3 Direct Laser Interference Patterning

The setups used to fabricate the different investigated DLIP topographies were developed at Fraunhofer IWS and the TU Dresden. The nanosecond DLIP experiments were conducted using a compact DLIP system (DLIP-μFAB, Fraunhofer IWS), it is shown in Fig. 7 (a). The system is equipped with a Q-switched Nd:YLF laser (Laser-export Tech-1053 Basic) operating at 1053 nm that provides 12 ns pulses at 1 kHz with pulse energies up to 290 μJ, emitting the fundamental transverse mode (TEM00) with a laser beam quality factor of $M^2 < 1.2$, a three-axis positioning stage system with an accuracy of ± 2.5 μm and a DLIP optical head. A schematic representation of the main components in the DLIP-setup is presented in Fig. 7 (b). Inside the DLIP optical head, the main beam is split in two sub-beams by means of a Diffractive Optical Element (DOE), they are later parallelized by a prism and finally overlapped using a plano-convex spherical lens with a focal distance of 40 mm. Fig 7 (c) shows a schematic representation of the components in the experimental DLIP optical head [131]. By controlling the position of the prism, it is possible to automatically change the spatial period associated with a characteristic angle Θ. Thus, by varying the angle of incidence of the beams on the sample surface a determined spatial period ranging from 1.29 μm up to 7.20 μm can be produced. For instance, by setting the interference angles Θ to 4.23 °, 5.24 ° and 7.09 °, spatial periods of 7.20 μm, 5.82 μm and 4.31 μm can be calculated using Eq. 15.
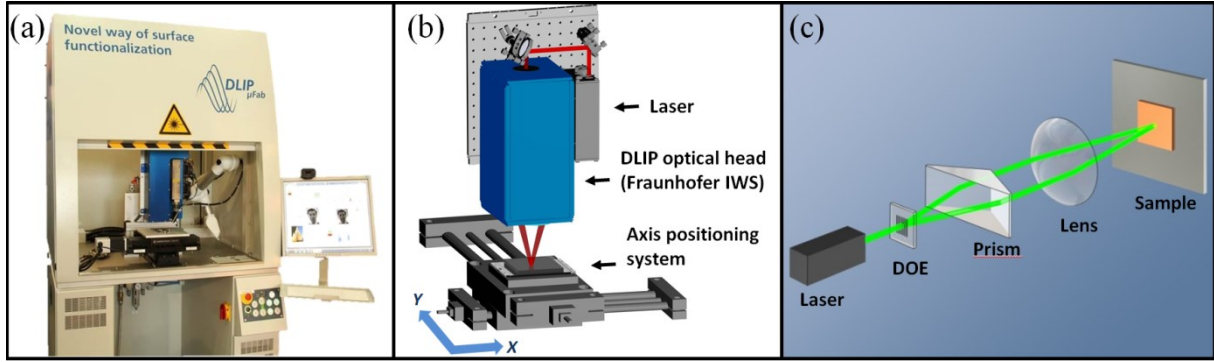
Fig. 7. (a) DLIP-µFab system, (b) schematic representation of the main components in the DLIP-setup and (c) optical elements used for a two-beam interference setup.

The setup produces a DLIP-pixel (irradiated area per pulse which contains the interference pattern) with a diameter of the laser interference area (Ø) of 160 µm. To extend the treated area, the sample was moved in the *x* and *y* directions, using the strategy depicted in Fig. 8.
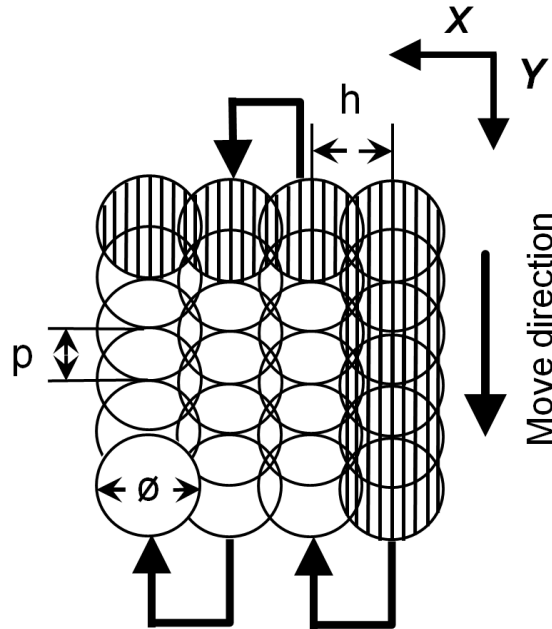

Fig. 8. Schematic representation of the pulse distribution used during the two-beam DLIP set up, *h*, *p* and Ø denote the hatch distance, pulse-to-pulse distance and diameter of the laser interference area, respectively.

In this way, the pulse-to-pulse overlap (OV) can be varied from 0 % up to 99 %. The overlapping of the pulses was performed in the *y*-direction in which the line-like patterns are oriented. In the *x*-direction, the pulses were separated by a fixed distance hatch distance (*h*). The pulse-to-pulse distance (*p*) is then defined by the repetition rate of the laser and the linear speed in the *y*-direction. Note that the DLIP pattern is oriented parallel to the move direction. The OV can be calculated as a function of *p* and Ø using the Eq. 18:

$$OV = \left(1 - \frac{p}{\emptyset}\right) \cdot 100 \qquad (18)$$

For the ps-DLIP experiments the large area DLIP system to process 2D and 3D parts shown in Fig. 9, was employed. The structuring of metallic substrates was performed using the two-beam DLIP configuration. The set up contains a solid-state Q-switched Innoslab Nd:YVO$_4$ (Edgewave PX200-3-GH), it can operate at one of the following wavelengths: 1064 nm, 532 nm and 355 nm, emitting pulses with a pulse duration of 10 ps. The laser allows using repetition rates in the range of 1 kHz to 30 kHz with pulse energies up to 1000 µJ at 10 kHz at the wavelength of 1064 nm, emitting the fundamental transverse mode (TEM00) with a laser beam quality factor of $M^2 < 1.5$. The used wavelength was 1064 nm with a horizontally polarized laser beam. The set up also contains a DLIP optical head (Fraunhofer IWS) and a three-axis positioning stage system with an accuracy of ± 2.5 µm. In the DLIP optical head, the primary beam is split in two sub-beams by means of a DOE with a diffraction angle for the first order of 9.21 °. Afterwards, the beams are parallelized using a prism with an angle of 19.93 ° and are finally overlapped using plano-convex spherical lenses, either with a focal distance of 40 mm or 100 mm. The optical configuration allows the fully automatic control of the spatial period in the range from 1.2 µm up to 6.0 µm and 4.0 µm up to 17.0 µm, respectively. By using different lenses (Galilean telescope), Ø can be adjusted in the range values between 160 µm up to 340 µm (40 mm focal lens) and from 480 µm up to 750 µm (100 mm focal lens). The Ø values were calculated by means of the laser beam radius (1/e^2), using the D-squared method [204].

To produce the pillar-like (or cross-like) patterns, the samples were first processed to fabricate the line-like pattern and after that they were rotated 90 ° in the *x-y* plane and re-irradiated. The laser experiments were carried out at normal ambient-pressure conditions without subsequent treatment.

Fig. 9. Large area DLIP system for processing 2D and 3D parts.

For the set of experiments regarding the melting of LIPSS features (which are fabricated during the ps-DLIP process) the samples were processed using a 12 ns pulsed Q-switched Nd:YLF laser (Laser-Export TECH-1053 Basic). The laser wavelength was 1053 nm and $f = 1$ kHz was used. The laser provided a TEM00 beam intensity distribution with a M² < 1.2 and the spot size at the focal position has a diameter of 145 μm. To cover larger areas, the substrates were translated in x and y directions following the same strategy depicted in Fig. 8 with a OV = 90 % and a $h = 75$ μm. The laser fluence F was varied between 0.19 J/cm^2 and 0.55 J/cm^2.

4.4   Surface chemical treatment

Samples were chemically treated by dipping them in a hydrophobizing agent (Mecasurf®, Surfactis) after the laser processes. This agent (ethoxydifluoromethyl, $C_{13}H_3F_{27}O_2$) used covalently bonded fluoride groups to cover the surface, saturating the material with non-polar compounds (reducing the surface energy) with an ultrathin layer (< 5 nm). It is important to mention, that the chemical reaction can take place only if the surface is not passivated with organic compounds. Therefore, the samples must be chemically treated directly after the laser process. The dipping process consists of immersing the samples for five minutes in the hydrophobizing agent. Afterwards, the sample was removed left for about two minutes until the solvent was completely evaporated.

4.5   Characterisation methods

There are different techniques used to retrieve information about a surface topography as well as roughness measurements. The measurement techniques can be divided into two categories: (a) contact type and (b) noncontact type. The here employed techniques for assessment surface topography belong to the noncontact type. For the wettability, coefficient of friction and fatigue tests, mechanical contact systems were employed.

4.5.1   Water Contact Angle

SWCA and CAH were conducted in a contact angle measurement system (OCA 20, Dataphysics Instruments GmbH), using the tangent searching fitting mode. The WCA measurements were carried out using 4 μl deionized water. Advancing contact angles were measured by gradually increasing the volume of the water droplet from 4 μl up to 12 μl at a rate of 0.9 μl/s. For the receding mode, 8 μl were retired. These parameters were kept constants during the experiments in order to be comparable.

4.5.2 White Light Interferometry and Confocal Microscopy

The treated surfaces were characterised using confocal microscopy (LeicaSCAN DCM3D) with a 150X magnification objective, allowing lateral and vertical resolutions of 140 nm and 2 nm, respectively.

White Light Interferometry (WLI) (LeicaSCAN DCM3D) was used during the homogeneity quantification of the line-like structures fabricated using nanosecond DLIP on titanium. WLI measurements were carried out with a 50X magnification, with a resolution of 340 nm and 4 nm in the x and y direction, respectively. A single measurement can record an area of 351 µm x 264 µm, therefore, the assessment of an extended area is approached in four adjacent single areas resulting in a total area of 702 µm x 528 µm, which is significantly larger than the DLIP pixel diameter (160 µm) produced in the interference area. Along the measured total area, five individual roughness profiles were extracted (perpendicular to the line-like patterns). The heights of the profile elements were extracted using the software MountainsMap® 7.4 by the step height measurements function.

4.5.3 Scanning Electron Microscopy and Energy Dispersive X-ray Spectroscopy

Scanning Electron Microscopy (SEM) images and Energy Dispersive X-ray spectroscopy (EDX) analyses were carried out using a Zeiss Supra 40VP at the operating voltage of 5 kV.

4.5.4 Raman Spectroscopy

The Raman spectra were measured using the Renishaw inVia™ Qontor® Raman microscope. It uses an Ar+- laser for the excitation at 514 nm. The laser power was set to 0.4 mW and focused with a 50X objective on the sample surface. The spectrum is dispersed in the horizontal direction which covers the range of Raman frequencies from 100 cm^{-1} to 3500 cm^{-1}, the measuring time was set to 1 min.

4.5.5 X-ray Photoelectron Spectroscopy

X-ray Photoelectron Spectroscopy (XPS) measurements were carried out using an Amicus spectrometer (Kratos Analytical, UK) equipped with a non-monochromatic Mg Kα X-ray source operated at 240 W and 8 kV. The kinetic energy of the photoelectrons was determined using an analyser with pass energy of 75 eV. The take-off angle between sample's surface normal and the electronoptical axis of the spectrometer was 0 °. In this case, the information depth is about 8 nm. Spectra were referenced to the C1s peak of aliphatic carbon at a binding energy of 285.0 eV. A

satellite subtraction procedure was applied. Quantitative elemental compositions were determined from peak areas using experimentally determined sensitivity factors and the spectrometer transmission function. C1s spectra were deconvoluted by means of CasaXPS (Casa Software Ltd., UK).

4.5.6 Tribological test

The determination of the CoF was carried out using an Anton Paar Tribometer (MCR301). The tribological counter body consists in a 100Cr6 ball with a diameter of 12.7 mm. Three samples were fixed on a sample holder at 45 ° in relation with the horizontal plane. Afterwards, 1 μl of polyalphaolefin with a dynamic viscosity of 32.2 mPa/s was placed on the surface using a microliter-pipette. The system temperature was set to 25 °C, and the normal force of 25 N was applied. Finally, the Stribeck curves were recorded using a logarithmic ramp up to 1.4 m/s.

4.5.7 Fatigue test

Fatigue tests were carried out on the electromagnetic resonance testing machine (Gigaforte 50, Rumul) with a 50 kN load-amplitude and a test frequency of 985 Hz. The load increase test was carried out at the stress ratio (R) of 0.1 until failure. Each load level included 10^7 load cycles and in the case that the failure did not occur, the load was increased by 10 MPa. A total of 8 mechanical polished samples from each group were tested, they included: unstructured, line-like structure and pillar-like structure. The specimen geometry used was according to DIN 50125, the length dimensions are represented in Fig. 10 (a). The center of the samples was structured by ps-DLIP covering a length of 50 mm using the same DLIP topography on one sample side, either line or pillar-like structures. Laser parameters of Λ = 5.20 μm, OV = 99 %, f = 10 kHz and F = 0.74 J/cm² were used for both topographies. In Fig. 10 (b) are showed the structured samples, upper side line-like structures and down side cross-like structures.
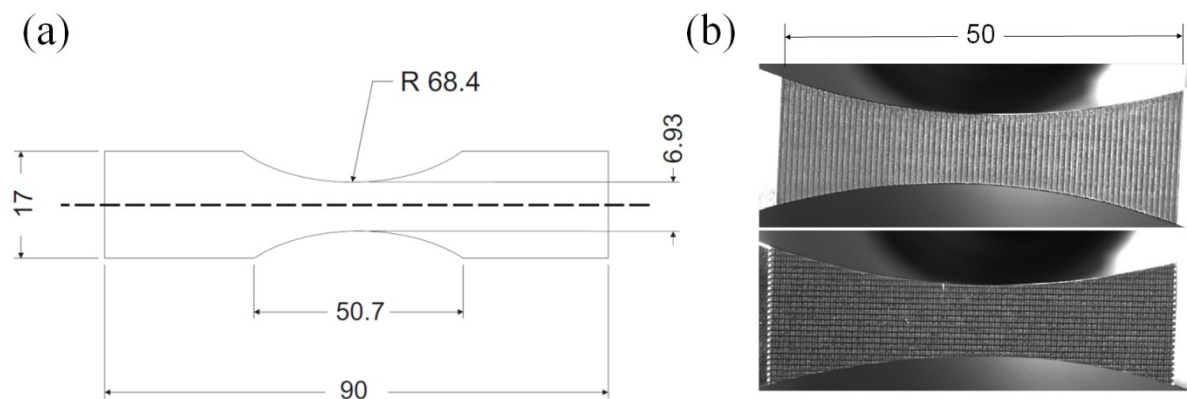

Fig.10. (a) Sample geometry employed the fatigue tests (DIN 50125), (b) ps-DLIP structured samples upper side line-like structures and down side cross-like structures. Units are given in mm.

5   Results and discussion

5.1   Interference structuring of Ti6Al4V using nanosecond laser pulses

In a first approach, line-like pattern with a spatial period of (Λ) 7.20 μm was produced on Ti6Al4V samples. In Fig. 11 are shown the micrographs of two topographies fabricated by the irradiation of a single-pulse nanosecond DLIP (ns-DLIP) with a diameter of the laser interference area ($\varnothing$) of 160 μm, where the fluence values of (a) $F = 0.84$ J/cm^2 and (b) $F = 1.05$ J/cm^2 were used. Inset pictures depict magnifications of the microstructure at the centre of the DLIP-pixel.
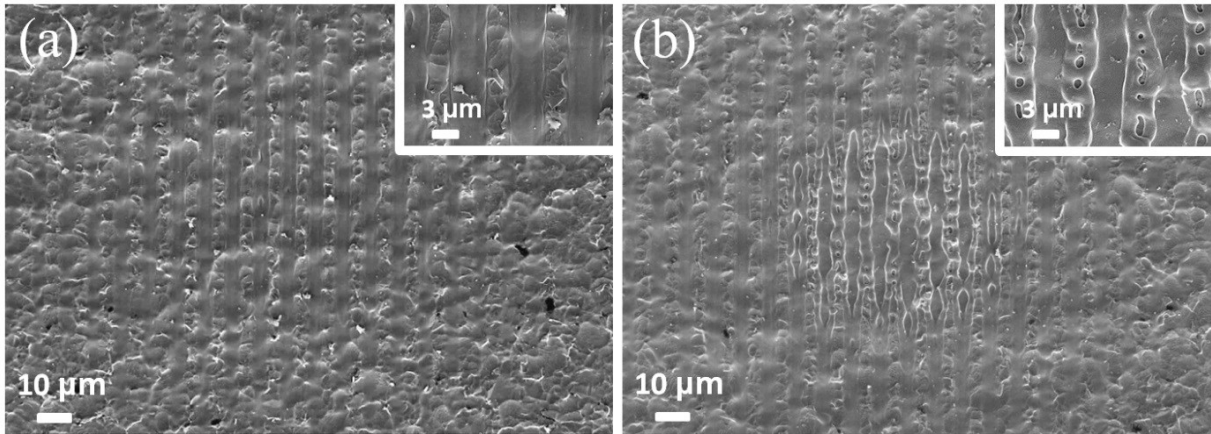
Fig. 11. Scanning electron micrographs of a single-pulse ns-DLIP on Ti6Al4V using the $\Lambda = 7.20$ μm, (a) $F = 0.84$ J/cm^2 and (b) $F = 1.05$ J/cm^2. The microstructure resulted at the centre of the DLIP-pixel was magnified in the inset pictures.

In Fig. 11 (a) is observable the line-like pattern produced by the periodic variation of the laser intensity. In the magnification showed in the inset picture in Fig. 11 (a) can be appreciated smoothed lines associated with the interference maxima positions. In detail a slightly material quantity was transferred to the colder zones (interference minima positions). The mechanism which promoted molten material at the interference maxima and then to be transferred to the interference minima positions is called Marangoni convection [128], [205]. The Marangoni convection is characterised by the flow of the molten metal from the hot (interference maxima positions) to the colder regions (interference minima positions). In Fig. 11 (b) is observed a higher amount of molten material and also a different microstructure at the centre of the DLIP-pixel. The line-like pattern is still recognizable with a non-uniform shape (see inset picture in Fig 11 (b), this result can be explained by the recoil pressure originated when the fluence value was increased and it is prominent at the centre of the DLIP-pixel due to the Gaussian-beam intensity distribution. The vaporization-induced recoil pressure increases with the surface temperature increment at the centre of the DLIP-pixel which induced the ejection of the melt from the interference maxima [16]. In the Ti6Al4V sample, after around 6 ps the energy is transferred from the electron subsystem to the lattice subsystems, so thermalization of the whole system is considered to be instantaneous [206]. Thus, when nanosecond laser pulses are used,

thermalization occurs practically during the entire pulse and thermal effects are predominant. Specifically, using a single-pulse ns-DLIP and due to the promoted recoil pressure the homogeneity of the patterns is diminished.

In a further experiment the fluence was increased to $F = 1.42$ J/cm^2. In Fig. 12 (a) is shown the resulted microstructure at the central part of the DLIP-pixel region. Even though, periodic structures with the $\Lambda = 7.20$ µm are clearly visible, the discontinuous molten material is observable. In Fig. 12 (b) the Gaussian-beam intensity distribution of two-beam DLIP configuration is graphically showed. For arbitrary values of F_{th} can be appreciated that a higher fluence is contained at the centre of the interference.
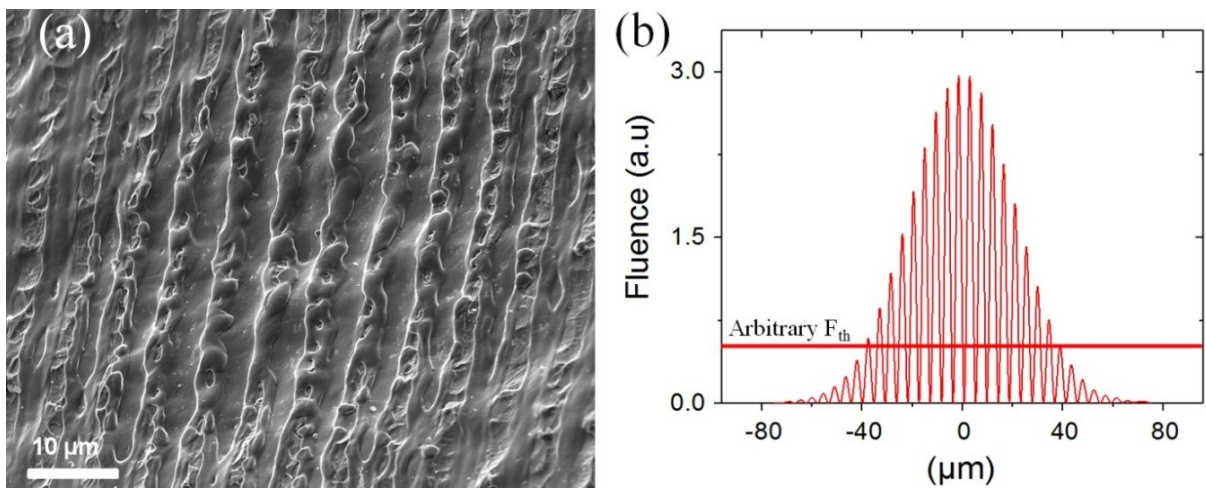
Fig. 12. (a) Scanning electron micrograph (tilted at angles of 20 ° in x and -10 ° in y) of a single-pulse ns-DLIP on Ti6Al4V using the $\Lambda = 7.20$ µm and $F = 1.42$ J/cm^2. (b) Gaussian-beam intensity distribution of two-beam DLIP configuration.

A new set of experiments was considered including the spatial periods of $\Lambda = 4.31$ µm, $\Lambda = 4.90$ µm, $\Lambda = 5.82$ µm and $\Lambda = 7.20$ µm, using fluence values ranging from $F = 0.84$ J/cm^2 to $F = 1.12$ J/cm^2. In Fig. 13 (a) are plotted the measurements of the mean height produced as a function of the fluence. By means of confocal microscopy ten height measurements were extracted from the roughness profile perpendicular to the line-like pattern at the centre of the pixel. A typical confocal image is shown in Fig. 13 (b) where the dashed line represents the position of the assessed profiles.
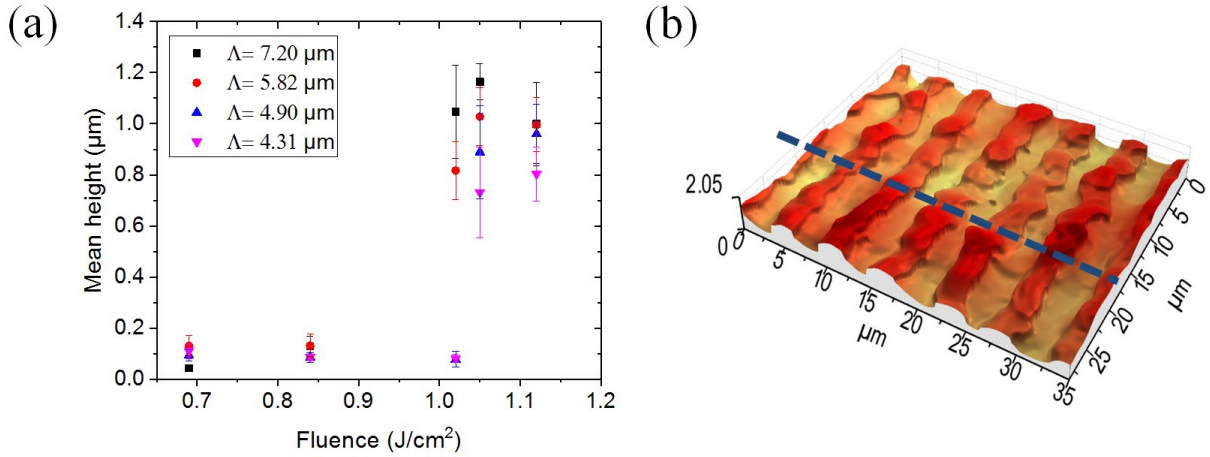
Fig. 13. (a) Mean height measurements of one-single pulse using line-like pattern fabricated by ns-DLIP on Ti6Al4V, for Λ = 4.31 µm, Λ = 4.90 µm, Λ = 5.82 µm and Λ = 7.20 µm. The fluence values were ranged from F = 0.84 J/cm^2 up to F = 1.12 J/cm^2. (b) Confocal image at the centre DLIP-pixel using the Λ = 5.82 µm and F = 1.05 J/cm^2.

For the fluence range depicted in Fig. 13 (a) a difference in structure height was measured at the centre of the DLIP line-like microstructure. It can be observed for all the spatial periods that after the fluence values of F = 1.05 J/cm^2 the mean height increase abruptly from 100 nm to about 1 µm, note that the error bars are also larger if they are compared with the error bars of the heights where the fluence values were less than F = 0.90 J/cm^2. Furthermore, at the F = 1.02 J/cm^2 the microstructures fabricated with spatial periods of 4.31 µm and 4.90 µm did not change their mean height value to a larger one, while the spatial periods of 5.82 µm and 7.20 µm the change in height occurred. This difference can be explained due to the modification of the interference angles, which increases slightly the laser interference area for the small spatial periods and then reducing the energy per area absorbed on the material. Further experiments should be carried out to verify this premise. On the other hand, by setting the spatial periods of 7.20 µm, 5.82 µm, 4.90 µm and 4.31 µm, interference angles Θ to 4.23 °, 5.24 °, 6.23 ° and 7.09 ° can be calculated using Eq. 15. Thus, for the given angles, the variation on the reflectivity is negligible, e.g. for non-polarized laser radiation [4] at the incident angle of 7.09 °, it results in a difference smaller than 0.3 %, when it is compared to the reflectivity at the normal incidence condition (0 °). The reflectivity was calculated using n (refractive index) and k (extinction coefficient) values of 3.57 and 3.50, respectively [10], [207].

5.1.1   Strategy to fabricate homogeneous DLIP line-like structures

The quality of the final surface morphology is typically dependent on the used laser beam profile which is Gaussian (TEM00 profile) in most of the commercial laser systems. The Gaussian-beam intensity distribution strongly affects the pattern homogeneity; subsequently the homogeneity in large areas can be affected during the ns-DLIP process. As a result, desirable surface properties based

on the surface topography could not be accomplished. Here is presented an approach for the improvement of surface texture homogeneity by means of the pulse distribution in ns-DLIP process using a TEM00 beam distribution. Following the pulse distribution presented in chapter 4.3, the hatch distance (h) and pulse-to-pulse overlap (OV) can be controlled in order to distribute the energy in a homogeneous form. In this perspective, the strategy consists in the reduction of the hatch distance in order to deliver homogeneously the fluence considering the Gaussian-beam distribution. In Fig. 14 is represented the cross-section of DLIP pulses with a reduced hatch distance (x direction). It could lead to fabricate homogeneous line-like microstructures, since the fluence will be consistently distributed.
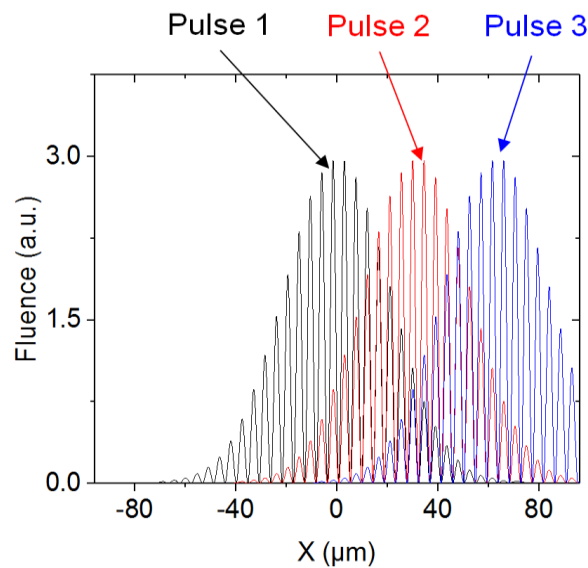
Fig. 14. Representation of homogenously distributed fluence by reducing the hatch distance of DLIP-pulses, which have a Gaussian-beam intensity distribution.

5.1.2   Development of topographical parameters for homogeneity quantification

Solid surfaces, independently of the method of formation or fabrication, contain irregularities of various orders. In technological applications, both macro- and micro/nano topographies of the surfaces are important. For better understanding on how the micro topography impacts a desired surface function on large surface areas, quantitative characterisation parameters should be developed which can assists in designing the micro-surfaces. Although important results have been obtained [208]–[212], the optimal characterisation parameters are still missing. In this context, to describe surface roughness the arithmetic mean (Ra) is an official standard in most industrialized countries. It is based on the absolute heights ($|Z|$) from the mean line of the measured roughness in a 2D profile for a determined sampling length [213]. However, this parameter does not provide any information about the slopes, shapes and sizes of asperities or about the regularity of their occurrence. Therefore it is only sensitive to average variation in the amplitude of the surface heights and does not reflect variation in local behaviour [210], [214], since equal values of Ra could mean different topographies [38], [215]. Consequently, new surface parameters are necessary for quantitatively characterise the

homogeneity of periodic patterns. The height fluctuations can be calculated by 1D extraction of the 2D profiles with the help of the software MountainsMap® 7.4. Although an analysis directly from the 3D information is possible [216], this route does not provide a height variation analysis (e.g. it is not possible to calculate standard deviations of the 2D profiles which is fundamental for the approach here used). Microstructure heights fabricated become the most relevant variable during the 2D assessment since its changes affect directly the surface texture homogeneity. Thus, the mean structure height can be calculated (Rc) by Eq. 19:

$$Rc = \frac{1}{n}\sum_{i=1}^{n} Zt_i,$$ (19)

where Zt are the heights of the i - profile elements and n is the total number of heights considered. The measurement of the data dispersion can be described by its standard deviation (Sd) using Eq. 20 [213]:

$$Sd = \sqrt{\frac{1}{n-1}\sum_{i=1}^{n}(Zt_i - \overline{Z}t)^2},$$ (20)

where $\overline{Z}t$ is the mean value of the heights of the i - profile elements. Thus, relative error ($Err\ \%$) of a periodic structure in terms of the structure amplitude can be introduced where is possible to establish a relation between the terms Sd and Rc according to Eq. 21:

$$Err\ \% = 100 \cdot \frac{Sd}{Rc}$$ (21)

As a result, the term $Err\ \%$ expresses the ratio of height variation to the measured mean height of the profile elements. Furthermore, the topography can be characterised by the kurtosis (Rku). For a discrete distribution of heights, Rku is defined using Eq. 22 which relates the mean quartic of the absolute heights ($|Z_i^4|$) and the 4th power of Rq (root mean square of the absolute heights) within the sampling length.

$$Rku = \frac{1}{Rq^4}\left[\frac{1}{n}\sum_{i=1}^{n}|Z_i^4|\right].$$ (22)

The kurtosis (Rku) characterises the spread of the height distribution and is connected to the sharpness of the roughness profile. A surface with a Gaussian height distribution has a kurtosis value of three. A spiky surface will have a high kurtosis value (> 3) and a bumpy surface a low kurtosis value (< 3) [217], [218] .

5.1.3 Impact of process parameters on surface structure homogeneity

In a first approach, the effect of the varying the OV was explored. The investigations were performed at the fixed process parameters of $F = 1.15$ J/cm^2 and $h = 43.20$ µm. Since arbitrary values could generate irregularities in the DLIP pixel distribution and lead to undefined microstructures, the hatch distance h (or pulse distribution in the x direction) was chosen as a multiple number of the

spatial period. Fig. 15 shows the SEM images of samples treated by ns-DLIP with OV values of 90.0 % (Fig. 15 (a)), 96.6 % (Fig. 15 (b)), and 98.0 % (Fig. 15 (c)), where the percentage values correspond to the number of pulses per area of 10, 30 and 50, respectively. It is observed that surfaces irradiated with a larger number of laser pulses exhibit more pronounced microstructures. For instance, the mean structure height produced by DLIP ($Rc\Lambda$, calculated using Eq. 19) fabricated with an OV = 90 %, was about $Rc\Lambda$ = 2.8 µm, while for an OV = 98 % a $Rc\Lambda$ = 6.5 µm was achieved. Consequently, AR of 0.38 and 0.90 were fabricated using values of cumulative fluence of 11.5 J/cm^2 and 57.5 J/cm^2, respectively.
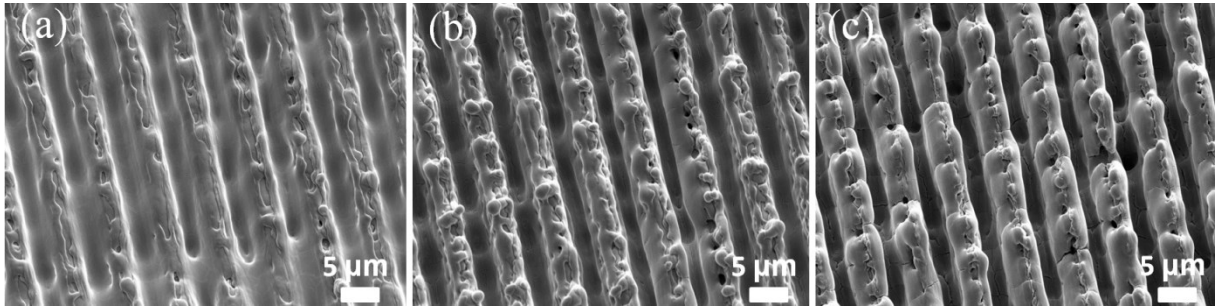
Fig. 15. Scanning electron micrographs of Ti6Al4V samples processed by DLIP producing line-like structure with Λ = 7.20 µm, F = 1.15 J/cm^2 and OV values of (a) 90.0% (b) 96.6 % and (c) 98.0%.

In a second approach, the impact of the fluence variation on the microstructure was investigated. In this set of experiments the fluence values were ranged from 1.05 J/cm^2 to 1.42 J/cm^2 by controlling the pulse energy of the laser. The parameters of Λ = 7.20 µm, OV = 90.0 % and h = 43.20 µm were kept fixed. In the SEM images depicted in Fig. 16, three different surfaces can be observed which were processed at the F = 1.06 J/cm^2 (Fig. 16 (a)), F = 1.15 J/cm^2 (Fig. 16 (b)) and F = 1.42 J/cm^2 (Fig. 16 (c)). If a low fluence value is used, the initial surface texture of the untreated substrate can still be observable after the laser structuring process (see horizontal features in Fig. 16 (a) and (b)). At higher fluence values, the initial surface roughness could be flattened and at the same time structures with higher AR were fabricated. Furthermore, the high magnification image depicted in Fig. 16 (d) clearly shows redeposition of the molten material which is produced during the laser treatment.
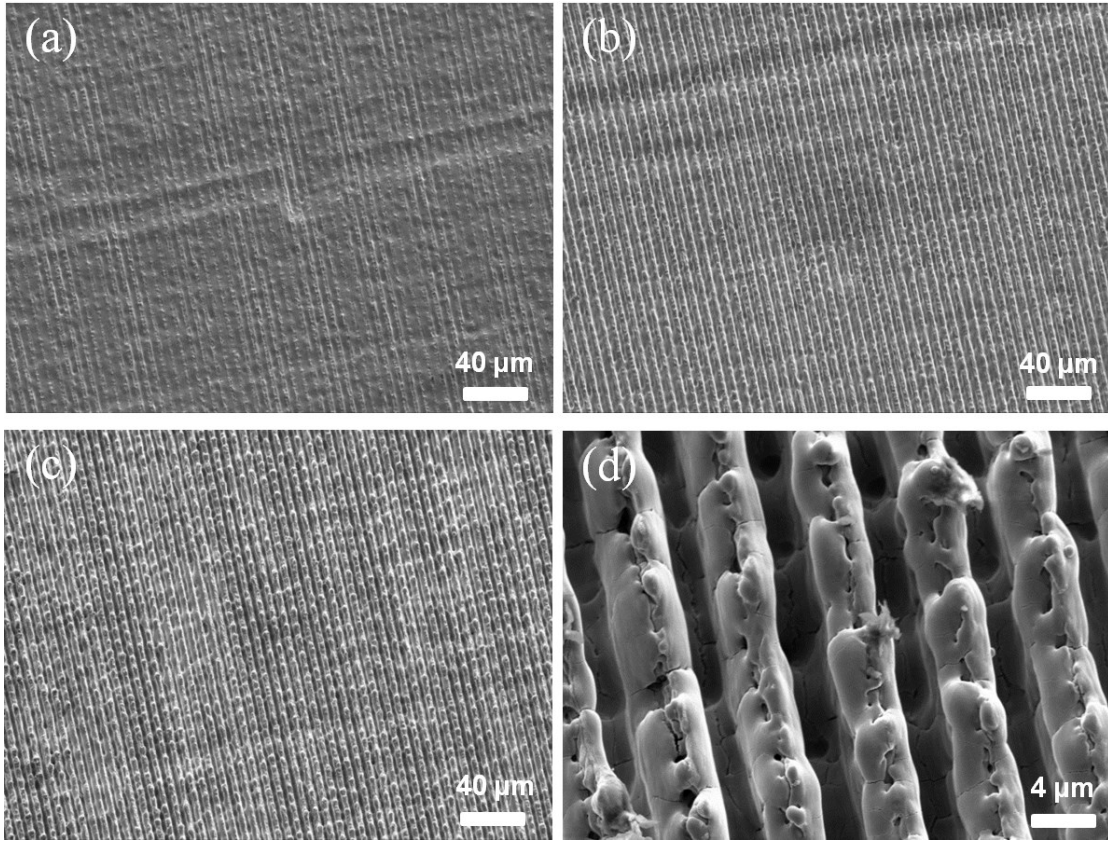
Fig. 16. Scanning electron micrographs of the nanosecond DLIP structures produced on Ti6Al4V using the $\Lambda = 7.20$ μm, the $h = 43.20$ μm, OV = 90.0 % and the fluence values of (a) $F = 1.06$ J/cm^2, (b) $F = 1.15$ J/cm^2 (c) and $F = 1.42$ J/cm^2, (d) magnification from the topography in (c).

Fig. 17 shows the WLI images of the three surfaces processed at laser fluences described in Fig. 16. Thereby, examples of roughness profiles taken in perpendicular direction to the line-like structures are depicted. The images show the evolution of the height increase as a function of the used laser fluence. For instance, Fig. 17 (a) ($F = 1.06$ J/cm^2) reveals an inhomogeneous surface pattern whereas Fig. 17 (b) ($F = 1.15$ J/cm^2) and Fig. 17 (c) ($F = 1.42$ J/cm^2) highlight line-like patterns with a more defined shape.
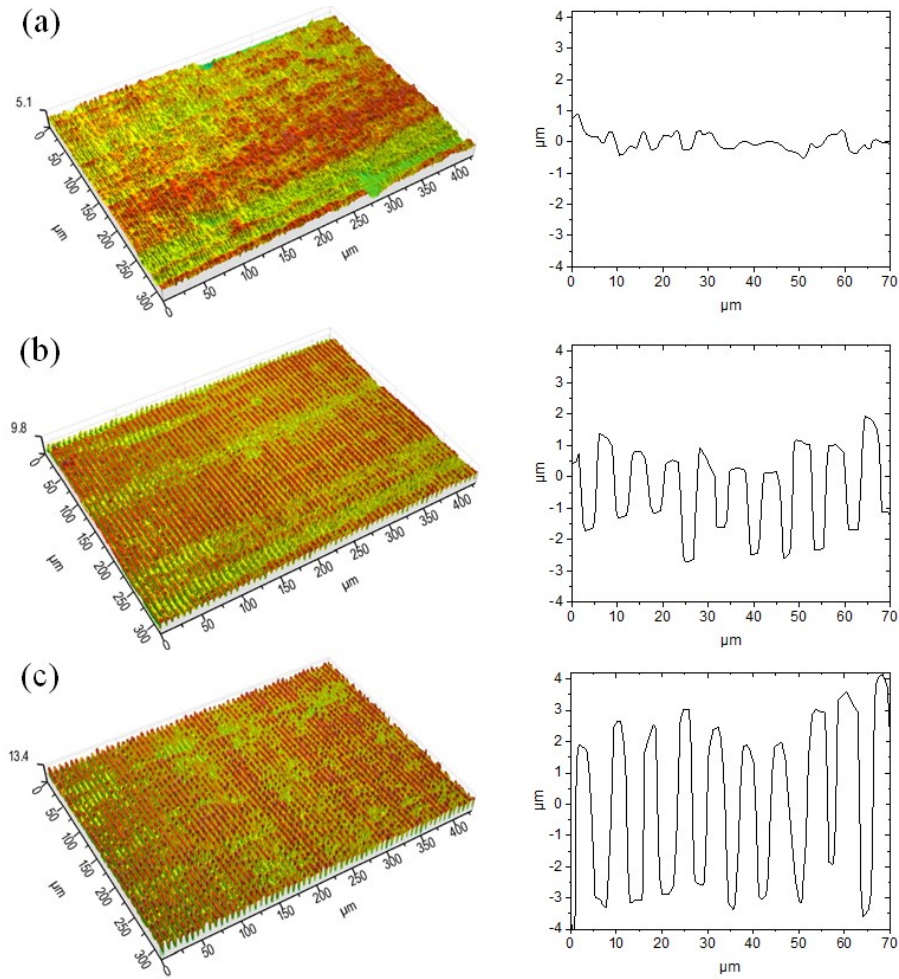
Fig. 17. White light interferometry images and typical roughness profiles of the nanosecond DLIP structures produced on Ti6Al4V using the Λ= 7.20 µm, the h = 43.20 µm, OV = 90.0 % and the (a) F = 1.06 J/cm^2 (b) F = 1.15 J/cm^2 (c) F = 1.42 J/cm^2.

Furthermore, the variation of the hatch distance was included in order to study its impact on the microstructure height fabricated. The $Rc\Lambda$ evolution values as a function of the laser fluence is presented in Fig. 18 (a), Fig. 18 (c) and Fig. 18 (e) for hatch distances of h = 43.20 µm, h = 36.00 µm and h = 28.80 µm, respectively. The OV value of 98.5 % (corresponding to 70 pulses per area) and the F = 1.34 J/cm^2 was also included.
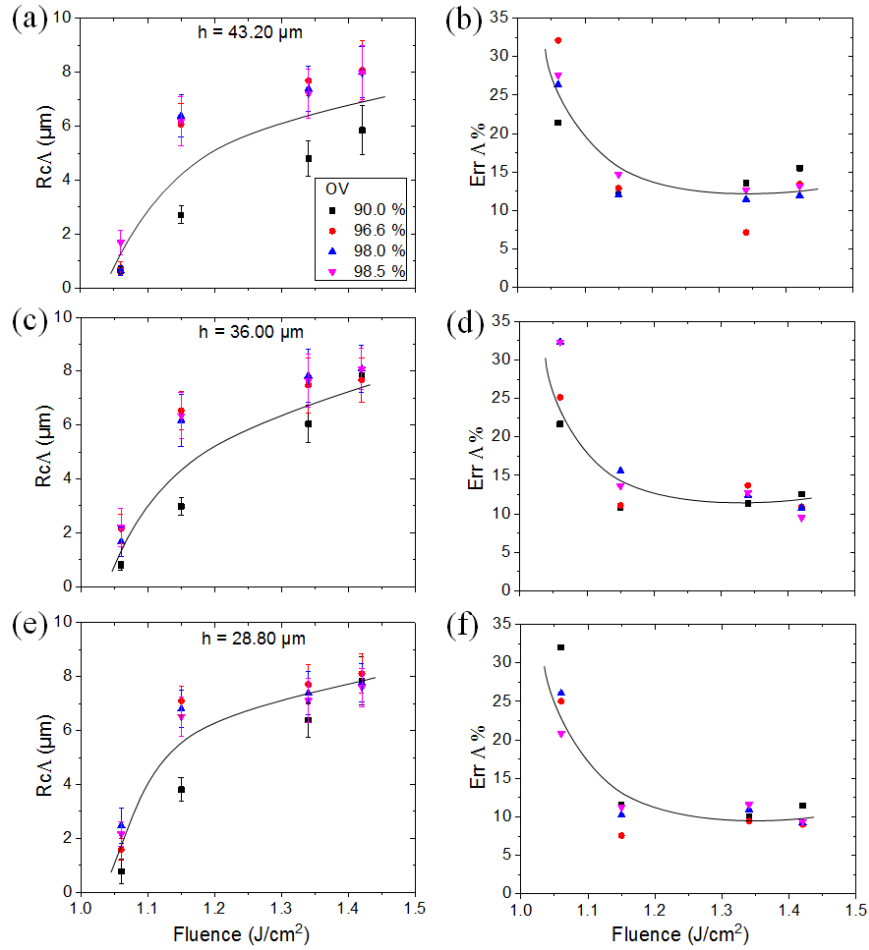
Fig. 18. Mean structure heights ($Rc\Lambda$) of produced structures on Ti6Al4V as function of the laser fluence using the Λ= 7.20 μm and the h of a) 43.20 μm, c) 36.00 μm and e) 28.80 μm, the relative error ($Err\Lambda$ %) for each microstructure produced is shown in (b) (d) (f), respectively. The overlap OV values were 90.0 %, 96.6 %, 98.0 % and 98.5 %. The continuous line is just to guide the eye.

In general, it can be observed that the increase of fluence values, results also in an increase in the structure height. For instance, surfaces irradiated using the $F = 1.06$ J/cm^2 result in heights below 2 μm, while the $F = 1.42$ J/cm^2 increases the mean structure height to about 8 μm. On the other hand, fixing the laser fluence and successively increasing the overlap over 96.6 % did not produce remarkable differences in the resulting structure heights, showing that the structure height remains almost constant for a certain number of laser pulses. Using Eq. 21, the relative error correlated to the DLIP periodic structure (denoted as $Err\Lambda$ %) was determined which connects the variation of the average structure height (standard deviation) to the mean structure height ($Rc\Lambda$) along the roughness profile. The results of $Err\Lambda$ % are shown in Fig. 18 (b), Fig. 18 (d) and Fig. 18 (f) for hatch distances of $h = 43.20$ μm, 36.00 μm and 28.80 μm, respectively. It can be observed, a decrease of the $Err\Lambda$ % connected with the increase of laser fluence as well as by reducing the hatch distance. Relative structure errors $Err\Lambda$ % as low as 15 % were achieved for fluence values higher than $F = 1.15$ J/cm^2 and $h = 28.80$ μm. The low $Err\Lambda$ % is translated directly into a surface homogeneity of 85 %.

A reduction of the *ErrΛ %* values could be achieved for laser fluence values higher than $F = 1.15$ J/cm^2 combined with OV values over 90 %. This reduction can be attributed to an increase of the *RcΛ* value compared to the standard deviation (Sd) (see Eq. 21) and thus leading to more homogenous profiles. The samples treated with $F = 1.06$ J/cm^2 revealed higher values in the *ErrΛ %* (up to 32 %), related with less homogeneous microstructures.

For the subsequent experiments, the variation of the angle of incidence (θ) is considered and two additional spatial periods of 5.82 µm and 4.31 µm were selected, using *h* values of 40.74 µm and 43.10 µm, respectively. The hatch distances were selected in order to keep them as close as possible to the value of 43.20 µm associated with the hatch distance used in the first set of experiments ($\Lambda = 7.20$ µm). The characterised *RcΛ* values of the produced microstructures are shown in Fig. 19 (c) and Fig. 19 (e). Fig 19 (a) was previously presented; nevertheless, it is included in order to be compared with the fabricated heights of the two additional spatial periods.
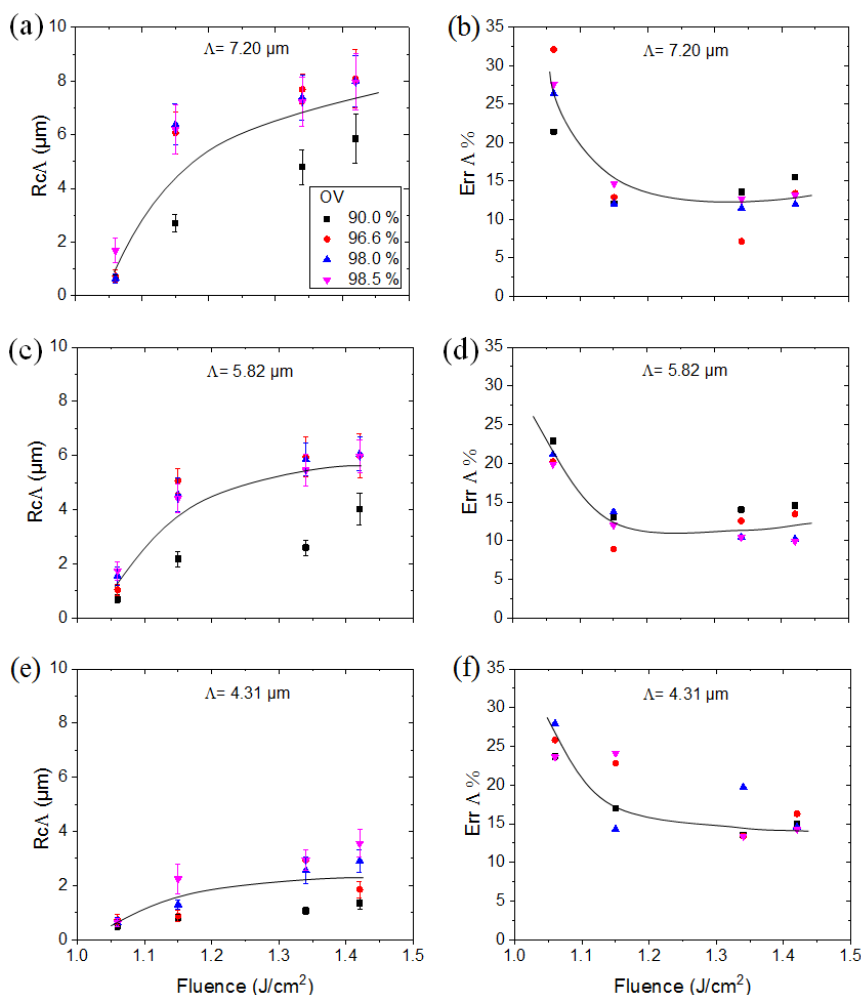

Fig. 19. Mean structure heights (*RcΛ*) of produced structures on Ti6Al4V as function of the laser fluence variation for the (a) Λ = 7.20 µm, (c) Λ = 5.82 µm and (e) Λ = 4.31 µm (*h* were 43.20 µm, 40.74 µm and 43.10 µm, respectively). The OV values were 90.0%, 96.6%, 98.0% and 98.5%. The variation of the structure height for the periodic structure (relative error, *ErrΛ %*) are shown for the same spatial periods: (b) Λ = 7.20 µm, (d) Λ = 5.82 µm (f) Λ = 4.31 µm. The continuous line is just to guide the eye.

In Fig. 19 can be observed that smaller heights were fabricated for the spatial periods of $\Lambda = 5.82\ \mu m$ and $\Lambda = 4.31\ \mu m$, in comparison with the heights for the $\Lambda = 7.20\ \mu m$. This effect is explained according with the different temperature gradients (temperature difference between interference maxima and minima positions over the spatial period) that are generated when the spatial period is varied. If a material is irradiated with an interference pattern, the surface is first locally heated at the interference maxima and if the energy is high enough the material is molten (or even ablated). Depending on the pulse duration, the energy located at the interference maxima might have enough time to flow to the colder regions, which are the interference minima positions. The distance in which the material is affected thermally can be described by the thermal diffusion length, which in the case of 10 ns pulses on Ti6Al4V has a value ~ 185 nm which correspond to a minimum spatial period about of 0.4 μm (on metals varies between 0.3 and 1 μm [132]). For the experiments conducted, it means that using high overlap values with short spatial periods, the interference minima positions can be significantly heated and thus reducing the thermal gradient. This reduces Marangoni convection which is characterised by a flow of the molten metal from the hot (maxima) to the cooler regions (minima). Other factor influencing the microstructure height is the evaporated material at the interference minima, thus the obtained structure height depends not only on the Marangoni and recoil pressure but also if the temperature at the minima positions is over the boiling point.

Although the microstructure height is different for the used spatial periods, the outcomes of *ErrΛ %* for the $\Lambda = 5.82\ \mu m$ (Fig. 19 (b)) and $\Lambda = 7.20\ \mu m$ (Fig. 19 (d)) are comparable. On the other hand, for the surfaces treated with the $\Lambda = 4.31\ \mu m$ (Fig. 19 (f)), the smallest error was about 15 % (for $\Lambda = 7.20\ \mu m$ and 5.82 μm, error values of ~10 % were measured). A typical structure obtained for the smallest period is shown in Fig. 20, corresponding to OV = 98.5 %, $F = 1.42\ J/cm^2$ and $h = 43.10\ \mu m$. In Fig. 20, it can be seen several irregularities, nevertheless the *RcΛ* = 3.36 μm was achieved. The effect involves the decrease in the thermal gradient with the reduction in the spatial period, as explained before, as well as possible vaporization of the material which promotes a recoil pressure involving a turbulent flow of the molten material [100], [219]. In the inset picture in Fig. 20 is evidenced the irregularities along the line-like structure which are not continuous and well defined, it affects the standard deviation and finally the *ErrΛ %.*
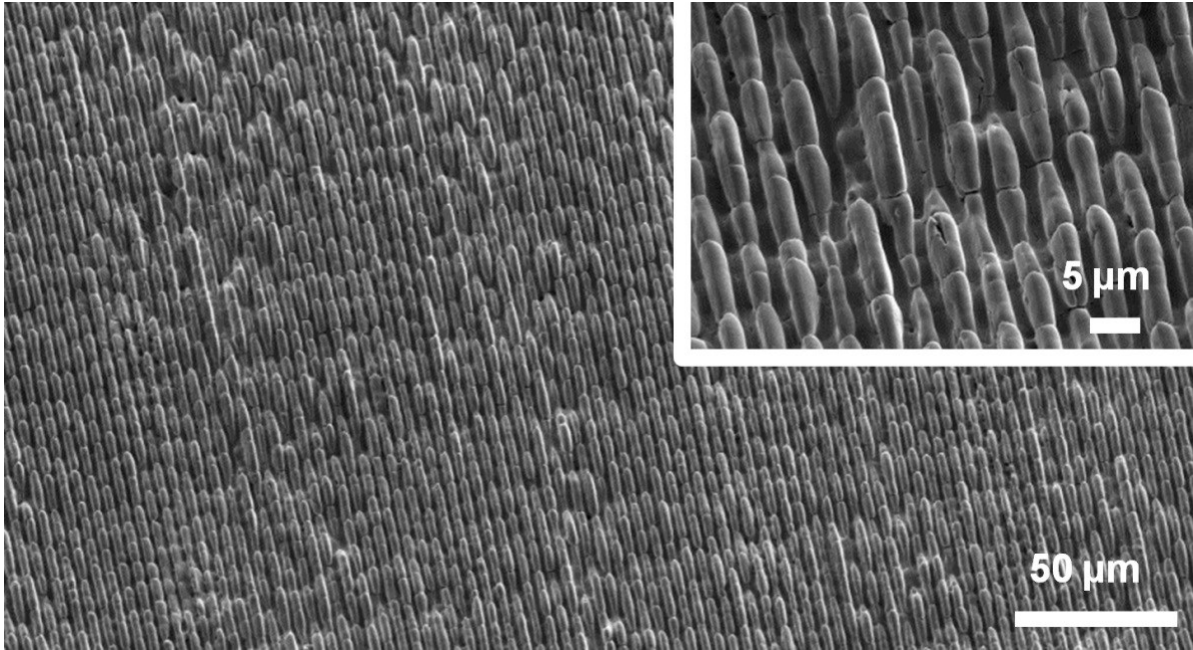
Fig. 20. Scanning electron micrograph of ns-DLIP treated Ti6Al4V surface using a spatial period $\Lambda = 4.31$ μm, $F = 1.42$ J/cm^2, OV = 98.5 % and $h = 43.10$ μm.

In addition, to the characteristic periodic microstructure produced by the interference pattern, also a second modulation of the structure topography could be observed for the used hatch distances (~ 41 μm). An example of a typical structure is shown in Fig. 21 (a), corresponding to $\Lambda = 7.20$ μm, with a $h = 43.20$ μm, $F = 1.42$ J/cm^2 and OV = 96.6 %. Although the structure mean height ($Rc\Lambda$) obtained was approximately 8 μm with an $Err\Lambda$ % of only ~12 %, the second modulation is very pronounced. This characteristic topography can be explained by the intensity distribution of the interference patterns that is obtained when two Gaussian beams (TEM00) are overlapped [27]. Therefore, the cumulative energy at the centre of the interference area is strongly affecting the quantity of molten and ablated material during the movement of the substrate in the y direction, producing the repetitive valleys. In addition, the repetitive length of this modulation was 43.20 μm, which is clearly related with the hatch distance used in this case. This value was measured using an erosion filter of 8 μm in diameter (value higher than the spatial period) during the surface analysis which permitted remove the periodic structure produce by the interference pattern (see inset in Fig. 21 (a)).
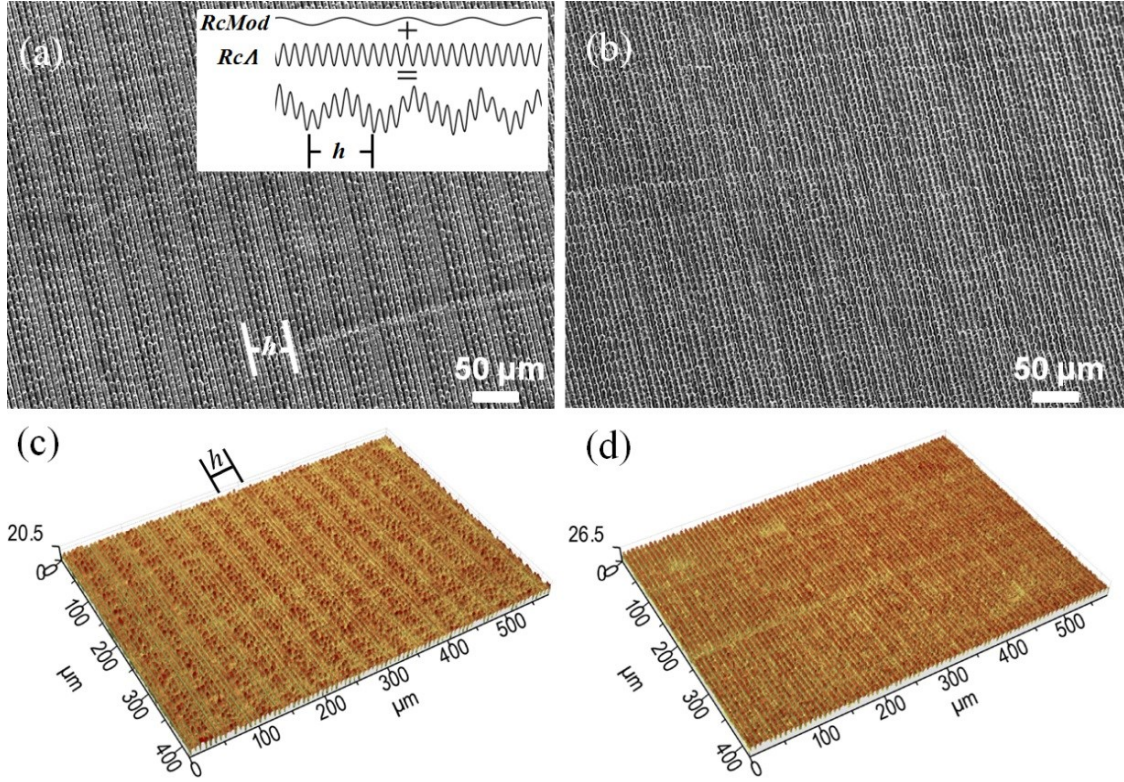
Fig. 21 Scanning electron micrographs of the ns-DLIP structures on Ti6Al4V using a spatial period Λ= 7.20 µm and F= 1.42 J/cm^2 at (a) OV = 96.6 % and h = 43.20 µm and (b) OV = 98.8 % and h = 28.80 µm, (c) and (d) shows the confocal images respectively.

As it was presented in Fig. 18, the hatch distance can be the decisive factor to increase the homogeneity, in this context, the Fig. 21 (b) is included where the h value of 28.80 µm was used. It can be observed that second modulation is less pronounced for the microstructures fabricated using the lower hatch distance value. WLI images of each surface are depicted in Fig. 21 (c) and (d), where can be also appreciated the repetitive valleys of the second modulation for the structure fabricated with a larger hatch distance. Hence, for determining the general surface texture homogeneity, this second modulation must be considered.

For quantitatively determining the surface texture homogeneity of the produced periodic patterns, a comparison between the *RcMod* (mean height of second modulation) and *RcΛ* (mean structure height produced by DLIP) was performed. This comparison determines which height is predominant. For example, surface patterns with high *RcΛ* and small *RcMod* denote a very pronounced periodic structure compared to the height of the large modulation. Thus, in this case the patterns will show a better homogeneity. Therefore, this strategy can be used to determine the surface error (*Surf Err %*) of the treated area using Eq. 23:

$$Surf\,Err\,\% = 100 \cdot \frac{RcMod}{Rc\Lambda} \tag{23}$$

In a first evaluation for structures fabricated using the $\Lambda = 7.20$ μm the *RcMod* values were obtained and plotted in Fig. 22 (a), Fig. 22 (c) and Fig. 22 (e) for the hatch distances of 43.20 μm, 36.00 μm and 28.80 μm, respectively. The decrease in the hatch distance induced a reduction in *RcMod* when fluence values over 1.40 J/cm^2 were used. Moreover, the resulting *Surf Err%* values are presented for each of the hatch distances in Fig. 22 (b), Fig. 22 (d) and Fig. 22 (f). The observable trend shows that *Surf Err%* values below 15 % can be accomplished if the lowest hatch distance is employed. For hatch distances of 36.00 μm and 43.20 μm, the *Surf Err%* values remain above 20 %. The error bars were estimated based on the error propagation method.
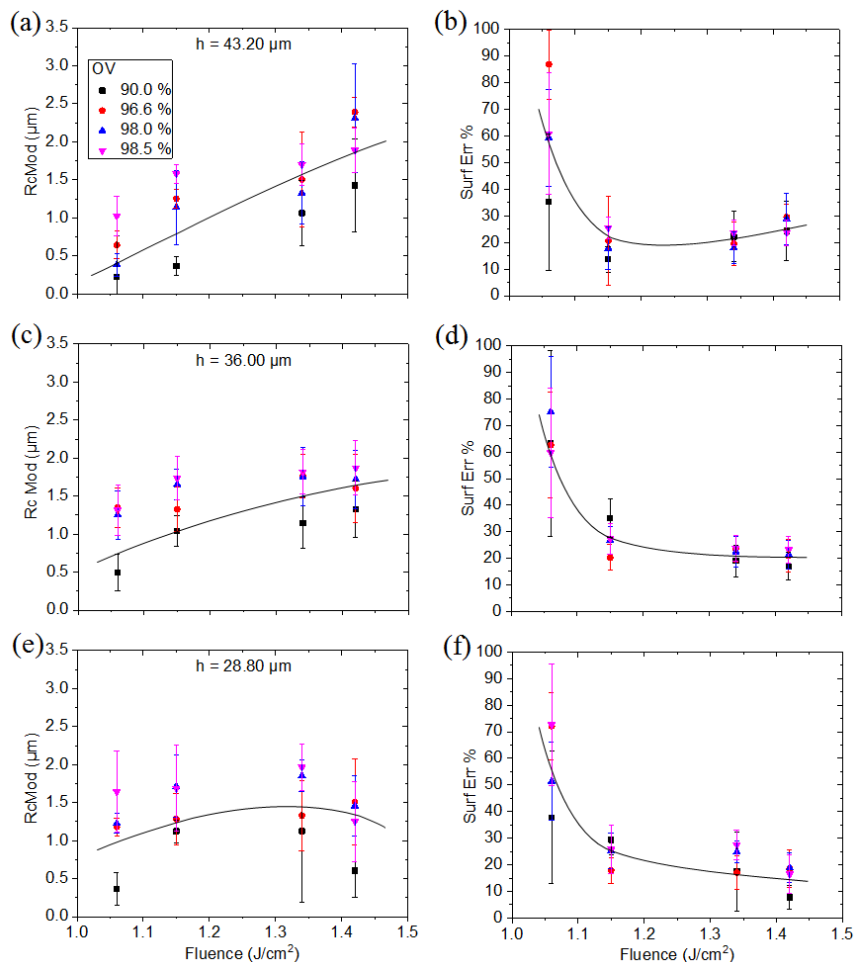

Fig. 22 Mean height *RcMod* of the second modulation as function of the laser fluence for the structures fabricated with the $\Lambda = 7.20$ μm using h values of (a) 43.20 μm, (c) 36.00 μm and (e) 28.80 μm. The OV values are 90.0 %, 96.6 %, 98.0 % and 98.5 %. The surface errors (*Surf Err %*) are shown for the same values of *h* (b) 43.20 μm, (d) 36.00 μm and (e) 28.80 μm. The continuous line is as guide the eye.

In order to better understand the role of the processing parameters in relation with the spatial period, the same analysis was carried out for the microstructures fabricated with the $\Lambda = 5.82$ μm (using an erosion filter = 6.5 μm) and $\Lambda = 4.31$ μm (using an erosion filter = 5 μm). Fig. 23 shows the mean height of this modulation (*RcMod*) for the spatial periods of $\Lambda = 7.20$ μm (Fig. 23 (a)), $\Lambda = 5.82$ μm (Fig. 23 (c)) and $\Lambda = 4.31$ μm (Fig. 23 (e). The hatch distances were for Fig. 23 (a), (c)

and (e) 43.20 µm, 40.74 µm and 43.10 µm, respectively. For each spatial period, the OV values were varied from 90 % to 98.5 %. The results show significant differences in the *RcMod* values depending on the spatial period and fluence values. In the case of the structures produced with Λ = 7.20 µm, *RcMod* values up to 3.11 µm were measured, while for Λ = 4.31 µm the maximum *RcMod* was 0.80 µm (both cases using values of OV = 98.5 % and F = 1.42 J/cm^2). In consequence, it can be concluded that a reduction of the spatial period is also related to a less pronounced topography corresponding to the larger modulation (*RcMod*).

Furthermore, the same analysis was carried out for a significant shorter hatch distances. The results are also presented in Fig. 23, for the same spatial periods (7.20 µm, 5.82 µm and 4.31 µm) and hatch distances of h = 28.80 µm (Fig. 23 (b)), h = 29.10 µm (Fig. 23 (d)) and h = 25.80 µm (Fig. 23 (f)). The same laser fluences values and OV as in the previous case were used.
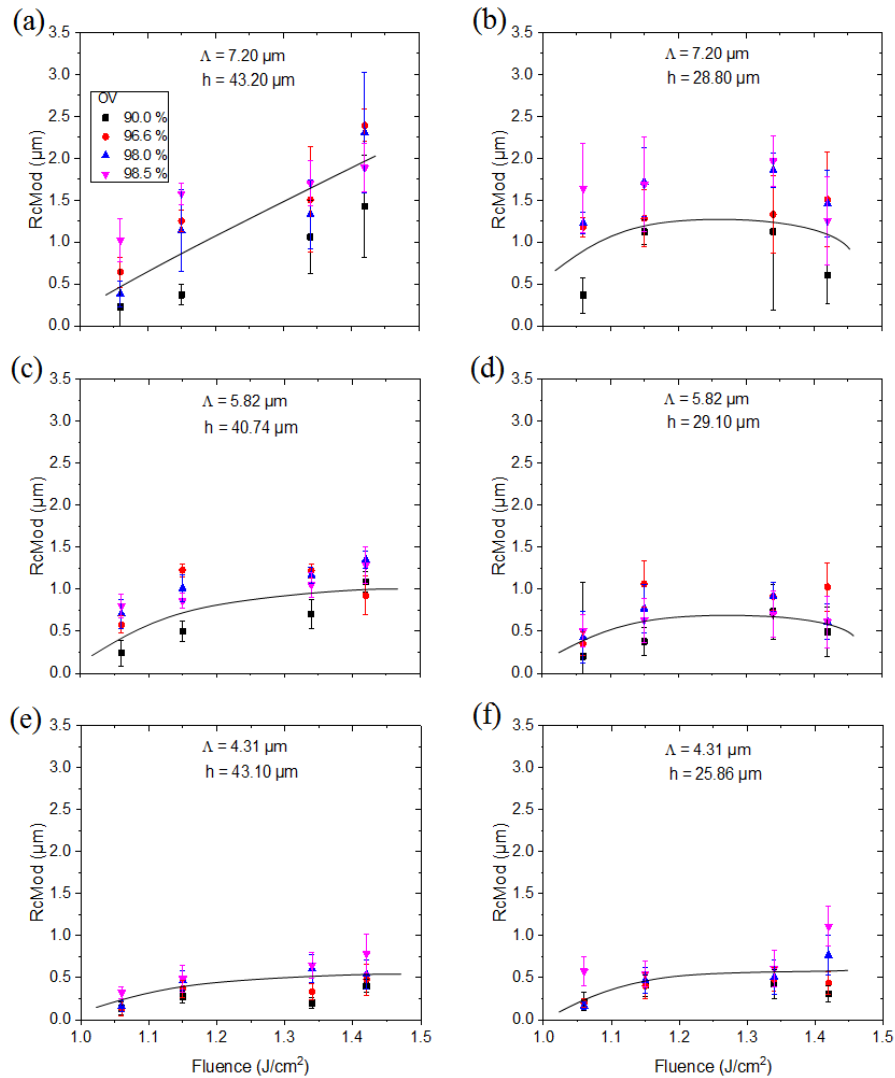

Fig. 23. Mean structure height produced by the second modulation (*RcMod*) of microstructures fabricated on Ti6Al4V using ns-DLIP. The used spatial periods were: Λ= 7.20 µm with h values of (a) 43.20 µm and (b) 28.80 µm; Λ= 5.82 µm with h values of (c) 40.74 µm and (d) 29.10 µm; and Λ= 4.31 µm with h values of (e) 43.10 µm and (f) 25.86 µm. The used OV values were 90.0 %, 96.6 %, 98.0 % and 98.5 %. The continuous line is just to guide the eye.

The results show that the *RcMod* height increases with increasing the laser fluence but apparently only for the larger hatch distances (~ 42 µm). For the shorter values (~ 28 µm) no marked trend is visible. Furthermore, comparing the *RcMod* values for the Λ = 7.20 µm with the *h* values of 43.2 µm in Fig. 23 (a) and 28.8 µm in Fig. 23 (b), it can be seen that the values for the shorter hatch distance are slightly smaller, especially for higher fluences (e.g. F = 1.42 J/cm²). Clearly, smaller *RcMod* values denote a more homogenous microstructure since the second modulation is not pronounced.

Subsequently, in Fig. 24 the variation of the *Surf Err%* as a function of the laser fluence, spatial period, OV and hatch distance is presented.
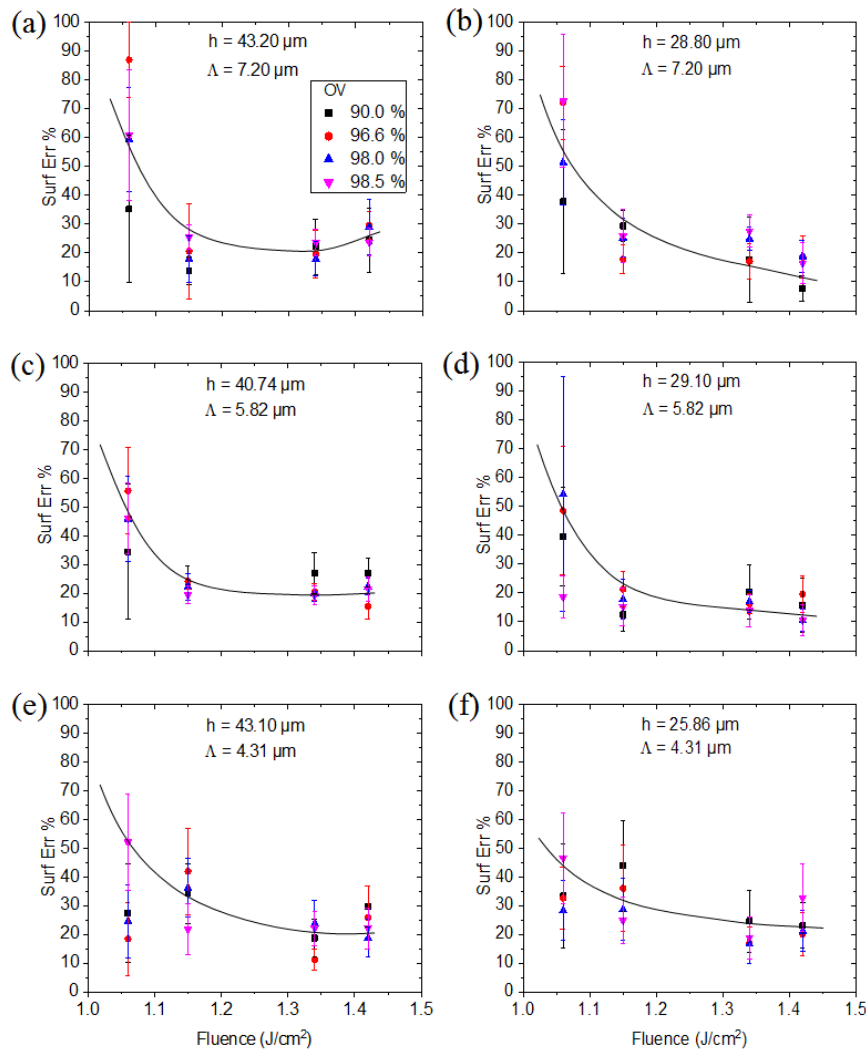

Fig. 24. Surface error (*Surf Err %*) as function of *F*, *h*, OV and spatial period. Λ= 7.20 µm with *h* values of (a) 43.20 µm and (b) 28.80 µm; Λ= 5.82 µm with *h* values of (c) 40.74 µm and (d) 29.10 µm; Λ= 4.31 µm with *h* values of e) 43.10 µm and (f) 25.86 µm. The used OV were 90.0 %, 96.6 %, 98.0 % and 98.5 %. The continuous line is just to guide the eye.

The results show that independently of the hatch distance and the OV, for low laser fluences (e.g. ~1.05 J/cm²) higher *Surf Err %* are observed (the error bars were estimated using the error propagation method). In addition, the calculated *Surf Err %* values increased for large spatial periods (e.g. 87 % for 7.20 μm and 53 % for 4.31 μm) at the same fluence values. Other characteristic that could be observed is that for shorter hatch distances, better surface texture homogeneity values could be reached, especially for larger periods (see Fig. 24 (a) and 24 (b)). The same effect is observed for high laser fluences (for example, surface errors smaller than 20 % were measured for $F = 1.42$ J/cm² and $\Lambda = 7.20$ μm).

Two scanning electron micrographs examples of the fabricated periodic microstructures using the $\Lambda = 7.20$ μm (with *Surf Err %* = 16 %) and $\Lambda = 5.82$ μm (with *Surf Err %* = 10 %) are shown in Fig. 25 (a) and Fig. 25 (b), respectively. In both case, the shortest hatch distances were employed (28.80 μm and 25.86 μm, respectively). Fig. 25 (c) and Fig. 25 (d) show the WLI images for each case. As it can be observed in the WLI images, a significant reduction of the second modulation (*RcMod*) could be achieved (compare with the WLI picture in Fig. 21(c)).
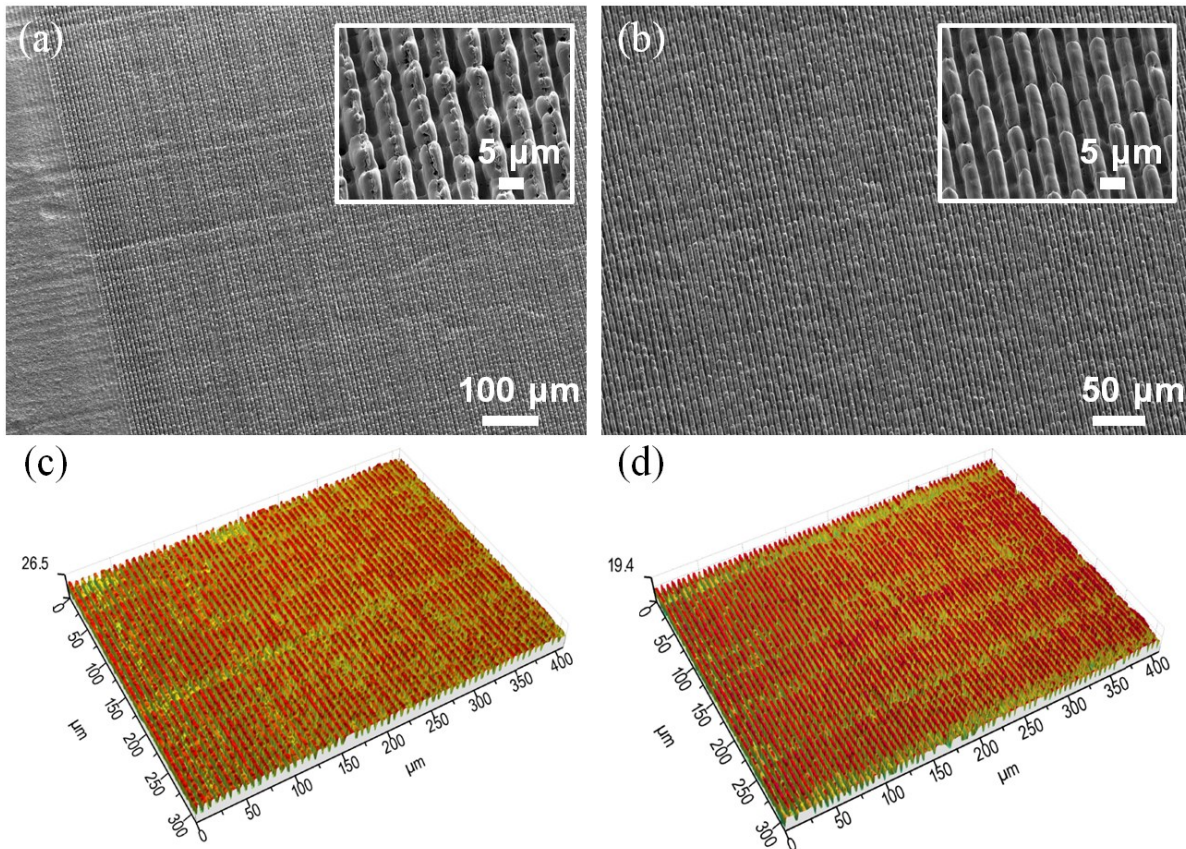

Fig. 25. (a) and (b) scanning electron micrographs of produced DLIP structures on Ti6Al4V using spatial periods of: (a) $\Lambda = 7.20$ μm ($h = 28.80$ μm), (b) $\Lambda = 5.82$ μm ($h = 29.10$ μm), in both cases the $F = 1.42$ J/cm² at OV = 98.5 %, (c) and (d) show its white light interferometry images, respectively.

As previously stated, the kurtosis (*Rku*) was calculated for all produced surface patterns. As mentioned, this parameter characterises the spread of the height distribution and is connected with the

sharpness of the roughness profile. Fig. 26 shows the outcomes for the spatial periods of 7.20 μm, 5.82 μm and 4.31 μm for the different used hatch distances.
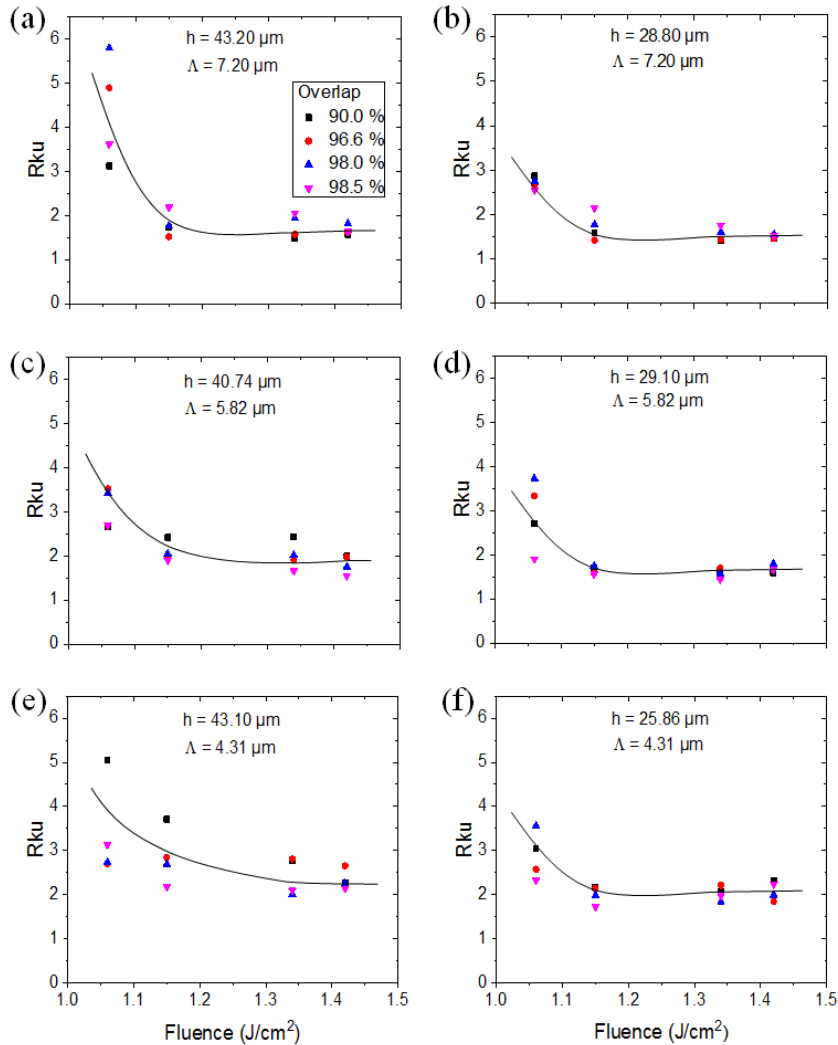

Fig. 26. Kurtosis (*Rku*) along the roughness profiles produced by ns-DLIP on Ti6Al4V in the line-like pattern as a function of *F*, using the Λ= 7.20 μm, *h* values of (a) 43.20 μm and (b) 28.80 μm, Λ= 5.82 μm, *h* values of (c) 40.74 μm and (d) 29.10 μm and Λ= 4.31 μm, *h* values of (e) 43.10 μm and (f) 25.86 μm. The OV values were 90.0 %, 96.6 %, 98.0 % and 98.5 %. The continuous line is just to guide the eye.

In general, it was observed that if fluences values lower than 1.10 J/cm^2 are used, the measured *Rku* values were higher than 2. In particular, the highest kurtosis was observed for larger periods and large hatch distances (e.g. *Rku* up to ~6 in the Λ = 7.20 μm and *h* = 43.20 μm). For higher laser fluences (*F* > 1.15 J/cm²) the kurtosis values were significantly lower (~ 1.5). Furthermore, for the structures fabricated with the smaller hatch distances the dispersion of the *Rku* values was reduced, which means that the obtained characteristic surface morphology do not varies. In addition, a perfect sinus profile has a *Rku*= 1.5, shape that is comparable to the obtained topographies [220]. However, it has to be commented that other profiles might lead to similar results and thus this parameter is insufficient to describe a topography shape.

Finally, an example of the fabricated surfaces is shown in the WLI image in Fig. 27 (a), for a surface treated using a $\Lambda = 7.20$ µm, OV = 96.60 %, with the h value of 43.20 µm and $F = 1.15$ J/cm^2. Fig. 27 (b) shows the WLI profile (profile A-A′ Fig. 27 (a)) of a partial untreated material surface and the treated area, where the structure height of the material redeposited can be compared with the untreated area surface at the left side of the profile. As it can be noticed, about 50 % of the structure height was redeposited. Furthermore, Fig. 27 (c) shows a smaller profile B-B′ (~ 65 µm in length) extracted from Fig. 27 (a). Typically, similar profiles with different heights were acquired along all the microstructures produced. However, when a *Rku* value close to 1.5 is obtained (like this specific microstructure shown in Fig. 27 (a)) a bimodal distribution shown in Fig. 27 (d) can be observed, the histogram represents the distribution in a profile taken without considering the untreated area. The histogram is built by plotting the number or fraction of surface heights lying between two specific heights as a function of height [221]. The material in the upper and lower part of the profile promotes the reduction of the scores in the tails in the distribution graph (see Fig. 27 (d)) with a tendency to kurtosis value of 1.5, explained by the induction of smooth surfaces on the interference minima and maxima positions of the microstructures.
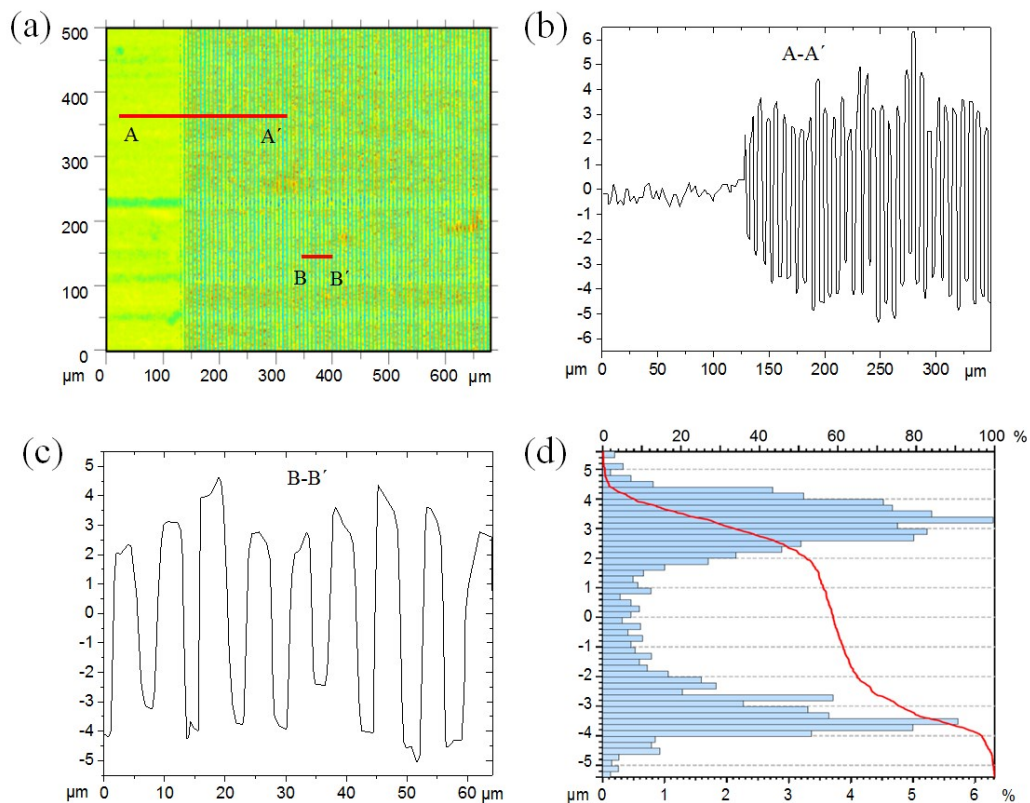

Fig. 27. (a) WLI image of the surface treated by ns-DLIP on Ti6Al4V in the line-like pattern, using $\Lambda = 7.20$ µm, with the $h = 43.20$ µm, OV = 96.6 % and $F = 1.15$ J/cm^2. (b) Roughness profile A-A′ which depicts the edge between the DLIP area and the material untreated surface. (c) Partial roughness profile B- B′ which depicts the material redeposited and (d) its statistical representation as height distribution from a profile with sample length of 2.75 mm with its cumulative distribution curve.

5.2 Interference structuring of stainless steel using picosecond laser pulses

In a first approach, the effect of using a single-pulse ps-DLIP in the two-beam configuration on stainless steel (1.4016) was investigated. The laser set up was configured to the spatial period of $\Lambda = 5.20$ μm, a diameter of the laser interference area (Ø) of 285 μm which results in a $F = 0.56$ J/cm². Fig. 28 (a) shows the SEM image for a resulting pixel with a Gaussian interference distribution, the magnification in Fig. 28 (b) reveals a detailed view of inference maxima and minima in the line-like pattern produced.
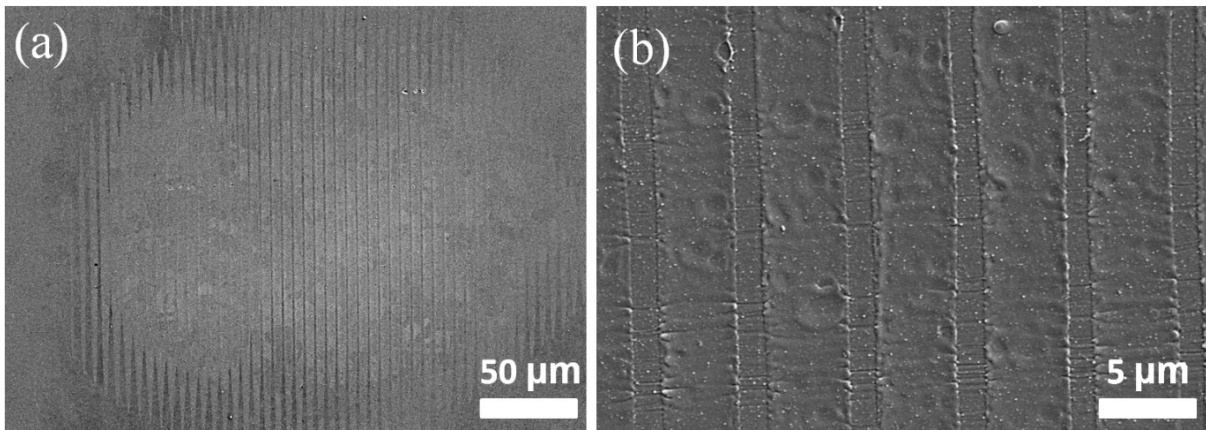

Fig. 28. Scanning electron micrographs of single-pulse ps-DLIP on stainless steel using the $\Lambda = 5.20$ μm, $F = 0.56$ J/cm², at the $f = 1$ kHz and $\tau = 10$ ps.

In Fig. 28 (b) it is recognizable molten material at the interference maxima. It supports the premise that thermal effects cannot be completely ruled out on metals when picosecond pulses are used [222]. However, it must be highlighted that the photophysical mechanism is prone during the ps-DLIP due to the ultrashort pulse time regime (10 ps).

5.2.1 Fabrication of hierarchical periodic micro/nanostructures

In a second set of experiments, line-like structures with two different spatial periods ($\Lambda = 2.60$ μm and $\Lambda = 5.20$ μm) were produced considering a constant diameter of the interference area (Ø) of 160 μm, $F = 1.45$ J/cm² and OV values ranging from 0 % to 99 % on stainless steel (1.4016). Scanning electron microscope images of characteristic treated samples are shown in Fig. 29. As it can be seen, for both used spatial periods, very well defined line-like patterns could be fabricated. In general, it can be observed that for samples treated with higher OV values, the patterns are more pronounced since larger structure depths are produced. For example, in Fig. 29 (a) and 29 (b), the OV = 91 % was used obtaining structure depths of 600 nm and 750 nm for the $\Lambda = 2.60$ μm and $\Lambda = 5.20$ μm, respectively. In contrast, the produced structures with an OV = 99 % have average depths of 4.9 μm and 2.5 μm for the $\Lambda = 5.2$ μm (Fig. 29 (d)) and $\Lambda = 2.6$ μm (Fig. 29 (c)),

respectively. Using this information, the AR of 0.87 and 0.96 can be calculated for $\Lambda = 5.20$ μm and $\Lambda = 2.60$ μm at OV = 99 %, respectively.
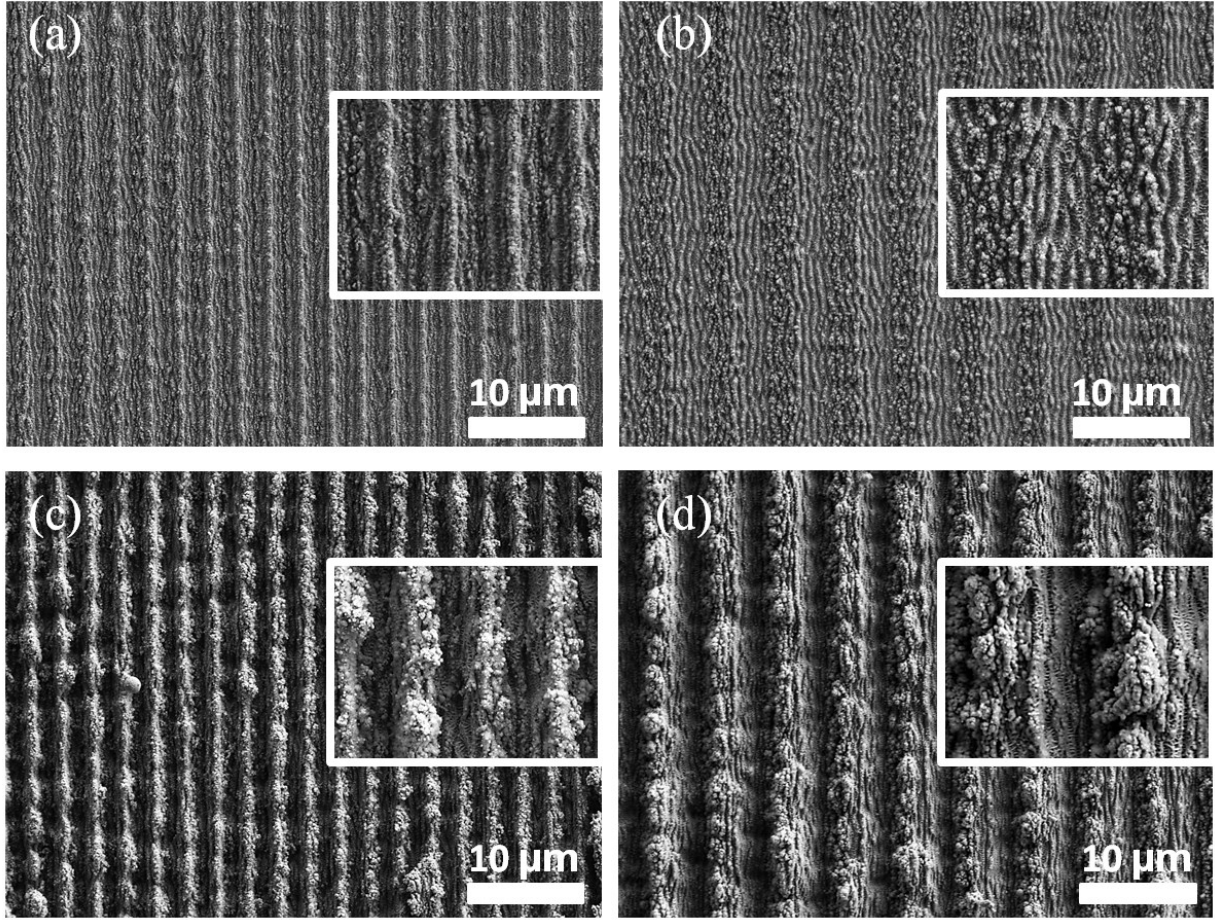

Fig. 29. Scanning electron micrographs of the line-like microstructure produced by ps-DLIP using a $F = 1.45$ J/cm^2. (a) $\Lambda = 2.60$ μm and (b) $\Lambda = 5.20$ μm at OV = 91 %. (c) $\Lambda = 2.60$ μm (d) $\Lambda = 5.20$ μm at OV = 99 %.

The structure depths here shown for the $\Lambda = 2.60$ μm are significantly larger than those obtained using ns-pulses for the similar spatial periods ($\Lambda < 3$ μm). This effect is explained by the reduced heat affected zone when utilizing picosecond laser pulses [22]. In this context, the heat affected zone is directly related with the thermal diffusion length and thus with the pulse duration. For the used steel, a thermal diffusion length of only 8.4 nm can be calculated for the 10 ps pulse duration (τ) using Eq. 6 (with $\lambda_{th} = 25$ W/mK, $\rho = 7.7$ g/cm^3, and $c_p = 460$ J/kg K [223]). This value is approximately 32 times shorter compared with the pulse duration of ~ 10 ns ($l_T \sim 266$ nm). The smallest spatial period achievable during a DLIP process is about twice the thermal diffusion length [130]. Thus, for the 10 ns pulse duration, this theoretical value is approximately 531 nm. According to experimental observations, generally structure depths of some tens of nanometres (40-60 nm) can be achieved in different metallic substrates for spatial periods smaller than 2.5 μm when using a pulse duration of 10 ns [224]. These significant differences in the structure depth can be only explained by a stronger selective local ablation (evaporation) of the material at the interference

maxima positions for the ps-DLIP since the heat introduced by the laser cannot be evacuated by thermal conduction.

In addition to the line-like periodic structure produced by the interfered laser beams, also additional features could be found at the laser treated surfaces. For example, in Fig. 29 (b) ($\Lambda = 5.20$ μm) an arrangement of periodic lines with a lateral spacing of approximately 700 nm over the interference structures are evident. Furthermore, these structures are oriented perpendicular to the polarization of the laser beam and their size does not change with the used laser processing parameters. Due to observed characteristic size and orientation of these features and taking into consideration the used $\lambda = 1064$ nm and $\tau = 10$ ps, these features can be identified as Low Spatial Frequency Laser-Induced Periodic Surface Structures (LSFLs) [140].

After these first impressions of the DLIP process using a picosecond laser source, a systematic analysis was carried out, in order to determine the dependence between the used processing parameters and the structure depth of the produced patterns. The laser fluence was kept constant at $F = 1.45$ J/cm² as well as h with a value larger than the interference area (200 μm) to avoid overlap in the x-direction perpendicular to the orientation of the line-like patterns. This dependency is shown in Fig. 30 (a). The structure depth was measured using confocal microscopy and was calculated taking the average of five different measurements at random positions.

As it can be seen, the structure depth increases with the OV, especially in the range from 87 % to 99 % (Fig. 30 (a)). These OV values correspond to a total number of laser pulses (N) of 8 and 100, resulting in cumulative fluences of 11.6 J/cm^2 and 145 J/cm^2, respectively. In addition, it can be observed that the structure depths for both periods do not differ significantly, until approximately the OV value of 87 %.
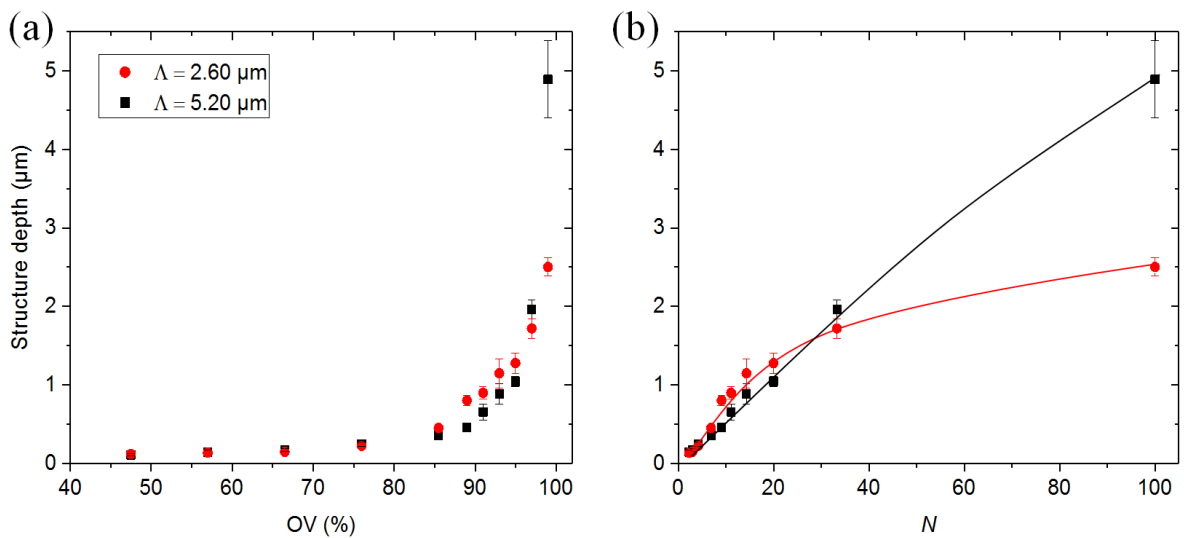

Fig. 30. Dependence of the structure depth with (a) OV and (b) N for $\Lambda = 2.60$ μm and $\Lambda = 5.20$ μm, fabricated using line-like structures by ps-DLIP on stainless steel. As a constant parameters the $F = 1.45$ J/cm², $\tau = 10$ ps and $\lambda = 1064$ nm were used. The continuous line is just to guide the eye.

The obtained experimental results can be also represented as function of N as shown in Fig. 30 (b). The results reveal an almost linear increase of the structure depth for both periods up to approximately 30 pulses. After that, for the $\Lambda = 2.60$ µm a maximal structure depth of 2.50 µm is achieved, while for the $\Lambda = 5.20$ µm the structure depth further increased up to 4.90 µm for 100 pulses. In Fig. 31 is presented the micrograph corresponding to the $\Lambda = 5.20$ µm and OV = 99 % (100 pulses), with a tilted angle of 45° in x and y which denotes the relative AR fabricated. In the inset picture the angle of 45° in x was used, it can be observed the LSFLs in parallel to the DLIP microstructures.
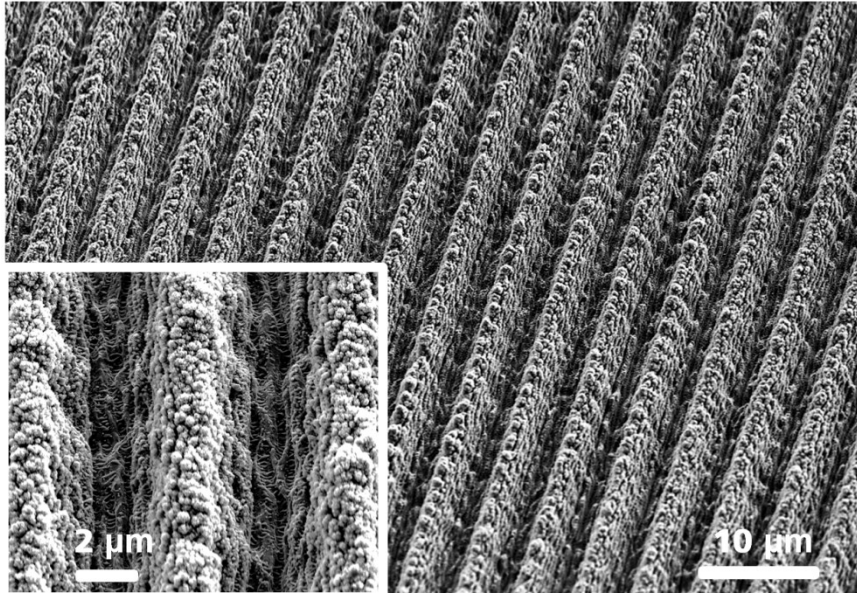
Fig. 31. Scanning electron micrograph (tilted at angle of 45° in x and y) of line-like microstructures with AR = 0.96 fabricated by ps-DLIP using OV = 99 %, $\Lambda = 5.20$ µm and $f = 1$ kHz.

Finally, two confocal microscopy images of produced line-like patterns are presented in Fig. 32 (a) and (b) structured using the $\Lambda = 5.20$ µm and $\Lambda = 2.60$ µm, respectively. As a constant parameters the OV = 97 % and $F = 1.45$ J/cm² were used.
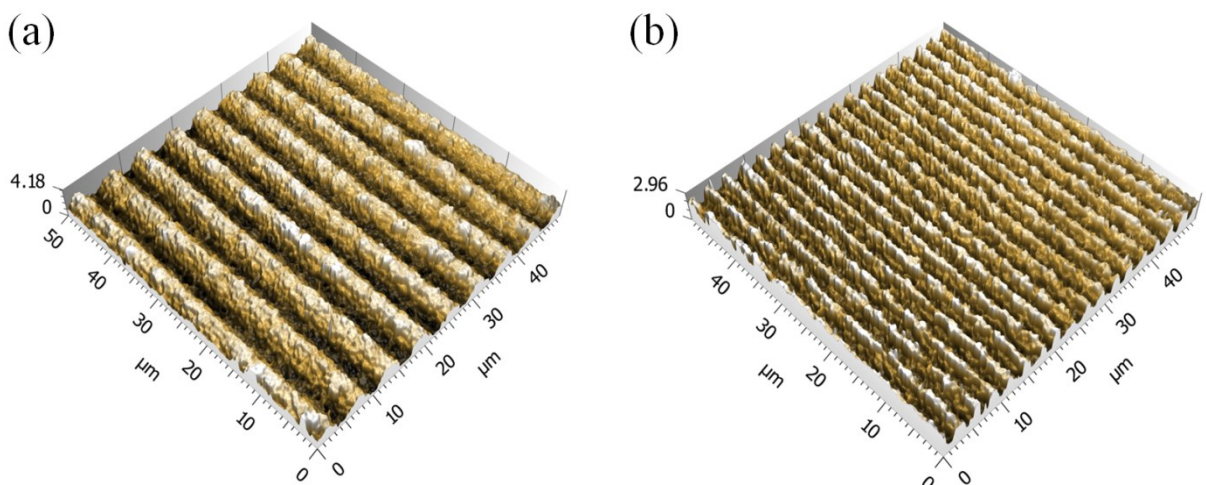
Fig. 32. Characteristic confocal microscopy images of produced line-like patterns with (a) $\Lambda = 5.20$ µm and (b) $\Lambda = 2.60$ µm. The OV = 97 % and $F = 1.45$ J/cm² for (a) and (b) were used.

5.2.2 Control of nanostructure orientation

The orientation of LIPSS is related to the direction of the laser light polarization [134], [225], [226], therefore, a change in the polarization must permit to control the orientation of the LIPSS with respect to the interference pattern. In a new set of experiments the laser beam polarization was rotated using a half-wave plate. Fig. 33 shows SEM micrographs of metallic substrates produced using a $\Lambda =$ 5.20 μm and OV = 97 % with four different linear polarization states. In Fig. 33 (a) the polarization remains perpendicular to the DLIP pattern, subsequently the polarization was rotated by 42° (compared to the patterns produced in Fig. 33 (a)), 88° and 130° for the Fig 33 (b), Fig. 33 (c) and Fig. 33 (d), respectively. These angles were chosen arbitrary. Clearly, the produced LSFL are still perpendicular to the beam polarization, for all the chosen angles.

Other set of periodic array are visible in the magnification showed in the inset pictures in Fig. 33. Since, these features are significantly smaller, with a repetitive distance around ~ 200 nm, they are named High Spatial Frequency LIPSS (HSFL). In this case HSFL are oriented parallel to the beam polarization.
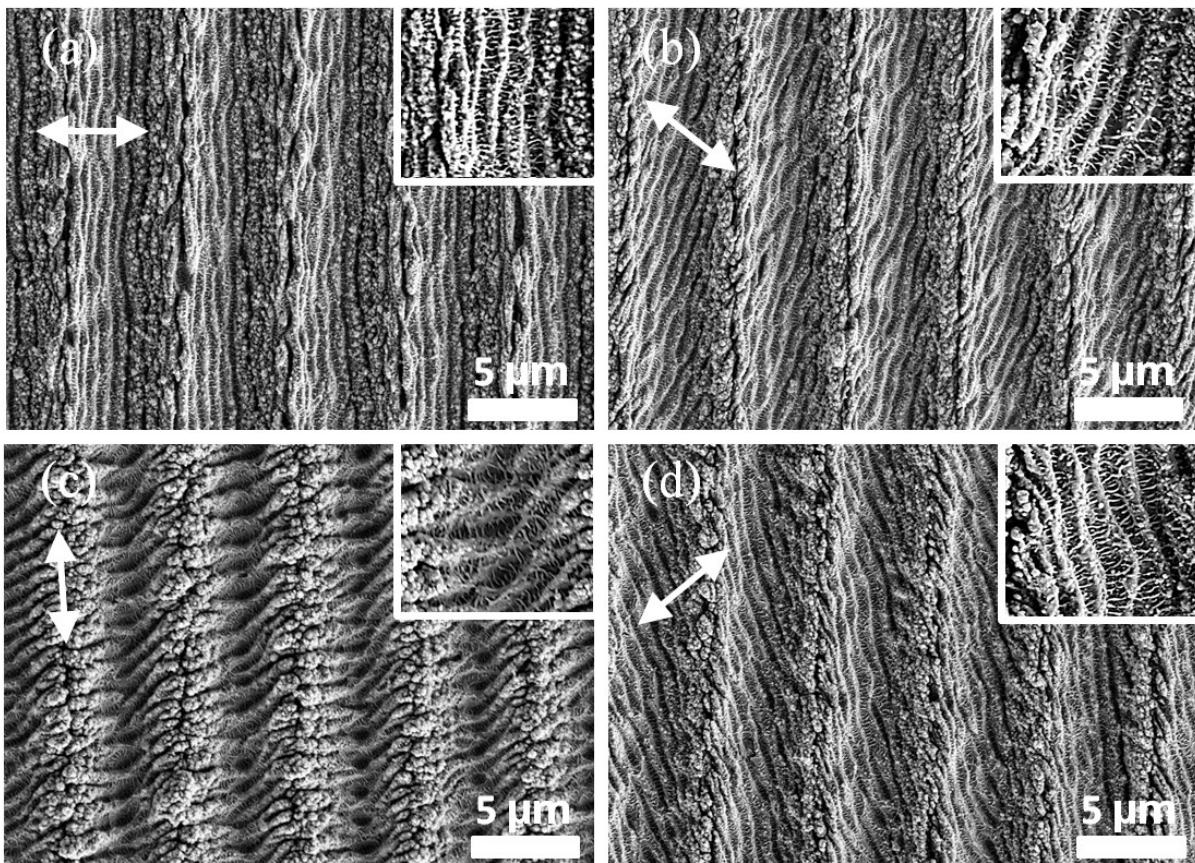

Fig. 33. Scanning electron micrographs of the line-like structure produced by ps-DLIP using a laser $F = 1.45$ J/cm^2, a $\Lambda = 5.20$ μm, processed at OV = 97 %. The polarization of the beam was (a) perpendicular to the DLIP pattern and rotated (b) 42°, (c) 88° and (d) 130°. Both LSFLs and HSFLs are visible. The arrows denote the polarization of the electric field.

In another set of experiments a zero order 1/4 wave plate was mounted in order to control the polarization of the laser beam in a circular direction. Fig. 34 shows the topography fabricated using the Λ = 5.20 μm and OV = 97 % with F = 1.45 J/cm^2. In the inset picture in Fig. 34, it can be observed that the HSFL are visible with also any determined direction. Furthermore, the LSFL are not well defined.
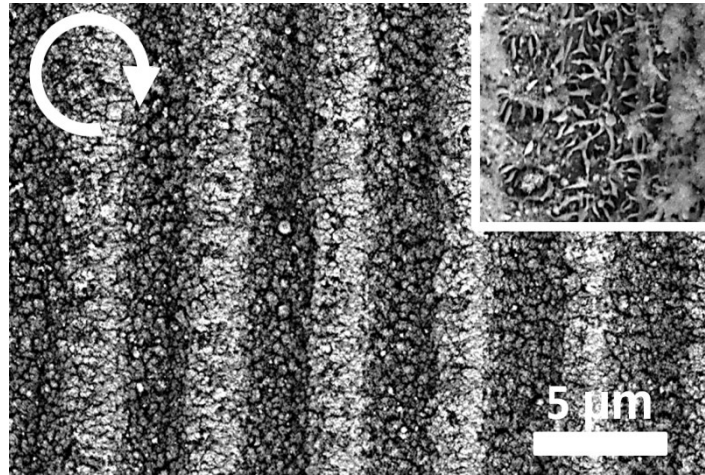

Fig. 34. Scanning electron micrographs of the line-like structure produced by ps-DLIP using the F = 1.45 J/cm^2, Λ= 5.20 μm and OV = 97 %. The circular polarization of the beam was controlled by using a zero order 1/4 wave plate. The arrow denotes the polarization of the electric field.

5.2.3 Fabrication of hierarchical pillar-like microstructures

Pillar-like structures were fabricated using ps-DLIP. As mentioned in the experimental section, these structures are produced by irradiating first the substrate with the line-like arrays and by overlapping them with a second line-like pattern before rotating the sample 90° in the *x-y* plane. For the fabrication of the first structure, the tests performed before permitted to determine the optimal conditions to produce microstructures with high AR values. Thus, the laser fluence was set to F = 1.45 J/cm² and the OV values were varied from 91% to 99 % for both used periods (Λ = 2.60 μm and Λ = 5.20 μm). Differently, for the second irradiation step, both the laser fluence and the OV were varied. Examples of produced pillar-like structures with Λ= 2.60 μm and Λ= 5.20 μm are shown in Fig. 35. In Fig. 35 (a), the spatial period was set to Λ = 2.60 μm and for the second irradiation step, the OV = 97 % using F = 1.31 J/cm². In Fig. 35 (b), the used spatial period was Λ = 5.20 μm, with a OV = 97 % and using a F = 0.85 J/cm². Both images are accompanied with a two-dimensional Fast Fourier Transform (FFT) analysis which can be used to determine the orientation and size of repetitive patterns.
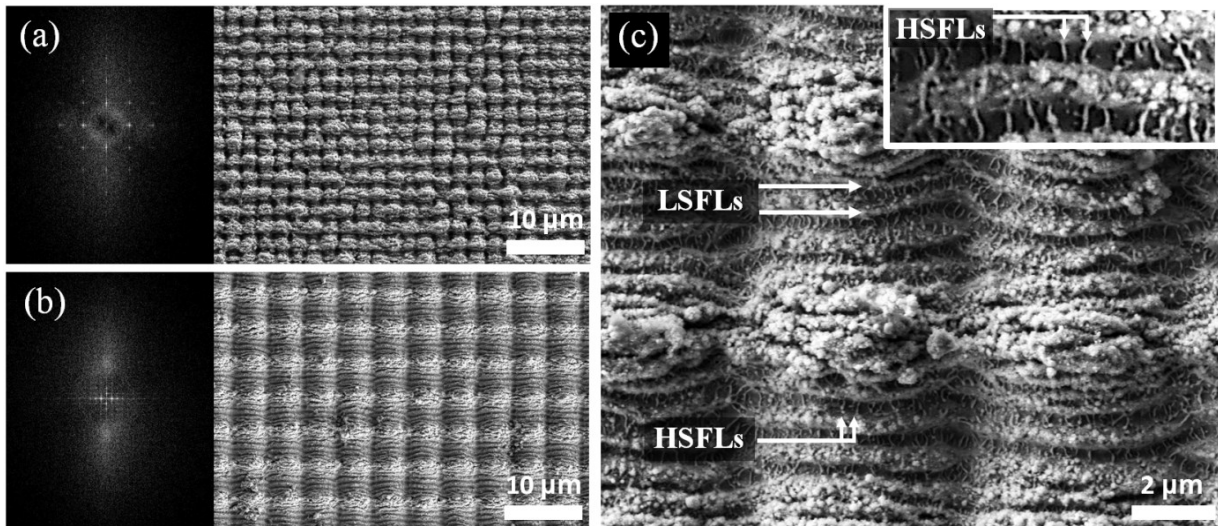
Fig. 35. Scanning electron micrographs of stainless steel samples processed by DLIP with pillar-like pattern. (a) Λ= 2.60 μm, (b) and (c) Λ= 5.20 μm. In all cases, the OV value of 97 % was used. In (a) and (b) the FFT analysis are shown. In (c), the high magnification image reveals the presence of both LSFLs and HSFLs, these last can be clearly appreciated in the inset picture.

In the FFT of Fig. 35 (b), two clouds can be observed at the top and the bottom of the image. The orientation of these clouds is perpendicular to the sub-μm features which are placed over the structure corresponding to the interference pattern. Similarly to the experiments for the line-like patterns, these structures can be described as LSFLs (type-s) [140], [227]. However, only the ripples produced in the second irradiation process are visible. The additional bright spots in the image with a rectangular arrangement result from the very symmetrical pillar-like pattern. Moreover, since these structures are bigger than the observed LIPSS, these spots are closer to the centre of the image (the distance between the spots and the central spot is inversely proportional to the characteristic repetitive distance).

In the case of Fig. 35 (a), for the pillar pattern produced with a Λ = 2.60 μm, also the clouds corresponding to the LIPSS structures are visible. However, their intensity is lower which means that these structures are not so pronounced as for the larger period. As in the previous case, very well defined bright spots with a rectangular arrangement can be observed, denoting the high quality of the structures associated with the pillar-like geometry. When analysing these structures at a high magnification, HSFL are also visible (see inset in Fig. 35 (c)). Due to the size, orientation and periodicity of these structures, it is possible to classify them as HSFLs, type-r features [140]. These nanostructures were also produced during the second irradiation step. The same structures can be also observed in the insets shown in Fig. 29 (a) and (b), where the HSFLs are also oriented parallel to beam polarization. Also in this case, a systematic analysis was carried out, in order to determine the dependence between the used processing parameters (OV and *F*) and the microstructure depth of the produced patterns. Due to the two-step irradiation process, the produced pillar-like patterns can be characterised by three different depths, corresponding to the interception of an interference maxima with an interference minima (in both *x* and *y* direction) and the interception of two interference

maxima (with theoretically the largest structure depth). For a perfect pillar structure, both depths of the positions corresponding to the maxima - minima interceptions must have similar values. On the contrary, differences between these positions denote that in the second irradiation step, the produced line-like patterns were too narrow or too high.

Measurements of the produced depths at the aforementioned positions are shown in Fig. 36 as function of OV and F during the second irradiation step (horizontal pattern). Both OV values for the first and the second irradiation steps were identical. The OV is indicated in percentage for each case in the figure.
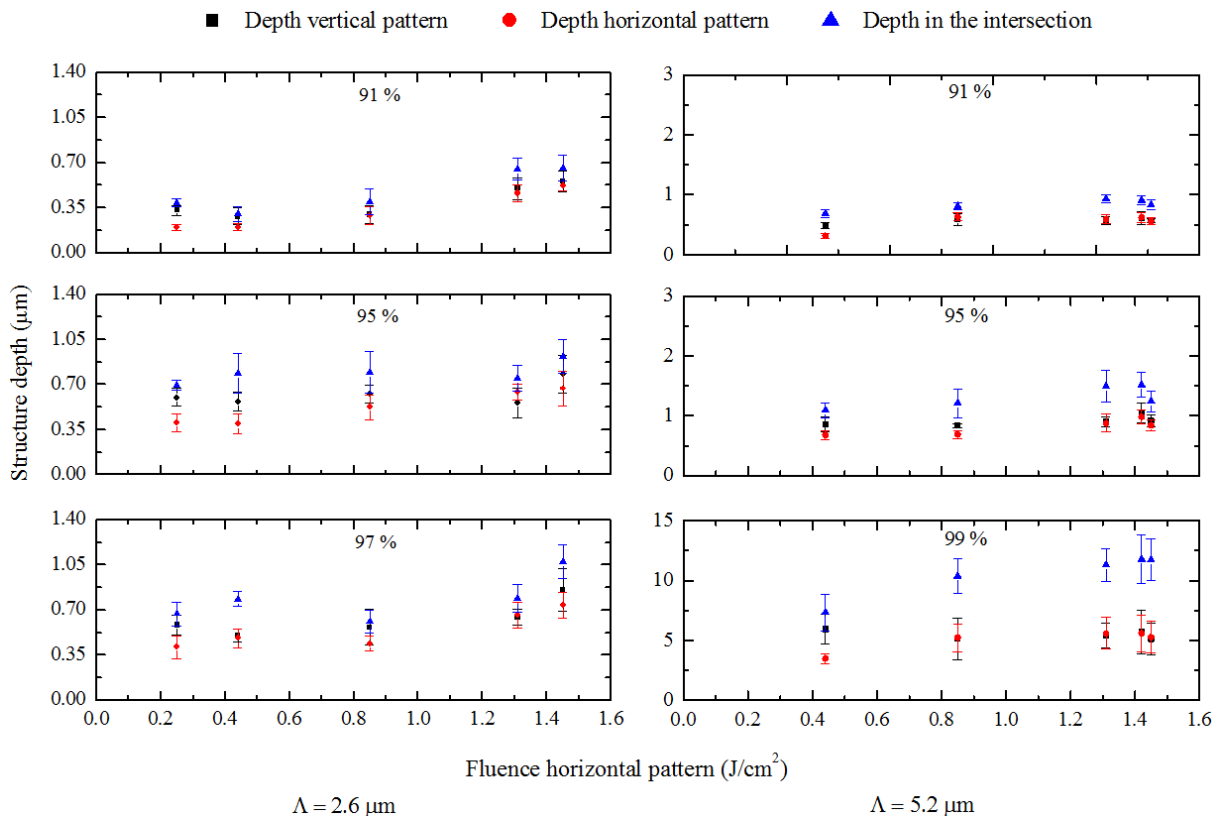
Fig. 36. Depth measurements of pillars-like structures fabricated by ps-DLIP, using the Λ = 2.60 µm, Λ= 5.20 µm. The OV values were varied between 91 % to 99 % and the values of laser fluence ranging from F= 0.25 J/cm² to F= 1.45 J/cm².

In general, an increase of the F resulted on larger structure depths. The same can be observed with increasing the OV. However, significant differences can be observed depending on the spatial period. In the case of the line-like patterns (see Fig. 30), for OV values over 91 % the measure structure depths were over ~ 1 µm for F = 1.45 J/cm². These depths could be hardly achieved, even at the interception positions of two interference maxima. Therefore, it is evident that the second irradiation step is partially destroying the first produced line-like patterns. Considering the processing parameters providing pillar-like patterns with the best quality, in several cases it was observed that the depths at the maxima - minima intersections for both irradiation directions (vertical and horizontal) were similar and the maximal structure depth was reached at the maxima - maxima interceptions. In

the case of the samples treated with OV values of 99 % using the $\Lambda = 2.60$ μm (not shown), the morphology of the DLIP treated surface was very irregular and thus the depths of the produced patterns could not be measured. In the last case, these samples were irradiated in total with $N = 200$ (100 pulses in each direction corresponding to a cumulative fluence value of 290 J/cm^2) which means that the quality of the patterns decreases with increasing N over a certain number.

In the case of the $\Lambda = 5.20$ μm, a different behaviour was observed especially when using an OV = 99 % compared to the $\Lambda = 2.60$ μm. As can be seen in Fig. 36, for F values over 1.30 J/cm², structure depths close to 5 μm can be obtained at both maxima – minima interceptions (at similar conditions, the observed structure depth for the line-like patterns was 4.9 μm) and at the maxima – maxima interceptions structure depths up to 11.5 μm could be measured. Considering that the depth at the maxima – maxima interceptions is practically two times the depth observed at the maxima – minima, it can be conclude that for this spatial period, the first irradiation process does not significantly affect the ablation behaviour during the second step. An example of a fabricated pillar-like pattern with a $\Lambda = 5.20$ μm, at OV value of 99 % and $F = 1.31$ J/cm² is shown in Fig. 37.
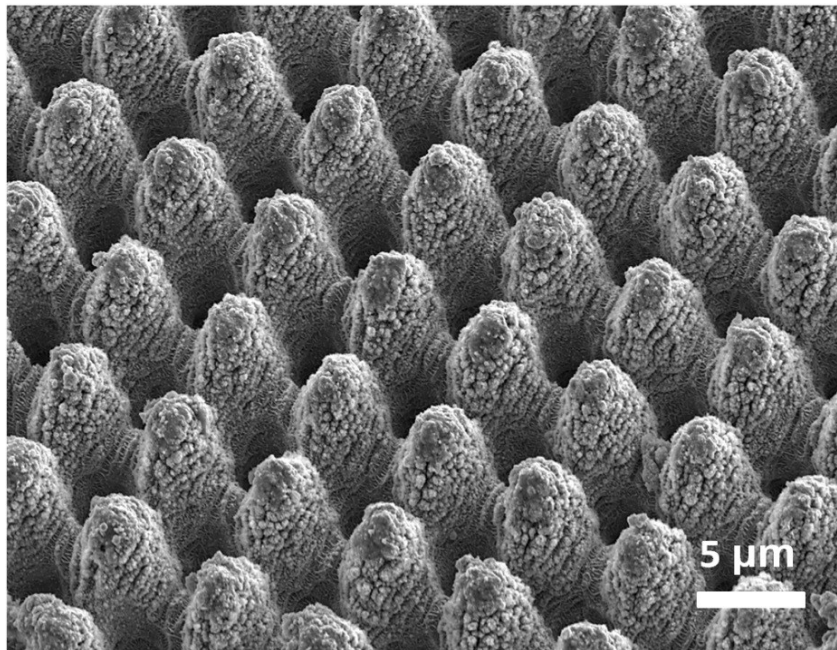
Fig. 37. Scanning electron micrograph of pillar-like structures fabricated by ps-DLIP with $\Lambda = 5.20$ μm, using a $\tau = 10$ ps, $\lambda = 1064$ nm, and OV = 99 % (tilted at angle of 45° in x and y). The $F = 1.31$ J/cm² for the second irradiation step.

Although 100 pulses were used in each irradiation step, very well defined and homogenous pillar-like patterns can be fabricated. Compared to the state of the art of produced pillar-like patterns using DLW, the fabricated structures in this work are up to 7 times smaller [35], [150], [153]. Considering the produced pillar-like structures fabricated the AR value of 2.21 is calculated. This AR value is also significantly higher than typical values reported in the literature [153]. For example, using ns-DLIP, pillar-like structures with AR between 0.1 and 0.3 have been reported, which are approximately 7 times smaller [114].

5.2.4 Control of nanostructures on hierarchical periodic microstructures

In order to control the nano features on the final topography on the pillar-like structures, a set of experiments using nanosecond laser pulses was carried out. Since in this time regime the material interaction is governed mainly by thermal mechanisms, the melting of LIPSS features can be promoted. For the fabrication of pillars-like structures the $\Lambda = 5.50$ µm was configured using ps-DLIP. The diameter of the interference area (Ø) was set to 340 µm. The patterns were fabricated using the $F = 0.74$ J/cm^2, the OV value of 99 % and $f = 1$ kHz, which results in a linear speed of 0.34 cm/s. In the x-direction, the pulses were separated by $h = 308$ µm in order to ensure a homogeneous coverage of the processed area. The same parameters were used for the second line-like pattern irradiation. The typical produced topography can be seen in Fig. 38 (a). The inset pictures in Fig. 38 (a) highlights the additional nanostructures (LIPSS), which were simultaneously produced. The orientation of the beam polarization is represented by the arrow in Fig. 38 (a).
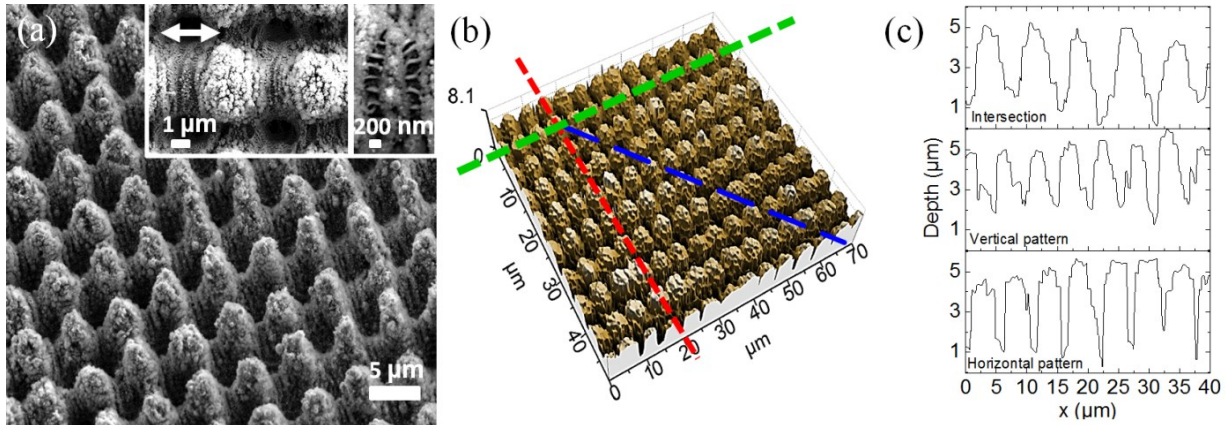
Fig. 38. (a) Scanning electron micrograph (tilted at angles of 20° in x and 10° in y), the arrow denotes the beam polarization correlated with the irradiation after rotating the substrate 90°, (b) confocal microscopy image of DLIP pillar-like structure on stainless steel with a $\Lambda = 5.50$ µm, produced with a $F = 0.74$ J/cm^2 and OV = 99 %. The lines in (b) denote the profiles from where the depth of the pillars was measured (green: horizontal, red: vertical, and blue: intersection depths), (c) profiles obtained by confocal microscopy.

In addition to the LSFL and HSFL structures, nanoparticles with a size of about 100 nm can also be observed on top of the micro-pillars, which probably result from the redeposition of the ablated material during the structuring process [93], [228]. These features are comparable in size to the nano-hair structures observed on the leaves of the Nelumbo Nucifera and Colocasia esculenta [59]. However, contrary to natural surfaces, the microstructures fabricated by ps-DLIP are highly ordered and homogenously distributed. Fig. 38 (b) illustrates the surface topography of the treated samples measured by confocal microscopy. The microstructure depth at the intersection regions of the interference maxima-maxima is 4.2 µm $\pm$ 0.6 µm (blue line) whereas the vertical (green line) and horizontal (red line) depths were determined to be about 3.0 µm $\pm$ 0.4 µm. The profiles at these positions are presented in Fig. 38 (c). After producing the multi-scale surfaces using the ps-DLIP

process, the LIPSS were melted using a nanosecond (ns) pulsed laser treatment. Additionally, the aim of the experiment was to keep the morphology of the pillars constant. In this way, the influence of the sub-micrometer structures on the SWCA can be properly highlighted. To qualitatively analyse this procedure, two-dimensional Fast Fourier Transform (FFT) was applied on the taken SEM images. The FFT analysis identifies periodic features with different length scales. In the case of the ps-DLIP treated steel sample, the SEM image is shown in Fig. 39 (a) and its Fourier transform is shown in Fig. 39 (d). As it can be seen, the FFT image of the combined DLIP + LIPSS structures is characterised by a distinct intensity distribution with features of constant distance, which originate from the symmetry of the DLIP pattern (pillar geometry). Additionally, two flanking "clouds" are attributed to the LIPSS features, and they are classified as LSFLs type-s features [140]. This multi-scale periodic surface was later irradiated with $F = 0.27$ J/cm² and $F = 0.55$ J/cm² (see experimental section), and obtained the surface pattern topographies shown in Fig. 39 (b) and Fig. 39 (c), respectively.
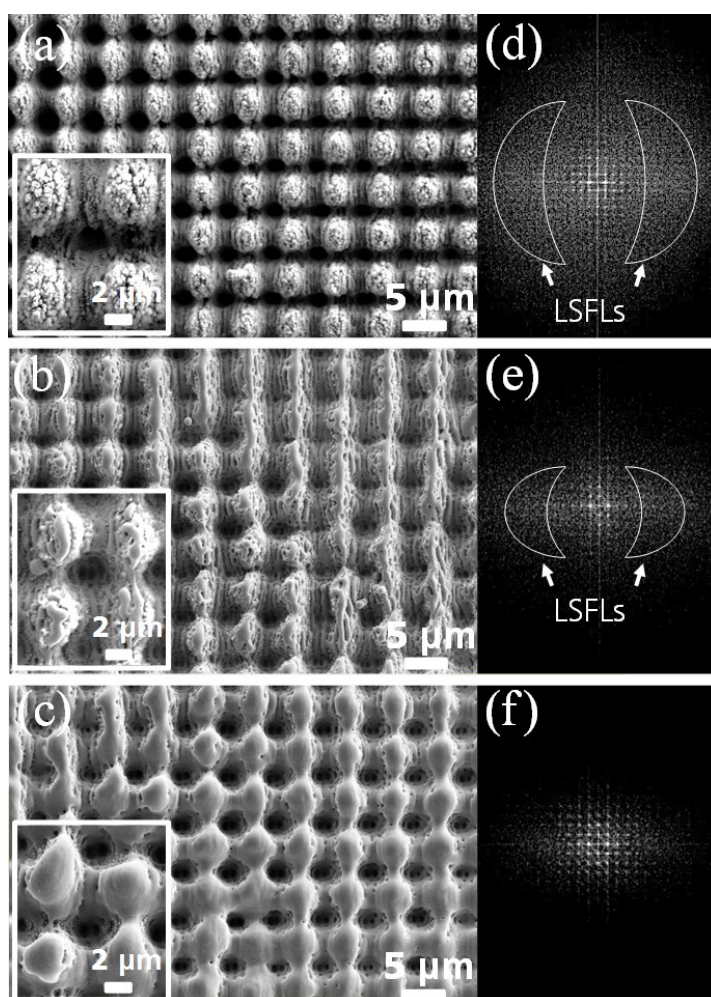

Fig. 39. (a-c) Scanning electron micrographs of stainless steel samples processed by ps-DLIP and their 2D-FFT (d-f). (a) Multi-scale pillar-like structures covered by LIPSS features and pillar-like features after using the nanosecond laser treatment for re-melting the LIPSS features at (b, e) $F = 0.27$ J/cm² and (c, f) $F = 0.55$ J/cm².

As can be seen in the images, the post-process led to the subsequent melting of the surface features (LSFL, HSFL and nanoparticles) with the increased laser fluence. In the case of the sample irradiated with lower laser fluence (Fig. 39 (b)), the nano-roughness is reduced and at the same time the LSFL became more noticeable, which means that the HSFL are initially molten. Finally, the $F = 0.55$ J/cm² leads to a nearly complete erase of the two-scale LIPSS, as shown in Fig. 39 (c). The continuous disappearance of the LIPSS with increasing laser fluence was also confirmed by the FFT results. As can be seen in Fig. 39 (e) and 39 (f), the intensity of the clouds corresponding to the LIPSS become less pronounced with increasing fluence.

Although the LIPSS could be removed from the produced pillars using the ps-DLIP treatment, it is also necessary to determine if the nanosecond pulsed laser treatment affected the structure depth of the pillars. This effect is depicted in Fig. 40, where the geometrical parameters of the pillars were characterised as a function of the F used during the nanosecond pulsed laser treatment. As can be seen, the structure depth is continuously reduced with the increase of F, from $4.24\ \mu m \pm 0.6\ \mu m$ to $3.17\ \mu m \pm 0.4\ \mu m$ for the original surface when using a $F = 0.55$ J/cm². Note that the localized heating promoted the melting of the surface at similar rates. Here it is noticeable that the depth in the intersection is always larger than the depth at the horizontal and vertical pattern, because when a double exposure approach was used, this area was irradiated twice by the interference maxima position of the DLIP pattern.
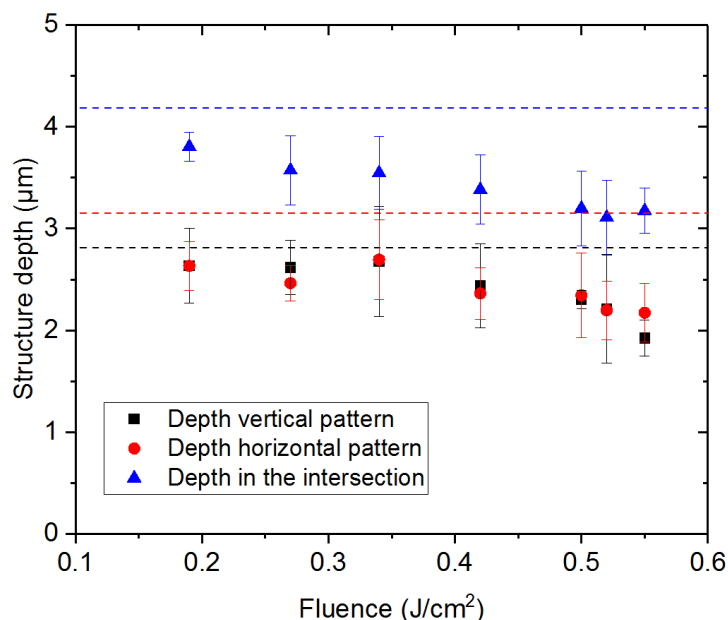
Fig. 40. Depth measurements of ps-DLIP pillar-like microstructures as a function of the laser fluence used in the post-process by nanosecond laser pulses. The dashed lines denote the mean depth of the untreated multi-scale pillar-like structures at the vertical (black line), horizontal (red line) and intersection points (blue line). Each data point was an average of ten depth measurements, the error bars were estimated by the standard deviation.

5.3 Fabrication of multi-scale periodic structures by DLW and DLIP

The micro-fabrication of multi-scale periodic structures was carried out by means of two different laser-based surface texturing techniques. The DLW technique was firstly used to produce structures in the micrometre range using nanosecond UV-laser pulses. Subsequently, micro- and nanostructures were produced by ps-DLIP using IR-laser pulses. Thus, the final topography consists in a multi-scaled periodic surface micro- and nanostructures.

5.3.1 Laser surface texturing of Ti6Al4V

In a first step-process, DLW was employed to fabricate micro-cells with a $h = 50$ μm, at $\lambda = 355$ nm, $f = 20$ kHz, $F = 5.65$ J/cm^2 and scanning speed of 80 mm/s. Fig. 41 (a) shows the micrograph of the morphology fabricated. Typical thermal effects due to the used nanosecond laser pulses can be appreciated, where the molten material was relocated in a recast formation. During the laser ablation, the molten material induces the formation of micro-walls around the untreated surface forming a closed micro-cell (see Fig. 41 (b)). In addition, also some residual granular particles were produced due to the re-solidification of the molten material.
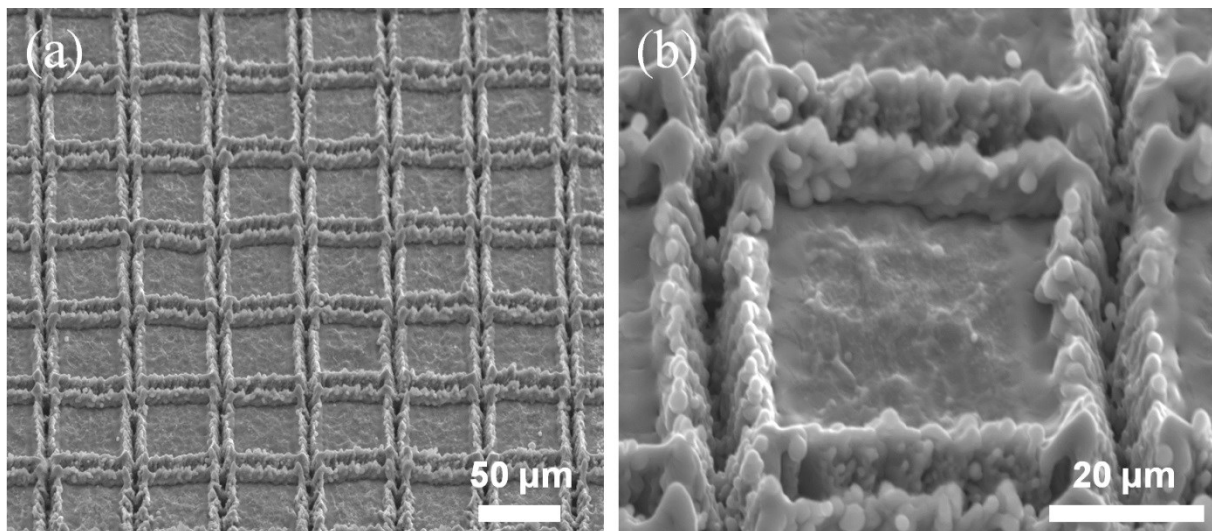
Fig. 41. Scanning electron micrographs of a Ti6Al4V surface structured by DLW using nanosecond UV-laser pulses. a) Micro-cell fabricated using the $h = 50$ μm, $\lambda = 355$ nm, $\tau = 15$ ns, $f = 20$ kHz, $F = 5.65$ J/cm^2 and scanning speed of 80 mm/s. b) The magnification image shows a surface area without laser treatment forming a closed micro-cell.

The first objective for the ps-DLIP process was to determine the laser parameters for the fabrication of pillar-like structures on Ti6Al4V. Consequently, the investigation was focused on the fabrication of line-like structures using the spatial periods of 1.10 μm, 2.60 μm and 5.20 μm. During the experiments the OV values were varied in order to identify the impact on structure depth. The OV

values ranged from 10 % up to 97 %, as fixed laser parameters the $f = 1$ kHz and $F = 0.80$ J/cm^2 were used. Thus, structure depth measurements as a function of OV are shown in Fig. 42.
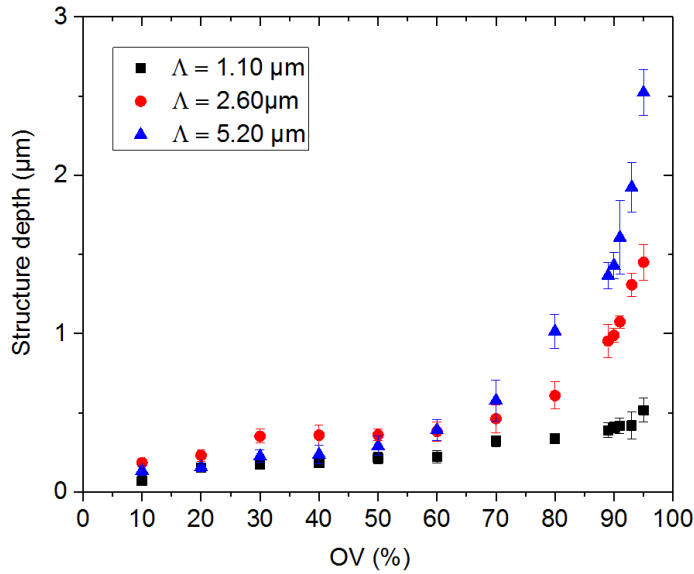
Fig. 42. Dependence of the structure depth with the OV for $\Lambda = 1.10$ µm, $\Lambda = 2.60$ µm, $\Lambda = 5.20$ µm fabricated using line-like structures by ps-DLIP on Ti6Al4V. As a constant laser parameters the $F = 0.8$ J/cm², $\tau = 10$ ps and $\lambda = 1064$ nm were used.

In can be appreciated that in the OV ranged from 80 % to 97 % the structure depth increases strongly for the $\Lambda = 5.20$ µm and $\Lambda = 2.60$ µm, achieving structure depths up to 2.56 µm and 1.42 µm, respectively. Using these results the AR values of 0.46 and 0.53 are obtained, correspondingly. For the $\Lambda = 1.10$ µm the structure depth values remains constant with values under 0.5 µm (AR = 0.45) even for the highest OV value. This effect can be attributed to the reduced distance between each interference maxima, which leads that the interference minima positions can be significantly heated and ablated.

For the fabrication of pillar-like structures the $\Lambda = 2.60$ µm was selected, in order introduce a higher number of pillars with relative high AR at the centre of the micro-cells. In this set of experiments, OV values from 89 % up to 95 % were used to fabricate pillar-like structures. It was determined to reduce the fluence value to $F = 0.55$ J/cm^2 for the second irradiation, because homogenous structures were measured at the horizontal and vertical positions. Fig. 43 (a) shows the structure depth measurements as a function of OV for pillar-like structures with the $\Lambda = 2.60$ µm, where the vertical, horizontal and the intersection positions were considered.
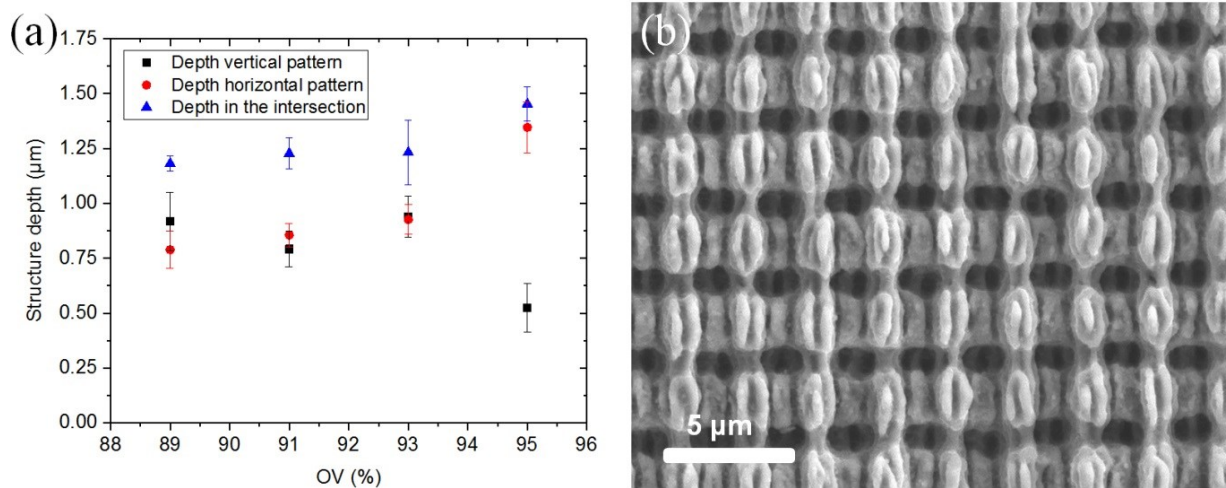
Fig. 43. a) Structure depth of ps-DLIP pillar-like microstructures as a function of the OV on Ti6Al4V using a $\Lambda = 2.60$ µm. (b) Scanning electron micrograph of pillar-like structures fabricated by DLIP with $\Lambda = 2.60$ µm, $\tau = 10$ ps, $\lambda = 1064$ nm, OV = 93 % and $F = 0.80$ J/cm^2, $F = 0.55$ J/cm^2 for the first and second irradiation, respectively.

According to the measurements in Fig. 43 (a), the OV = 93 % led to well-balanced depths in the vertical and horizontal patterns, its corresponding micrograph is presented in Fig. 43 (b). As well as in the case of structuring stainless steel using ps-DLIP, on Ti6Al4V the formation of LIPSS is also observed. Note that the LSFL are in vertical direction which corresponds to the direction of the second irradiation process.

Finally in the last set of experiments the DLW and DLIP topographies were combined. Fig. 44 (a) and (b) show the results of the fabricated multi-scaled periodic structures. The fabrication of pillar-like structures on micro-cells was carried out using the DLIP parameters of $\Lambda = 2.60$ µm, OV = 93 %, $F = 0.80$ J/cm^2 and $F = 0.55$ J/cm^2 for the first and second irradiation, respectively.
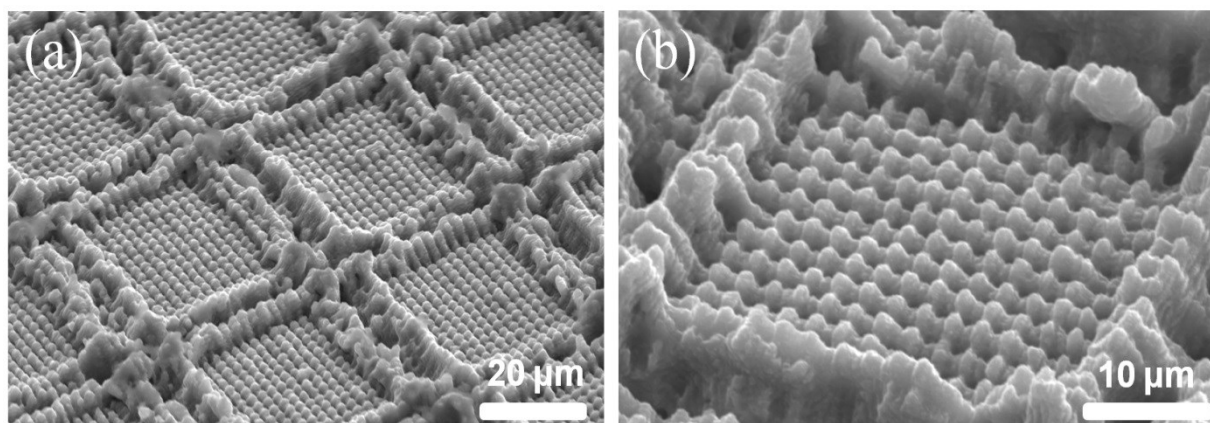
Fig. 44. a) and b) scanning electron micrographs of the multi-scaled surface microstructures fabricated on Ti6Al4V by DLW and DLIP. DLW: $\lambda = 355$ nm, $\tau = 15$ ns, $f = 20$ kHz, $F = 5.65$ J/cm^2, scanning speed = 80 mm/s, and $h = 50$ µm, DLIP: $\lambda = 1064$ nm, $\tau = 10$ ps, $f = 1$ kHz, $\Lambda = 2.60$ µm and $F = 0.80$ J/cm^2, $F = 0.55$ J/cm^2 for the first and second irradiation, respectively.

In the micrograph presented in Fig. 44 (a) is observable a well-defined pillar-like structures in the centre of the micro-cell. Additionally, LIPSS fabricated during the ps-DLIP process allowed creating a triple scale roughness surfaces. The obtained results suggest that ps-DLIP technology can be combined with ns-DLW in order to create topographies that mimic natural hydrophobic surfaces.

5.3.2   Laser surface texturing of Al2024

The micro-fabrication of multi-scale periodic structures on Al2024 was carried out by means of two different laser-based surface texturing techniques. Similar to the case of Ti6Al4V, structures in the micro-meter range using nanosecond UV-laser pulses were fabricated by DLW, afterwards pillar-like microstructures by picosecond IR-laser pulses were fabricated using DLIP.

For the first step process, micro-cells by DLW were fabricated. The fixed laser parameters include the $\lambda = 355$ nm, $f = 100$ kHz, $F = 1.28$ J/cm^2 and scan speed of 80 mm/s, while the h values were ranging from 17 μm up to 35 μm. For instance, Fig. 45 shows the micrograph of the morphology fabricated using a $h = 25$ μm. It can be observed spherical droplets that were expelled and re-solidified due to the dominant thermal ablation process. They can be observed mainly on the top of the structures, but also at the centre of the micro-cells.
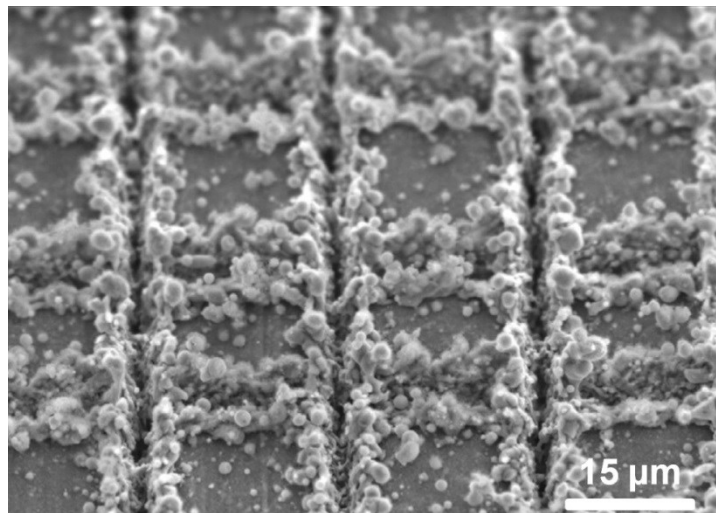
Fig. 45. Scanning electron micrographs of Al2024 surface structured by DLW using nanosecond UV-laser pulses. Micro-cell fabricated using $h = 25$ μm, $\lambda = 355$ nm, $\tau = 15$ ns, $f = 100$ kHz, $F = 1.28$ J/cm^2 and scanning speed = 80 mm/s.

For the first set of experiments using ps-DLIP, line-like structures using the $\Lambda = 2.60$ μm and $\Lambda = 5.80$ μm were fabricated. The fixed laser parameters values include the $f = 1$ kHz and $F = 0.8$ J/cm^2. As in the case of the previous metallic surfaces presented in this thesis, the experiments correlated with the variation of the structure depth as a function of the OV were carried out on Al2024. This dependence is presented in Fig. 46.
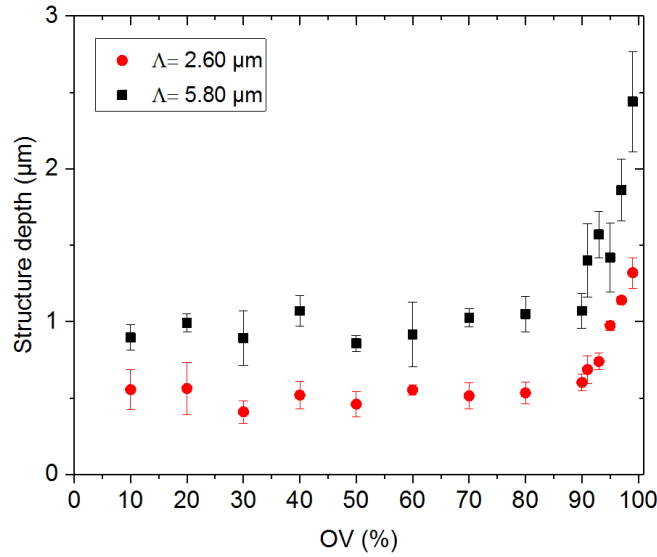
Fig. 46. Dependence of the structure depth with the OV for $\Lambda = 2.60$ μm, $\Lambda = 5.80$ μm fabricated using line-like structures by ps-DLIP on Al2024. As a constant laser parameters the $F = 1.46$ J/cm², $\tau = 10$ ps and $\lambda = 1064$ nm were used.

It can be observed in Fig. 46 that the structure depth was consistently higher for the structures with $\Lambda = 5.80$ μm than for the $\Lambda = 2.60$ μm. This effect was more noticeable on aluminium surfaces, since it has a thermal diffusion length value larger than titanium or stainless steel. Hence, it can be connected with a heat accumulation effect on the interference minima which causes a partial ablation of the material at these positions for the $\Lambda = 2.60$ μm.

In a second set of experiments, the optimal parameters for the fabrication of pillar-like structures on Al2024 were investigated. The samples were irradiated fabricating line-like structures with $F = 1.46$ J/cm² and OV values of 99 %. Subsequently, the substrates were rotated 90° in the x-y plane and re-irradiated using the same OV value, in this case the fluence was reduced to the value of $F = 1.18$ J/cm², corresponding to 81 % of the first pulse, since for higher energies the second line-like pattern erased partially the previous line-like microstructures. Fig. 47 (a) depicts the depth fabricated as a function of the OV, the measurements were performed for pillar-like structures using spatial periods of 2.60 μm (Fig. 47 (a)) and 5.80 μm (Fig. 47 (b)).
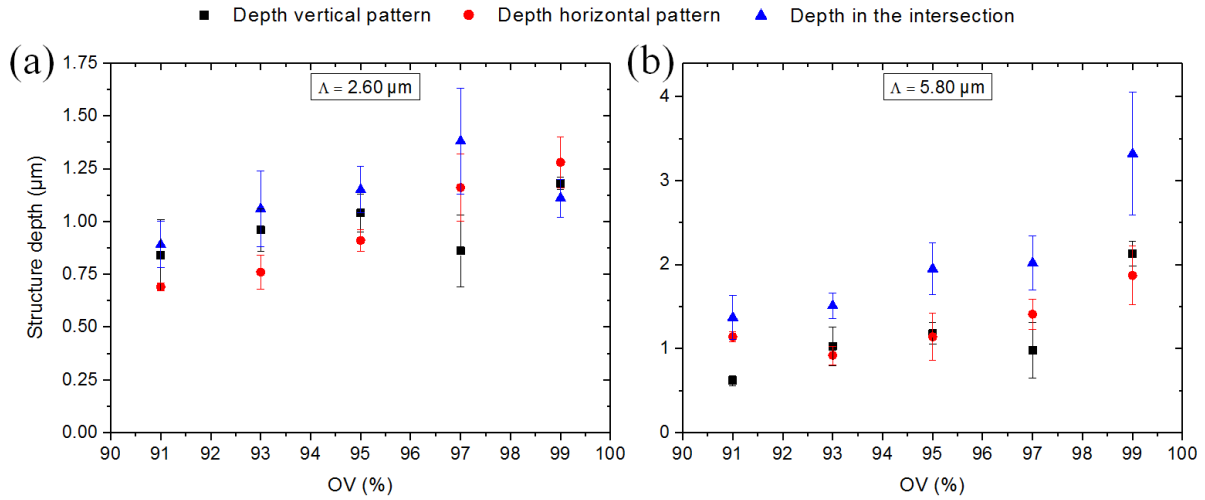
Fig. 47. Structure depth of ps-DLIP pillar-like microstructures as a function of the OV on Al2024 using the (a) Λ = 2.60 μm and (b) Λ = 5.80 μm. The fluence values were F = 1.46 J/cm^2 and F = 1.18 J/cm^2 for the first and second irradiation, respectively.

For both spatial periods the OV value of 95 % shows balanced structure depths for the vertical and horizontal positions, as it was expected the intersection depths are larger, considering this positions the AR of 0.46 and 0.34 are calculated for Λ = 2.60 μm and Λ = 5.80 μm, respectively. Due to the hatch distance values used during the DLW process and in order to fabricate a higher number of microstructures in the centre region of the micro-cells with higher AR, the Λ = 2.60 μm, at OV = 95 % was selected for the successive experiments.

In the fabrication of multi-scale periodic structures, micro-cells produced by DLW with h values of 17 μm and 35 μm were used. However, for the ps-DLIP process, the previously used fluence values of F = 1.46 J/cm^2 and F = 1.18 J/cm^2 for the first and second line-like process, respectively, could not be applied in this procedure, since these fluence values were too high and the DLIP microstructures erased the microcells. This effect is argued due to absorption change on the surface, the first micro-cell structures increased the absorptivity on the material which enlarged the ablated material induced by ps-DLIP. Thus, a new set of experiments related with the fabrication of line-like patterns on the micro-cell structures was performed. Using the OV = 95 % as a constant and decreasing the fluence values systematically was observed that the DLIP microstructures were fabricated at F = 0.44 J/cm^2 without erasing the micro-cells. The used fluence corresponds to 30 % of the fluence value used previously on the untreated samples. Thus, in order to fabricate pillar-like structures, the fluence value for the second pulse was reduced. It was calculated with the estimated rate of 20 % less than the first DLIP irradiation and fixed to F = 0.36 J/cm^2. The estimation is based on the previous results when the optimal pillar-like structures were determined. Fig. 48 shows the micrographs of the fabricated multi-scale periodic microstructures on Al2024 surfaces. Two different micro-cells with h values of 17 μm and 35 μm fabricated by DLW, they are shown in Fig. 48 (a) and Fig. 48 (b), respectively, while the ps-DLIP pillar-like microstructures correspond to the Λ = 2.60 μm in both cases.
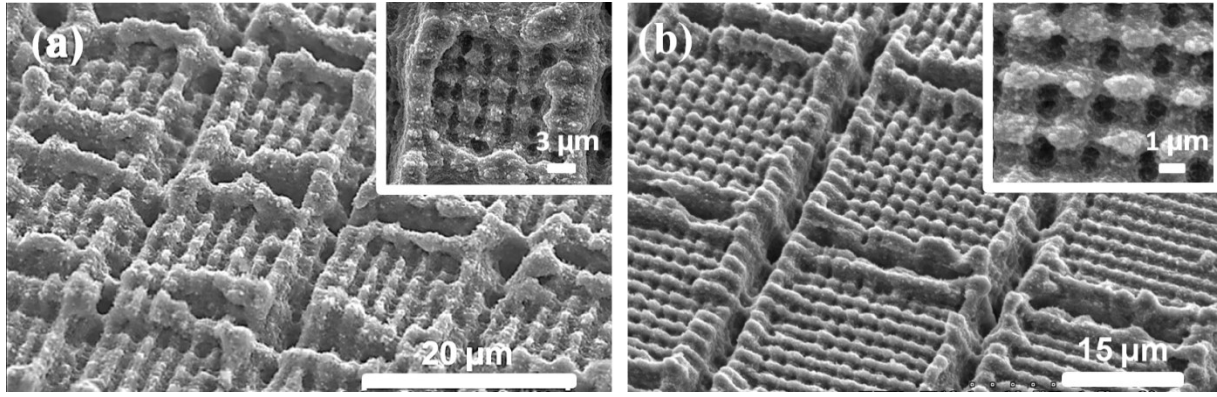
Fig. 48. Scanning electron micrographs of Al2024 samples patterned with multi-scaled periodic structures by DLW and DLIP techniques, for the micro-cell were used (a) $h = 17$ μm and (b) $h = 35$ μm (DLW: $\lambda = 355$ nm, $\tau = 15$ ns, $f = 100$ kHz, $F = 1.28$ J/cm^2, scanning speed = 80 mm/s, and for the DLIP pillar-like were used $\Lambda = 2.60$ μm, $\lambda = 1064$ nm, $\tau = 10$ ps, $f = 1$ kHz, and $F = 0.44$ J/cm^2, $F = 0.36$ J/cm^2 for the first and second irradiation, respectively, (tilted at angle of 45° in x and y). Inset picture in (a) (b) show the top view at the centre of the micro-cells.

As it can be observed, in the inset picture in Fig. 48 (a) the pillar-like structures were fabricated successfully in the centre of the micro-cells. Moreover, the spherical droplets produced by ns-DLW were removed after the ps-DLIP. However, contrary to the pillar-like structures fabricated on titanium and stainless steel, the hierarchical microstructures on aluminium do not contain LIPSS (see inset picture of Fig. 48 (b)). This result can be connected with the relative large thermal diffusion length, in the case of 10 ps pulses in pure aluminium has a value of $l_T = 30.8$ nm, (in titanium and stainless steel the values are $l_T = 5.3$ nm and $l_T = 8.4$ nm, respectively). It can impact the fabrication of LIPSS when using spatial period $\Lambda = 2.60$ μm together with the relative low fluence and OV of 95 %. However, using ps-DLIP with $\Lambda = 7$ μm, a higher $F = 1.93$ J/cm^2 and OV = 99 %, LIPSS with spatial periods of 570 nm were already reported on Al2024 [229].

5.4   Structuring of a large aircraft surface for a flight test

The pillar-like microstructures were also fabricated on Ti6Al4V following the methodology used on stainless steel samples. For a flight test, pillar-like structures were chosen with a $\Lambda = 5.20$ μm since using ps-DLIP, hierarchical micro- nanostructures can be attained and potentially enhance wettability properties. Examples of produced pillar-like structures on Ti6Al4V are shown in Fig. 49 (a), the aircraft surface was structured using the fixed laser parameters $F = 0.57$ J/cm^2, OV = 99 %, $h = 346.5$ μm, $\lambda = 1064$ nm, $f = 1$ kHz and $\tau = 10$ ps.
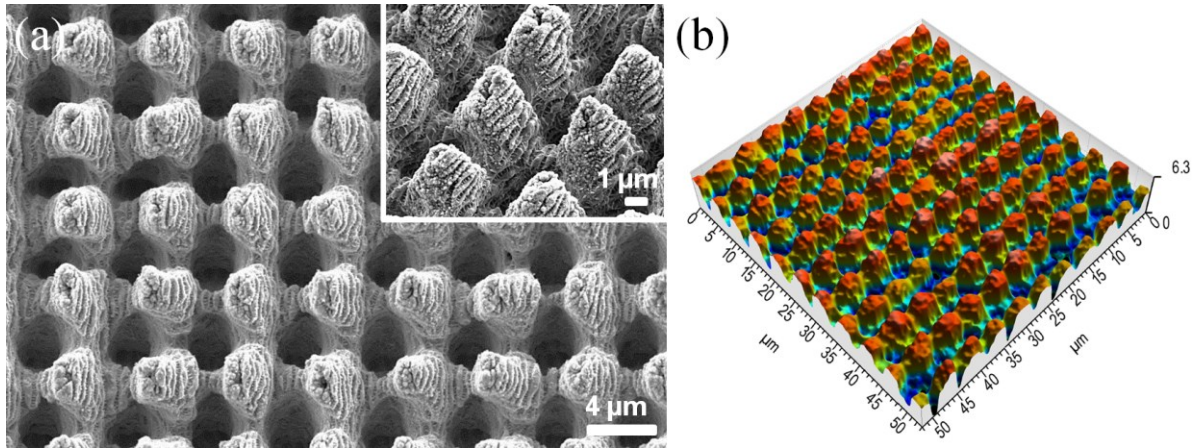
Fig. 49. (a) Scanning electron micrograph and (b) confocal microscopy image of pillar-like structures fabricated onTi6Al4V by ps-DLIP with Λ = 5.20 µm, using a τ =10 ps, λ = 1064 nm and OV = 99 %. The F = 0.57 J/cm² for both irradiation steps.

Fig. 49 (a) shows the micrograph image of the pillar-like surface. It denotes clearly the difference on the microstructure depths, it is observable larger on the maxima-maxima positions (also called intersection depth) with values about 3.6 µm $\pm$ 0.33 µm, while in the horizontal and vertical depths it achieved values of 2.8 µm $\pm$ 0.48 µm. Furthermore, in the inset picture in Fig. 49 (a) can be observed that the pillars are cover with LIPSS, it results in a hierarchical micro and nano structures as in the case of stainless steel. Fig. 49 (b) shows a typical confocal image obtained during the characterisation of the microstructures.

In Fig. 50 (a) using a lower amplification can be observed a SEM image of the pillar-like structures (tilted at angle of 45° in x and y). It shows the high uniform structured surface obtained by ps-DLIP. In Fig. 50 (b) is depicted the final sample, the darker area corresponds to the surface structured. Commonly, after using high OV values and ps-DLIP, dark treated surfaces were obtained. In collaboration with Airbus Group the ps-DLIP structured Ti6Al4V surface of 380 cm^2 (total area sample of 480 cm^2) was assembled on the wing of an airplane. The approach of the test was focused on the durability against rain and erosion.
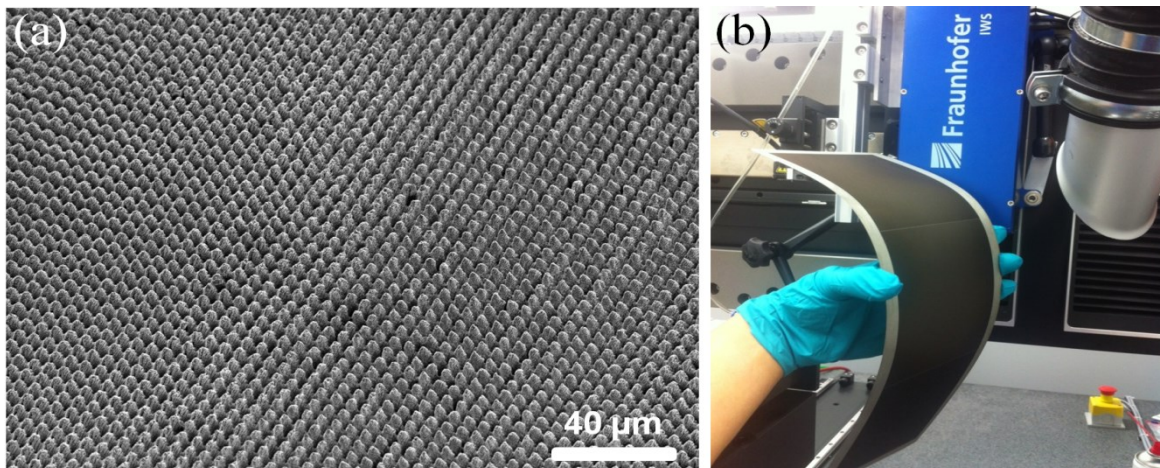
Fig. 50. (a) Scanning electron micrograph (tilted at angle of 45° in x and y) and (b) macroscopic image of Ti6Al4V structured by ps-DLIP with pillar-like structures using the Λ = 5.20 µm (size 10 x 38 cm).

6.   Development of an analytical ablation model for ps-DLIP

An analytical laser ablation model which describes the fabricated structure depth as a function of the ps-DLIP process parameters is introduced in this chapter. In a first overview, it is important to consider the pulse distribution which was introduced in chapter 4.3. Thus, the number of pulses in the *y* axes is an important factor that impacts the achievable structure depth. The graphical representation of the model is depicted in Fig. 51.
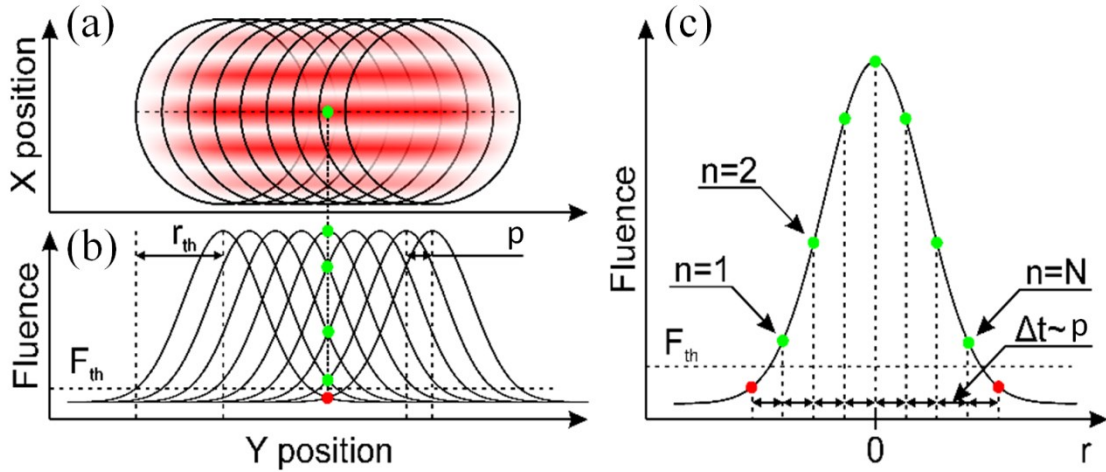
Fig. 51. Graphical representation of the analytical ablation model used to calculate the structure depth produced by ps-DLIP line-like pattern. (a) DLIP-pixel positions during the pulse distribution process. (b) Schematic representation of the fluence distribution of each DLIP-pixel along the centre of the distribution path. (c) Schematic representation of the single laser spot fluence across the point of interest and along the interfering lines.

Fig. 51 (a) represents the positions of the DLIP-pixel during the pulse distribution process. Moreover, a schematic representation of the fluence distribution of each DLIP-pixel along the centre of the distribution path is represented in Fig. 51 (b). Each DLIP-pixel ablates a periodic structure across a circular area; it results in a radius of the structured area (r_{th}). The pulse-to-pulse distance (p) is also denoted. The green dots represents the point where the structure depth is calculated using the analytical model (point of interest). In Fig. 51 (c) a single laser spot with a Gaussian distribution is represented. The dots represent the laser fluence at which the point of interest was ablated by each forthcoming pulse, green and red dots denote fluences higher and lower than the ablation threshold (F_{th}), respectively.

Assuming that the laser has a Gaussian beam profile, the value of r_{th} can be calculated using Eq. 24 [204]:

$$r_{th} = \omega \sqrt{\frac{1}{2} \ln\left(\frac{F_0}{F_{th}}\right)}, \tag{24}$$

where ω is the radius of the laser interference area and F_0 is the laser peak fluence of the Gaussian beam.

In order to determine the depth fabricated at the centre point in the Gaussian beam distribution (point of interest – green dots in Fig. 51 (a)) the cumulative absorbed fluence must be considered. In this context, an area can be exposed to multiple pulses, if the forthcoming spots are overlapped; in consequence, higher ablated material and larger depths will be produced. Therefore, the final structure depth should be calculated by the accumulation of ablated depths in the DLIP-pixel within the r_{th} parameter. However, it must be noted that each pulse ablates the point of interest with different local F values, due to the Gaussian energy distribution. Thus, the Eq. 25 is introduced in order to calculate the value of fluence as a function of the position ($F(n)$) [230]:

$$F(n) = F_0 \exp\left(-2\frac{r(n)^2}{\omega^2}\right), \tag{25}$$

where $r(n)$ is the distance from the point of interest to the centre of the pulse, which is expressed in terms of pulse number (m) and the total number of laser pulses (N) within the r_{th} value (see Fig. 50 (b)) as is presented in Eq. 26:

$$r(n) = p\left(-\frac{N-1}{2} + m - 1\right) = \frac{p}{2}(2m - N - 1), \tag{26}$$

where p is the pulse-to-pulse distance. Thus, in order to calculate the value of N, the Eq. 27 is introduced:

$$N = 2 \cdot floor\left(\frac{r_{th}}{p}\right) + 1 = 2 \cdot floor\left(\frac{\sqrt{\frac{1}{2}\ln\left(\frac{F_0}{F_{th}}\right)}}{2\left(1-\frac{OV}{100\%}\right)}\right) + 1 \tag{27}$$

where the *floor* function (also known as the greatest integer function) rounds a number down to the nearest integer or equal to a number. The mean structure depth (D) is calculated by means of Eq. 28, which considers the depth produced by individual F values at the point of interest.

$$D = \delta \sum_{n=1}^{N} \ln\left(\frac{F(n)}{F_{th}}\right), \tag{28}$$

where δ is the optical penetration depth. Finally, by substituting the Eq. 25-27 into Eq. 28, D can be estimated for determined number of pulses. Simplifying the expression D is given by Eq. 29:

$$D = \delta \cdot N\left(\ln\left(\frac{F_0}{F_{th}}\right) - \frac{2}{3}\left(1 - \frac{OV}{100}\right)^2 (N^2 - 1)\right), \tag{29}$$

where F_0 for two-beam interference can be expressed by the average laser power (P), repetition rate (f) and ω as follows:

$$F_0 = \frac{2 \cdot 2 \cdot P}{f \cdot \pi \cdot \omega^2} \tag{30}$$

As can be seen in Eq. 30, an additional multiplication factor of 2 was added, due to the two-beam interference pattern [231]. It must be highlighted that the ablation threshold used in these calculations does not depend on the pulse number, which means that the incubation effect is neglected

and F_{th} represents the effective ablation threshold for the number of pulses applied on the sample surface [232].

In order to verify the proposed ablation model, periodic line-like structures were fabricated on 304 stainless steel using two-beam DLIP configuration and $\Lambda = 5.50$ µm. During the ps-DLIP process a $f = 1$ kHz was used, it resulted in pulse energy (P_E) of 0.44 mJ on the sample surface. The value of F was varied as a function of the diameter of the laser interference area ($\varnothing$) within the range of 160 µm up to 285 µm, it resulted in F values ranging from 1.45 J/cm² down to 0.56 J/cm², respectively. The structures were produced varying the OV values from 90 % up to 99 %.

SEM images of the microstructures fabricated with a $\varnothing = 285$ µm (0.56 J/cm²) and OV values of 95 %, 97 % and 99 % are shown in Fig. 52 (a), (b) and (c), respectively. As can be appreciated, the structures contain of periodic distributed lines which become more pronounced if the OV value is increased. As aforementioned (in chapter 5.2.2) the DLIP microstructures are covered with LSFL and HSFL with spatial periods about 700 nm and 200 nm, respectively.
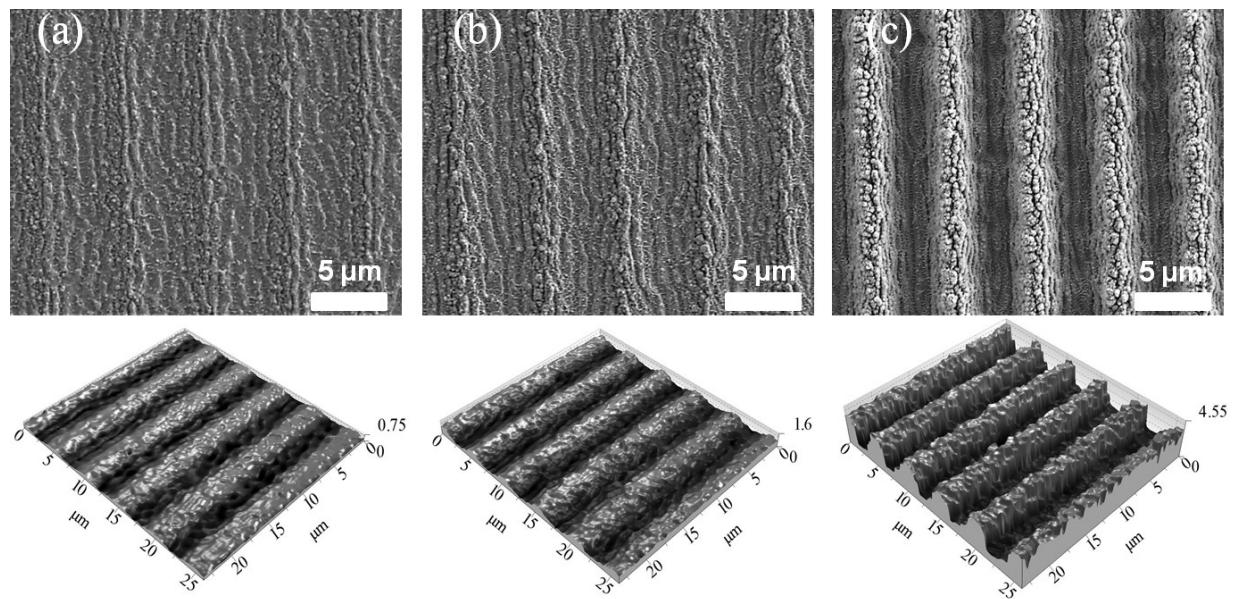
Fig. 52. (top row) Scanning electron micrographs and (bottom row) confocal images of the line-like structures fabricated by ps-DLIP on stainless steel with OV values of (a) 95 %, (b) 97 % and (c) 99%, as fixed laser parameters the $\varnothing = 285$ µm (0.56 J/cm²), $\Lambda = 5.50$ µm and $f = 1$ kHz were used.

Subsequently, the mean structure depth (D) produced by DLIP was measured using confocal microscopy. D values were measured at the centre of the structured line-like structures and averaged in the contained area of 25 x 25 µm, which is partially the view field of the 150X objective. In Fig. 53 is plotted the D as a function of the OV and $\varnothing$, where each measurement is represented by the black dots with drop lines.
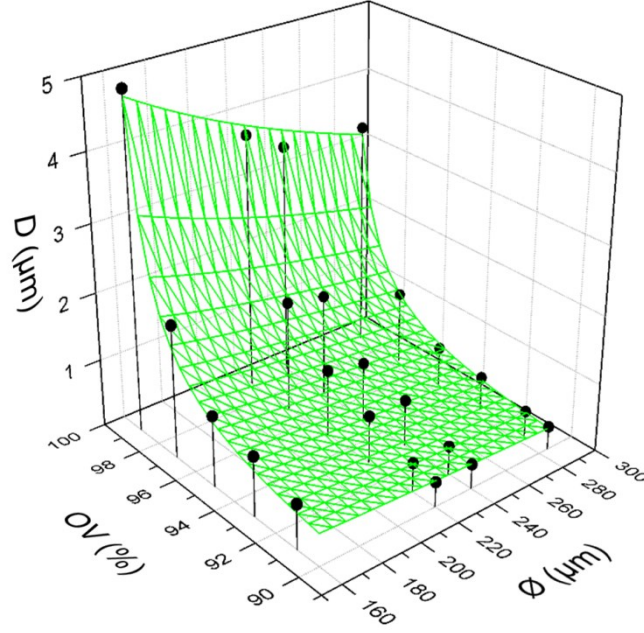
Fig. 53. Mean structure depth (*D*) produced by DLIP represented as a function of OV and diameter of the laser interference area (Ø). Black dots with drop lines represent the measurements of the experimental results. The green surface corresponds to the structure depths calculated using the analytical model.

Furthermore, the obtained results by the introduced analytical ablation model are plotted as a green surface in Fig. 53. The reported ablation threshold on the 304 stainless steel is 0.05 J/cm^2 for a single pulse with a pulse duration of 10 ps [233], a $\delta = 8.9$ nm at the wavelength of 1064 nm [230] and the $P_E = 0.44$ mJ were used during the calculation. The average error of the calculated depth is ~ 10 %, which shows that the model is in agreement with the experimental data points.

This model can also be used to determine the set of parameter (OV and Ø) to fabricate a defined *D*. For this reason the Eq. 29 was numerically solved in order to find the OV as a function of Ø for a determined structure depth. The resulting isocurves plotted in Fig. 54 (a) correspond to a combination of OV and Ø values, which results in the same *D* values. It means that there are different arrangements of OV and Ø, which can be used to fabricate a define value of *D*. Therefore, it is important to determine which set of parameter is optimal in terms of throughput. For this reason, the throughput (area per unit of time) is calculated using the Eq. 31:

$$\frac{\partial A}{\partial t} = 2r_{th}v = 2r_{th}d \cdot f = \frac{16P}{F_0\pi}\left(1 - \frac{OV}{100\%}\right)\sqrt{\frac{1}{2}\ln\left(\frac{F_0}{F_{th}}\right)} \tag{31}$$

where *v* is the speed and can be expressed by $v = d \cdot f$. Thus, the approximation of throughput as a function of Ø is shown in Fig. 54 (b).
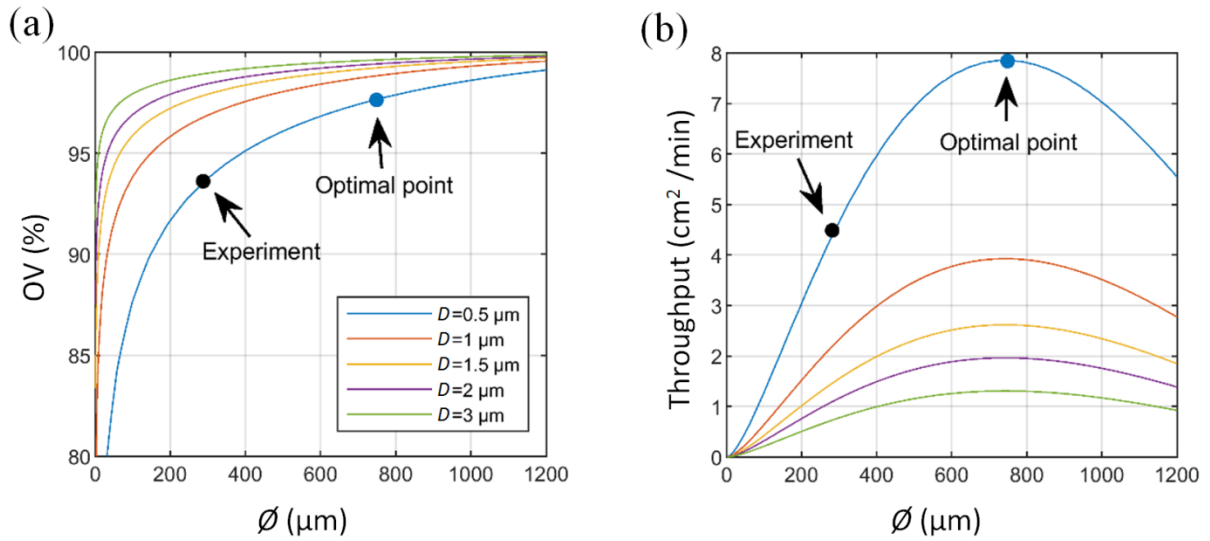
Fig. 54. (a) Calculated isocurves representing the set of process parameters OV and Ø, which results in a determined D. (b) The calculated throughput for each isocurve in (a).

All curves in Fig. 54 (b) show that the maximal throughput is reached at the value of $Ø = 740$ µm. This value is larger than the $Ø$ used in the previous experiments. It means that the process parameters used in the set of experiments were not optimal in terms of throughput. For example, for a value of $D = 500$ nm which is fabricated using the $Ø = 285$ µm and OV $= 93$ %, results in 4.7 cm²/min at 1 kHz repetition rate (black dots in Fig. 54 (a) and (b)). On the other hand, according to the model, the optimal parameters of $Ø = 740$ µm and OV $= 97.6$ % will result in the increase of the throughput to 7.9 cm²/min, which is 1.7 times faster (see blue dots in Fig. 54 (a) and (b)).

In a last set of experiments, the values of $Ø = 600$ µm and $Ø = 740$ µm where selected to be compared with the model and consequently to reach the maximum throughput of the system. In Fig. 55 is shown the confocal microscope images of the line-like structures fabricated using the $Ø = 600$ µm and $Ø = 740$ µm, with OV= 96.2% and OV $= 97.6$ % respectively, the OV values were calculated by the model in order to achieve 500 nm in depth. In both cases D was achieved within the measured area.
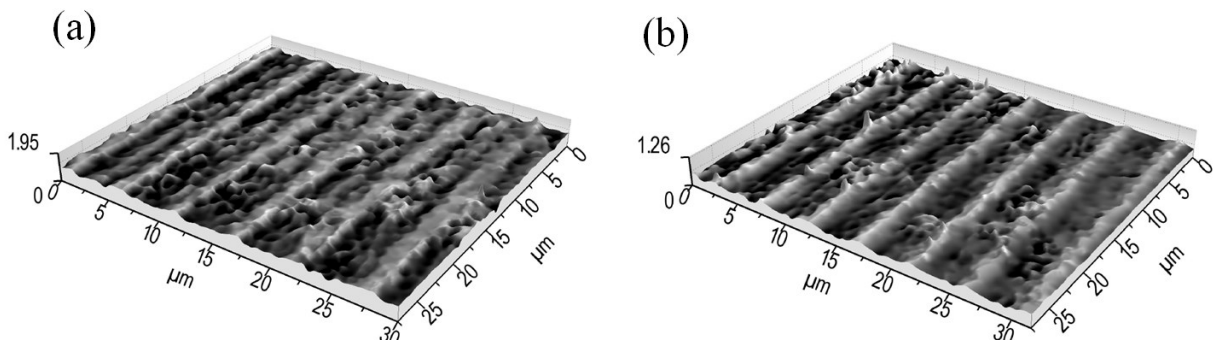
Fig. 55. Confocal images of line-like structures fabricated by ps-DLIP on stainless steel using (a) $Ø = 600$ µm, OV= 96.2% and (b) $Ø = 740$ µm, OV $= 97.6$ %, as fixed laser parameters $\Lambda = 5.50$ µm and $f = 1$ kHz were used.

Finally, in Fig. 56 the modelled maximal throughput (blue line) is plotted together with the experimental results (black circles) as a function of D for values ranging from 0 up to 5 µm. The corresponding D values for the experiments using the $\varnothing = 740$ µm were measured and included in the graph (red circles), OV values ranged from 99.0 % up to 99.5 %, an increment step of 0.1 % was used. Specifically, the OV values used for the experiments corresponding to the red circles and blue line are represented in the right axis.
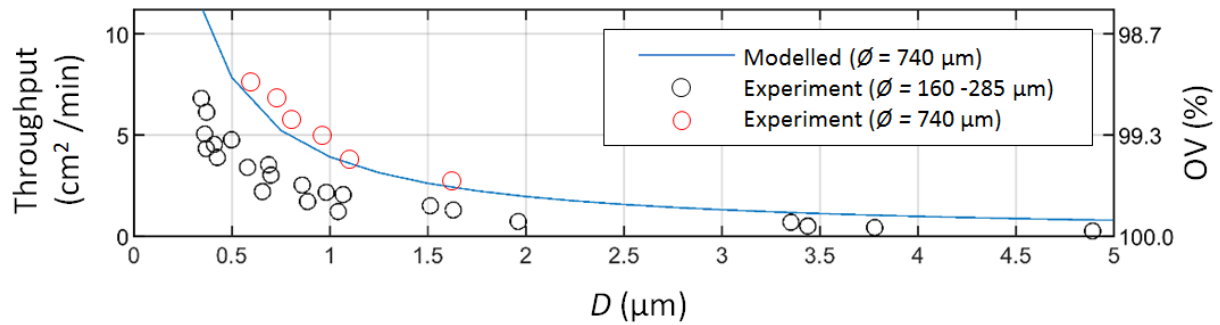
Fig. 56. Maximal modelled (blue line) and experimental (circles) throughputs for defined D value. All plots were calculated for a P_E of 0.44 mJ, $\Lambda = 5.50$ µm and $f = 1$ kHz.

Achievable throughputs to produce pillar-like structures on stainless steel (topographies presented in chapter 5.2.3 using the $\Lambda = 5.20$ µm, $f = 1$ kHz and $\varnothing = 160$ µm) range from 0.71 cm²/min to 0.076 cm²/min for OV values of 91 % and 99 % respectively. Consequently, even for the largest used OV (99 %) the processing time was at least two to three times shorter compared to the state of the art. For instance, using DLW (e.g. 0.037 cm²/min for 19 µm spatial period pillars with 20 µm of structure depth) [234]. Furthermore, since the spatial periods are up to 7 times smaller than typical structures, the density of produced features was increased up to 49 times for the pillar-like patterns (7 x 7). Furthermore, it has also important to mention that the laser power used was 0.44 W. Considering that the available laser power and repetition rates of typical commercial picosecond laser systems are considerable higher, significantly shorter processing times are possible.

7. Surface properties of textured materials

7.1 Determination of wetting behaviour

In order to determine a relation between the hierarchical micro-pillar fabricated by ps-DLIP on stainless steel 1.4016 (presented in chapter 5.2.3) and its wettability response, SWCA measurements were carried out. The SWCA on the non-treated surface showed an average value of 67.6 °. One hour after the laser treatment, the contact angle was immediately measured observing a strongly hydrophilic behaviour (SWCA < 10 °). This effect has been explained by Kietzig [178], who proposed the formation of an active magnetite $Fe_3O_{4-\delta}$ layer after the laser process which is strongly hydrophilic.

After 30 days of storing the laser treated samples at normal ambient conditions, the SWCA was measured again, observing a significant increase, it is shown in Fig. 57 (a). As it can be observed, the measured SWCAs are plotted as function of the Filling Factor (FF) for both Λ = 2.60 µm and Λ = 5.20 µm spatial periods (only pillar-like structures treated with OV values over 91 % were considered). The FF depicts the ratio between pillar width (described by the Full Width at Half Maximum) (FWHM) and spatial period, in which FF = 1 corresponds to the smooth surface. The increase of the SWCA can be explained by the dissociative adsorption of CO_2 into carbon which is catalysed by the magnetite $Fe_3O_{4-\delta}$ layer when the laser treated surfaces are exposed to air. Thus, a non-polar carbon layer is formed which promotes the hydrophobic behaviour. These results also show that in general, an increase in the SWCA with a decreasing FF can be observed for both periods. However, pillar-like structures with similar FF's but with different spatial periods show significant differences. For example, SWCA of the samples treated with the Λ = 5.20 µm are over ~140 ° for FF ~ 0.35, while for the Λ = 2.60 µm patterns a SWCA maximal up to ~ 125 ° could be reached for the same FFs. A possible explanation for this behaviour could be attributed to the shape of the produced pillars for both periods. For the case of microstructures with Λ = 5.20 µm, the produced pillars represent a more needle-like topography, while the pillars with Λ = 2.60 µm are more irregular and thus the contact area with the water droplets increases.
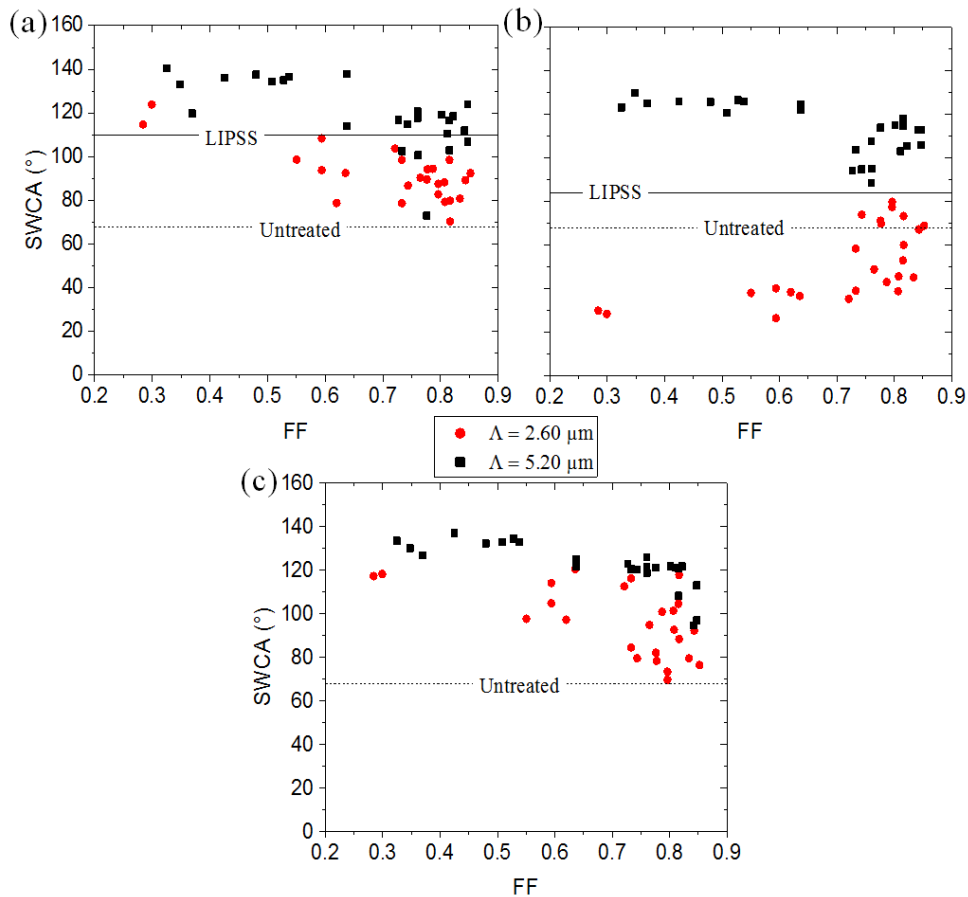
Fig. 57. Relations between the filling factor and water contact angles of stainless steel surfaces irradiated by ps-DLIP with the pillar-like patterns, using $\Lambda = 2.60$ µm and $\Lambda = 5.20$ µm measured (a) 30 days after DLIP process, (b) after immerse the samples in ethanol in ultrasonic bath during 1 hour and (c) 130 days after ultrasonic bath. The SWCA of samples containing LIPSS are also shown (continuous line).

In order to determine the effect of the hierarchical surface topography on the SWCA, also LIPSS-structures were produced on metallic stainless steel samples (without interference). In this case, the substrates were treated with OV = 97 % and $F = 1.45$ J/cm². In this case, a SWCA of 110 ° was measured (see the continuous line in Fig. 57 (a) which is similar to the reported values of the DLIP produced pillar-like patterns with $\Lambda = 5.20$ µm with high FF. In consequence, it can be assumed that contact angles over 120-130 ° required both, the DLIP and LIPSS structures which confirms the benefits of the multiple-scaled topography.

It has been proposed that depending on the washing procedure the contact angles can be altered due to the surface polarization which impacts the wettability in some degree [235], [236]. In this context the ps-DLIP pillar-like surfaces were cleaned in ultrasonic bath (using ethanol during 1 hour) and 24 hours later, the SWCA measurements were performed again under the conditions described before. This experiment was carried out in order to evidence that surface chemistry on laser surface areas can be altered. Furthermore, this scenario shows that topography is not the only responsible of a hydrophobic behaviour. The obtained results are depicted in Fig. 57 (b). As can be

seen, for the $\Lambda = 2.60\ \mu m$ ps-DLIP structures, the SWCA strongly decreased while the pillar-like patterns with $\Lambda = 5.20\ \mu m$ shown a similar behaviour as the non-cleaned surfaces. The same behaviour was observed for the stainless steel sample with the LIPSS structure, where the SWCA decreased from 110 ° to 84°.

These results suggest that after the ultrasonic bath, a complete or partial removal of the non-polar carbon layer occurs which is responsible of the decrease in the SWCA for the $\Lambda = 2.60\ \mu m$ as well as the LIPSS samples. Differently, due to the high AR of the produced pillars on the samples treated with the $\Lambda = 5.20\ \mu m$, the hydrophobic character is kept which means that in this case the surface topography mainly controls the surface wettability. Finally, to confirm this theory, the samples were stored again for 130 days and after that, SWCA measurements were performed. The results depicted in Fig. 57 (c) show a very similar behaviour as the samples characterised 30 days after the laser process (Fig. 57 (a)), which means that the non-polar carbon layer was regenerated and thus the hydrophobic state is recovered for all treated samples.

7.1.1 Wetting transition on single and hierarchical microstructures

In order to broaden our understanding of the wetting transition as a function of time on the micro-pillars fabricated by ps-DLIP, their wettability performance was investigated. Moreover, the single scale-micro structure treated with nanosecond laser treatment was also included in the evaluation. Fig. 58 (a) shows the hierarchical pillar-like structures (ps-DLIP) and Fig. 58 (b) the single–scale geometry. The single-scale structures were obtained by applying nanosecond laser pulses using the $F = 0.55\ J/cm^2$.
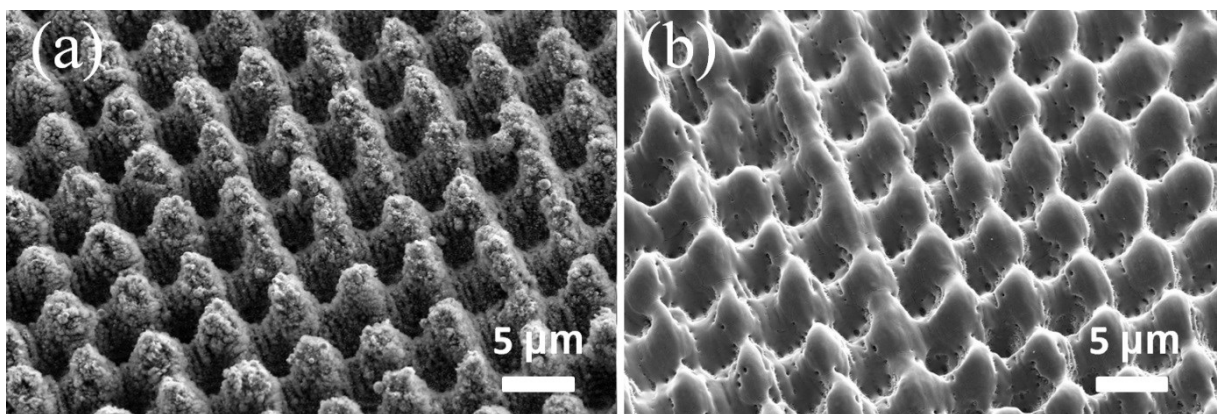
Fig. 58. Scanning electron micrographs of the DLIP pillar-like structures produced on stainless steel by (a) ps-DLIP with spatial period $\Lambda = 5.50\ \mu m$, $F = 0.74\ J/cm^2$ and OV = 99 % and (b) after the ns laser treatment using a $F = 0.55\ J/cm^2$.

The long-term SWCA measurements are presented in Fig. 59. As can be seen, three days after the laser irradiation, the SWCA on the hierarchical structured (ps-DLIP) surface was close to zero ($3° \pm 1°$), while the SWCA on the single-scale pattern (ps-DLIP + ns) was $34° \pm 5$.
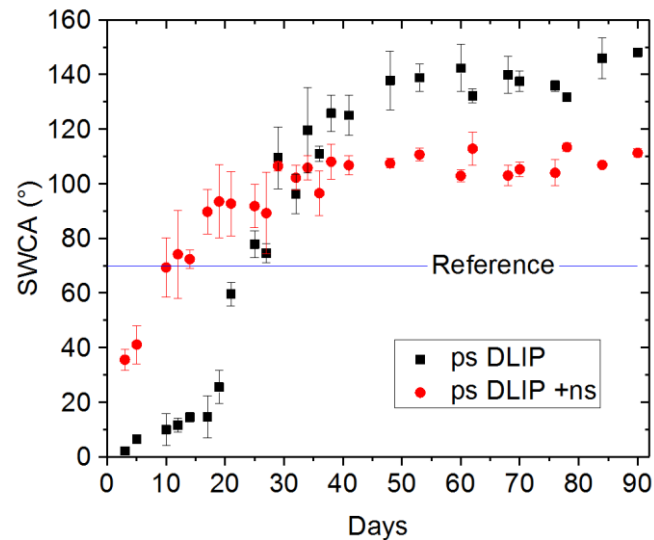
Fig. 59. SWCA measurements carried out over time on hierarchical pillar-like (ps-DLIP) and single-scale structures (ps-DLIP + ns). The Λ = 5.50 μm was used. For the ps-DLIP treatment, the F = 0.74 J/cm^2 and an OV = 99 % were used. The single-scale pattern was obtained by applying nanosecond laser pulses with F = 0.55 J/cm². Each data point was an average of four SWCA measurements, the error bars were estimated by their standard deviation. After each measurement, the samples were stored under normal ambient-pressure conditions.

The evolution of the SWCA over time shows two different responses, depending on the degree of complexity of the microstructures. In fact, for the hierarchical structures (ps-DLIP), the SWCA increased up to $138° \pm 10°$ after 50 days, while for the single-scale structures (ps-DLIP + ns) values of $107° \pm 2$ were reached after the same period of time. Note also that a steady-state condition was achieved after 30 days for single-scale structures (ps-DLIP + ns), in comparison to 50 days required for the hierarchical structures (ps-DLIP). Afterwards, the samples were stored under ambient conditions and the SWCA was measured each 30 days (until 180 days) and any significant change in the wettability response was seen. Due to the variation in less than $20°$ in the SWCA measurements on each sample, it was determined that the surfaces achieved a steady-state hydrophobic condition. Note that the steady-state condition was achieved after 30 days for single-scale structures (ps-DLIP + ns), in comparison to 50 days required for the hierarchical structures (ps-DLIP). This result suggests that the nano-roughness (LIPSS features and nanoparticles) is responsible for an increase of $31°$ (from $107°$ to $138°$) when the steady-state condition is reached. Although a high SWCA was reached, it is important to mention that the produced surfaces present a high CAH, $30°$ and $45°$ for the ps-DLIP and ps-DLIP + ns, respectively, which means that the water droplets can roll only after high sample inclination of the sample.

These observations are in agreement with a Wenzel model, for which (in a hydrophobic steady-state) an increase in the roughness induces higher contact angles, where complete wetting between the liquid and the microstructures exist. However, specifically for the hierarchical structures (ps-DLIP) values of SWCA higher than 150 ° and CAH higher than 30 ° were measured during the steady-state. These observations are connected to the rose petal effect, whereby high water droplet adhesion was promoted, and this suggested that a complete water impregnation occurred in the pillar-like microstructures while the air-trapping is maintained in the nanostructures. Less effective air trapping is associated to the single-scale structures (ps-DLIP + ns) with a CAH increase of up to 45 °.

The observed wettability transition has been also reported by other authors on different metallic surfaces [102], [105], [173], [187], [237]. It has been attributed to chemical changes at the surface. For that reason, in the following sub-chapter the chemical analyses presented are discussed.

7.1.2   Surface chemistry influence on wetting

In order to get better understanding about the wettability transition associated with the chemical content, different analysis on the pillar-like structures were carried out. In the first set of experiments, EDX analyses were obtained on the produced hierarchical pillar-like structures they are shown in Fig. 60. The EDX maps corresponding to the elements O and C indicate higher intensity regions at the interference minima positions, which are correlated with the lines fabricated by the second irradiation, while the element Fe is distributed mainly on the top of the micro pillars.
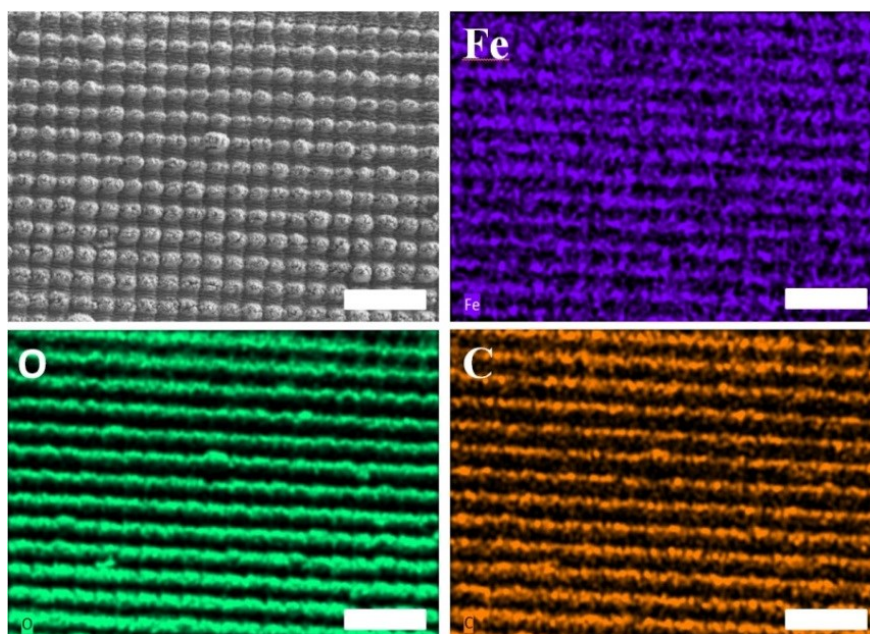
Fig. 60. EDX maps carried out on the hierarchical pillar-like structures showing the elements Fe, O, C. The scale bar is 20 μm. Analysis carried out after 6 months the irradiation. The fabrication parameters used during the ps-DLIP process are $\Lambda = 5.20$ μm, $\tau = 10$ ps, $\lambda = 1064$ nm, $F = 0.74$ J/cm^2 and OV = 99 %.

The chemical composition of the treated surfaces was obtained by EDX analyses on the single-scale (ps-DLIP + ns) and hierarchical pillar-like structures (ps-DLIP). SEM images of the evaluated surfaces are shown in Fig. 61, while their measured chemical compositions are described in Table 1. Two different measurements were carried out according to the data shown in Fig. 59: (i) 7 days after the irradiation, when both samples showed a hydrophilic state, and (ii) 76 days after the laser treatment, when both samples achieved a hydrophobic state.
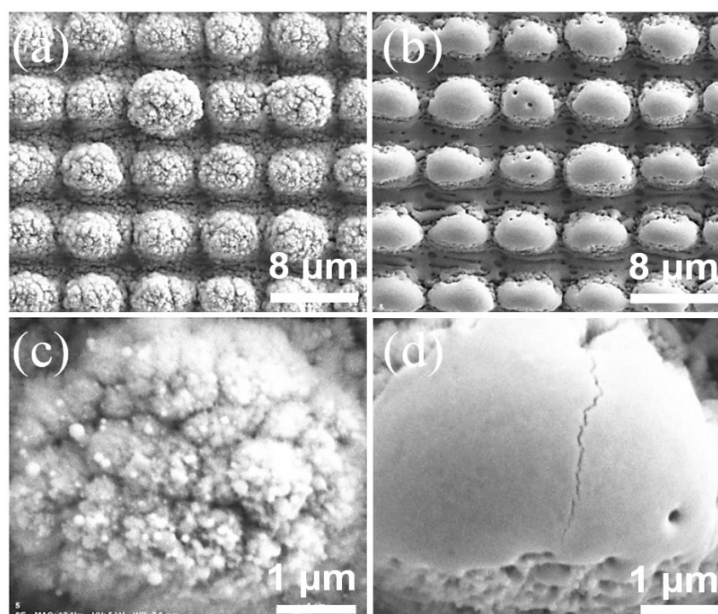
Fig. 61. SEM images of stainless steel samples processed by ps-DLIP with pillar-like topographies, (a, c) hierarchical structures and (b, d) single-scale structures after the nanosecond laser treatment (at $F = 0.27$ J/cm²). Figures (c) and (d) show a higher magnification image corresponding to the top of each pillar.

Table 1. Chemical composition C, O, Fe and Cr elements (at %) for the hierarchical structures (ps-DLIP) and single-scale (ps-DLIP + ns) treated surfaces (corresponding to Fig. 61) measured by EDX.

Sample	C (at %)	O (at %)	Fe (at %)	Cr (at%)
Untreated	5.8	7.7	70.4	16.1
ps-DLIP (after 7 days)	8.1	62.4	23.8	5.7
ps-DLIP + ns (after 7 days)	2.2	66.9	24.9	6.0
ps-DLIP (after 76 days)	11.4	47.5	33.7	7.4
ps-DLIP + ns (after 76 days)	3.3	46.0	40.2	10.4

As can be seen in Table 1, after 7 days, an increase in the carbon content was found for the hierarchical pillar-like structures (ps-DLIP). However, in case of the single-scale structures (ps-DLIP + ns), a decrease of carbon content in respect to the untreated reference was observed. This result suggests that the ns-laser treatment leads to reduction in the carbon content.

In general, it can be deducted that the ps-DLIP process in a two-beam configuration promotes and oxidation as well as carbon enrichment on the pillar-like structures. A confirmation of this increment is verified by the Raman spectrum depicted in Fig. 62. It compares the Raman spectrum of the unstructured material and the hierarchical pillar-like structures represented by the black line and red line respectively.
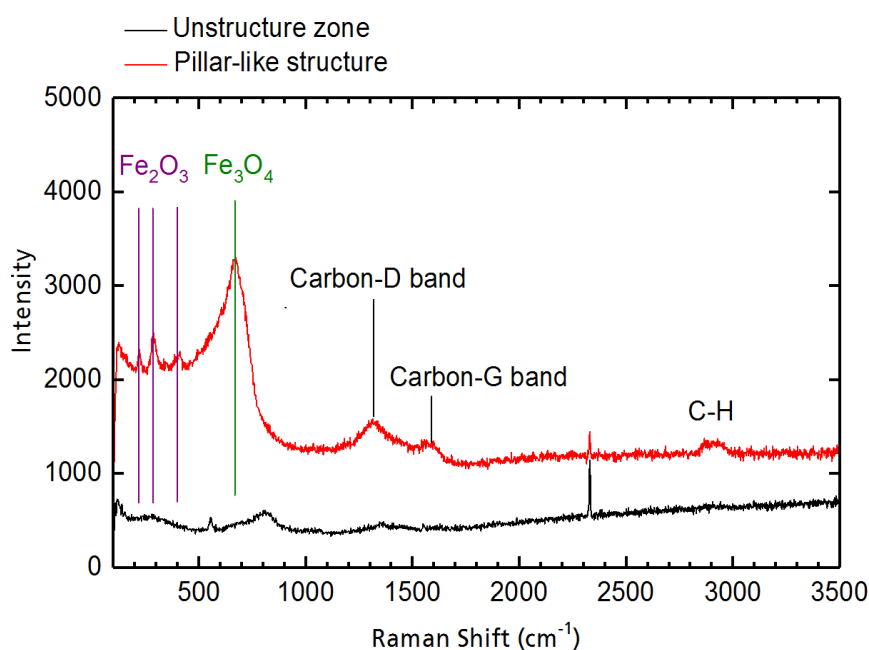
Fig. 62. Raman spectrum of hierarchical pillar-like structures fabricated on stainless steel using ps-DLIP with Λ = 5.20 μm, F = 0.74 J/cm^2 and an OV = 99 %. Black line depicts the Raman spectrum of the unstructured surface.

The results show that the G-peak at 1300 cm^{-1} and the G-peak centred around 1500-1700 cm^{-1} are increased. This suggest that the hierarchical pillar-like structures fabricated by ps-DLIP can originate the sp^2 ring structure in disorder graphite with the peak at 1332 cm^{-1} [238]. The oxygen bonds with Fe illustrate also an increment at four peaks corresponding to hematite (Fe_2O_3) and magnetite (Fe_3O_4).

Furthermore, for a more precise analysis of the chemical composition, XPS analyses were performed on the treated samples. Table 2 shows the data retrieved on the hierarchical (ps-DLIP) and single-scale structures (ps-DLIP + ns) 2 and 53 days after the fabrication.

Table 2. Surface composition (at. %) of the hierarchical (ps-DLIP) and single-scale (ps-DLIP + ns) after 2 days and 53 days measured by XPS.

Sample	C 1s (at%)	O 1s (at%)	Fe 3p (at%)	C/Fe	C/O
ps-DLIP (after 2 days)	48.66	37.42	13.92	3.49	1.30
ps-DLIP + ns (after 2 days)	36.78	39.57	23.65	1.55	0.92
ps-DLIP (after 53 days)	50.70	37.14	12.16	4.16	1.36
ps-DLIP + ns (after 53 days)	40.27	39.46	20.26	1.98	1.02

According to the XPS measurement, an increase in carbon content was measured on the treated samples after 53 days the irradiation. This highlight that the transition from the hydrophilic to the hydrophobic state is related to the decomposition of CO_2 into carbon (accumulation of non-polar carbon compounds), which is promoted over time due to the activation of iron oxides by the laser radiation [178]. This is typically observed when irradiated metal surfaces are exposed to ambient air or a CO_2 atmosphere [185]. The produced non-polar chemical groups on the surface reduce the wettability due to their low interaction with the polar forces and the low possibility of creating hydrogen bonds with the water molecules [162]. This reduces the surface free energy, and thus the SWCA is increased. Furthermore, it has been proposed in several works [176], [239], [240] that the ratio of C/Fe provides an idea of the relative amount of adsorbed non-polar carbon compounds. In our case, the atomic ratios of C/Fe at 2 and 53 days after laser treatment increased from 3.49 to 4.16 and from 1.55 to 1.98 for hierarchical pillar-like structures (ps-DLIP) and single-scale geometry (ps-DLIP + ns), respectively. Accordingly, this means that the polarity of the surface is also reduced, resulting in a higher hydrophobicity of the surface. The ratio C/O did not change (considering the measurement error is approximately +/-0.5 at. %) over time, which indicates the stable proportion of the C-O bounds.

7.1.3   Wetting response after the chemical surface modification

Due to the measured difference in the surface chemistry for both laser treated samples, it was proceeded to modify the chemistry of the used stainless steel samples by dipping them in a hydrophobizing agent (Mecasurf®, Surfactis). In order to provide the samples with an equal surface chemistry, new samples with single- and hierarchical topographies were fabricated and immediately after the laser treatments were chemically treated by dipping them in a hydrophobizing agent (Mecasurf®). After the chemical treatment, both SWCA and CAH angles were measured and the outcomes are shown in Fig. 63. The image also includes the wettability results for the surfaces without

the chemical treatment 90 days after the laser treatments (when the steady-state condition was reached).
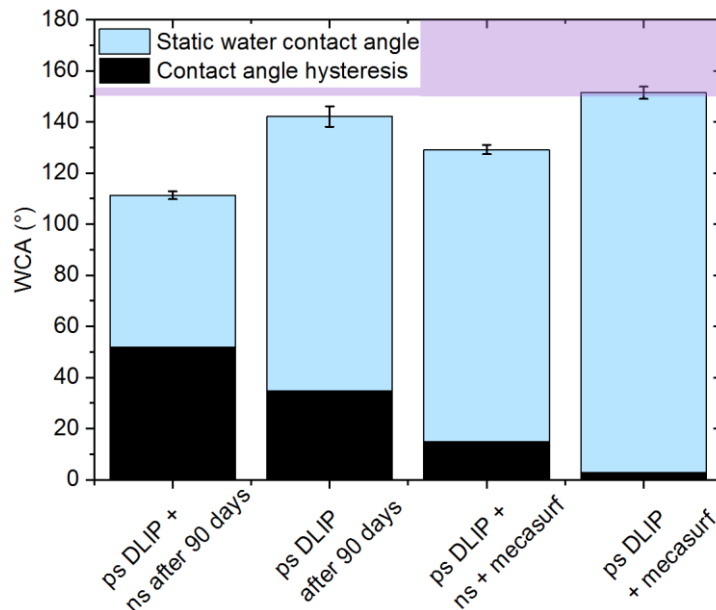
Fig. 63. Static water contact angle (SWCA) and contact angle hysteresis (CAH) on the hierarchical (ps-DLIP) and single-scale structures (ps-DLIP + ns) measured 90 days after the laser treatment. New surfaces with the same topographies were treated with a hydrophobizing agent, permitting the hierarchical pattern (ps-DLIP + Mecasurf) to achieve superhydrophobic behaviour. The values are an average of four SWCA measurements, the error bars were estimated by their standard deviation.

As can be observed, the superhydrophobic condition was only achieved on the hierarchical surface pattern (ps-DLIP) covered by the hydrophobic coating (Mecasurf®). In the last case, the SWCA and CAH values were 152 ° ± 2 ° and 4 ° ± 2 °, respectively. In the case of the single-scale geometry (ps-DLIP + ns) also covered by the hydrophobic coating, the SWCA of 129 ° ± 3 ° was measured, what is approximately 23 ° lower than the hierarchical pattern. The measured CAH was 15 °, which also denotes the lower ability of the water droplets to roll over on the surface material. The results obtained for the original samples, without the Mecasurf® treatment, show lower SWCAs as well as higher CAH values. However, also in this case, the hierarchical structures showed a better hydrophobic performance compared to the single-scale structure.

The results suggest that the hierarchical DLIP structures in conjunction with a surface chemistry modification promote superhydrophobic conditions. On the contrary, single-scale micro-pillars showed, independent of the surface chemistry, a poor performance compared to the hierarchical structures, confirming the importance of multi-scaled surface patterns for tailoring the wettability of metals.

Finally, for the large aircraft surface (Ti6Al4V) presented in Chapter 5.4, the hydrophobizing agent Mecasurf® was also applied in order to enhance the wetting behaviour. After applying Mecasurf® on the hierarchical pillar-like structures, the SWCA increased up to 158 °, also with CAH

less than 8 °. Furthermore, the untreated surface depicts SWCA values of 47.7 ° ± 5, while after applying Mecasurf® it increases up to 65 ° ± 5. It is important to mention also that the WCA on the pillar-like structures was measured directly after the ps-DLIP process depicting a hydrophilic state with SWCA values about 5 °.

7.2 Wetting on multi-scale periodic structures fabricated by DLW and DLIP

For the multi-scale microstructures fabricated using DLW and DLIP a hydrophilic character was observed directly after the irradiation, depicting SWCA values lower than 5° for both materials (Ti6Al4V and Al2024).

Specifically, multi-scale periodic structures on Ti6Al4V (showed in Fig. 44) depict SWCA values up to 110° ± 5° after 90 days the DLIP irradiation. Moreover, the SWCA was separately measured in the same period of time on the micro-cells and DLIP pillar-like structures showing values of 90 ± 6° and 65° ± 10°, respectively. The SWCA results suggest a positive influence of the multi-scale periodic microstructures (DLW+DLIP) on the hydrophobic enhancement. However, any superhydrophobic behaviour was observed on the Ti6Al4V structured surfaces in the following 90 days. Further experiments must be carried out in order to associate the wetting transition on titanium with the surface free energy promoted by using short pulse laser sources and the microstructures fabricated.

For the case of multi-scale periodic structures fabricated on Al2024 with the $h = 17$ μm and $h = 35$ μm (Fig. 48 (a) and (b)) the SWCA increased up to 161.5 ° ± 3 ° and of 110.4 ± 3 ° respectively. The SWCA were carried out after one week the DLIP irradiation. The difference in SWCA can be possibly due to the air trapping effect correlated with the exposure of the droplet in the centre region of the microcells. If the hatch distance is decreased, the gap between micro-cell is smaller; therefore droplets have less interaction with the pillar-like structures which could produce an increase on the observed SWCA. After 10 weeks the irradiation, the SWCA measurements depict values larger than 156.0 ° while the CAH is as low as 4 ± 3° on both samples.

In general, the hydrophobic properties on laser treated aluminium surfaces are observed when organic molecules are adsorbed on the surface through interaction with formed hydroxide groups. Then adsorbed short-chained organic molecules stimulate a decrease in the total surface free energy and super-hydrophobic behaviours can be observed on laser treated aluminium surfaces after a period of time. Furthermore, experimental works show that the organic molecules come from and depend on the ambient air moisture [241].

7.3   Tribological properties of laser treated surfaces

The coefficient of friction (CoF) was measured on the hierarchical pillar-like microstructures. For the assessment structures with spatial periods of 2.60 µm and 5.20 µm were fabricated on stainless steel 1.4112 by ps-DLIP. Fluences of $F = 1.45$ J/cm² and $F = 0.84$ J/cm² were used for the first and second irradiation steps, respectively. Two different values of pulse-to pulse-overlap (OV = 91 % and OV = 95 %) were used for the fabrication, producing different structures depths for each spatial period.

The surface characterisation revealed comparable depth values with pillar-like microstructures described in chapter 5.2.3. As aforementioned, for the characterisation of pillar-like structures, the depth at the intersection was considered in order to determine the AR of each pillar-like microstructure. In this set of experiments, the structures fabricated using the $\Lambda = 2.60$ µm at OV values of 91 % and 95 % have AR values of 0.25 and 0.41, while in the case of microstructures using the $\Lambda = 5.20$ µm the AR were 0.07 and 0.26. For the evaluation of the coefficient of friction under different lubrication speeds, the Stribeck curve was extracted. In Fig. 64 is presented the Stribeck curves measured for the four different pillar-like structures and the untreated surface material. It depicts the sliding speed as a function of the CoF.
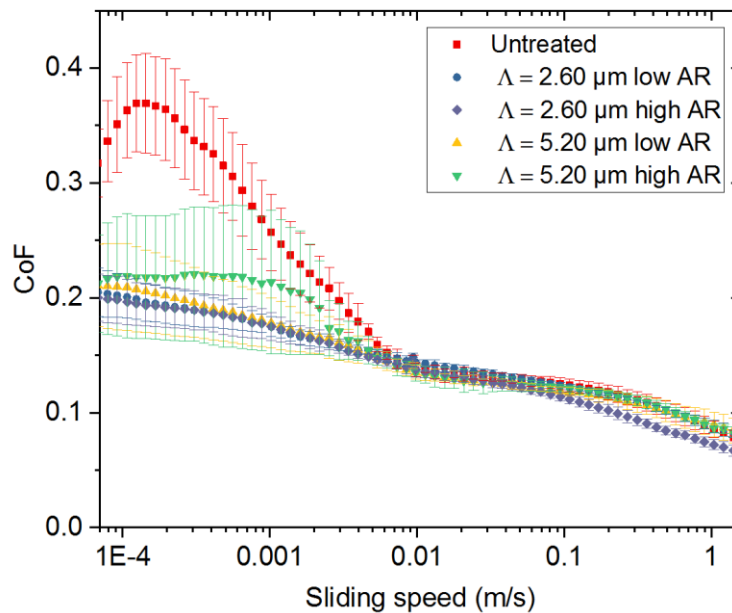
Fig. 64. Stribeck curve measured on pillar-like structures fabricated by ps-DLIP with to different spatial periods and two AR. The red points denote measurements for the untreated surface.

The CoF on the pillar-like structures compared to the untreated surface was reduced from 0.37 to 0.22 for the speed of 1.6×10^{-4} m/s, it represents about 40 % reduction for the CoF. As can be observed in Fig. 64, the reduction of the CoF was achieved specially for sliding speeds below 10×10^{-3} m/s, associated with a boundary lubricated regime [242]. Moreover, it can be observed that

for the microstructures with $\Lambda = 5.20$ µm and high AR, there is an increase of the CoF in this regime when it is compare with the other three microstructured samples. It can be attributed to higher depths at the intersection of the pillars which increase slightly the CoF on the top of the pillars.

These results suggest that the microstructures can impact the reduction of friction for low sliding speeds for a determined pressure. It is highlighted that the microstructures fabricated with the smaller spatial period ($\Lambda = 2.60$ µm) led to a lower CoF compare to the larger spatial period ($\Lambda = 5.20$ µm). This effect can be connected with the capillary force inside the microstructures which increases for smaller spatial periods. This phenomenon can be approached as an active lubricant transport in the microstructures which can avoid starvation in the tribocontact [243].

7.4   Influence of laser treated surfaces on fatigue

Laser surface texturing is a process intended to improve surface properties, but not necessarily the fatigue properties. In fact, surface roughness can limit the mechanical capacity of a cyclic loaded part [47]. In this perspective, the DLIP process produces a surface roughness which can lead to micro-cracking [244]. However, the goal of this section was to obtain quantitative data on the high cycle fatigue behaviour of ps-DLIP structures. Thus, line and pillar-like microstructures were fabricated on Ti6Al4V using a $\Lambda = 5.20$ µm. In Fig. 65 (a) and (b) are presented the confocal images of the evaluated line-like structures and the pillar-like structures, respectively.
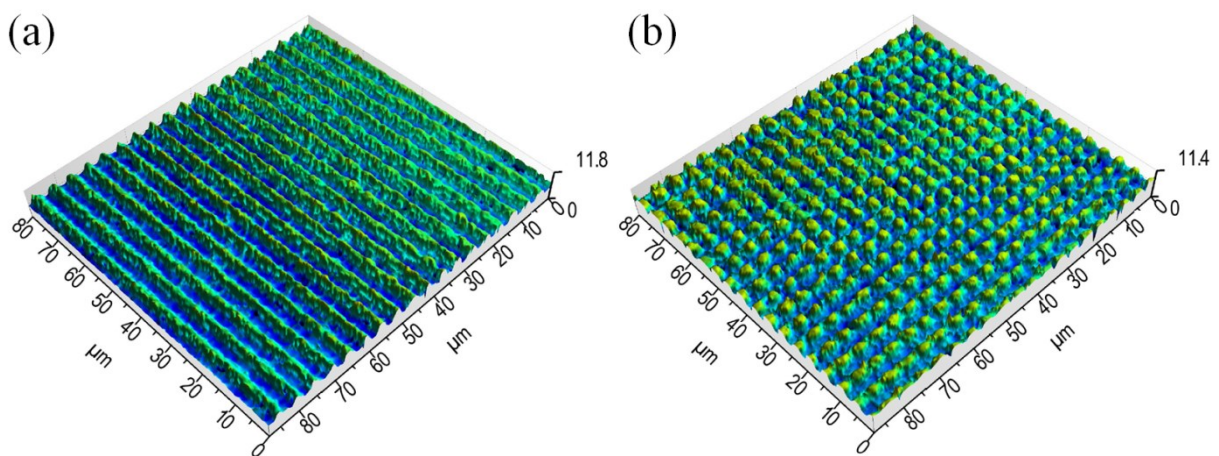
Fig. 65. Characteristic confocal microscopy images of produced (a) line-like and (b) pillar-like patterns on Ti6Al4V. The $\Lambda = 5.20$ µm, OV = 99 %, f = 10 kHz and F = 0.74 J/cm² were used for both topographies.

The stress ranges corresponding to unstructured, line- and pillar-like structured samples are shown in Fig. 66.
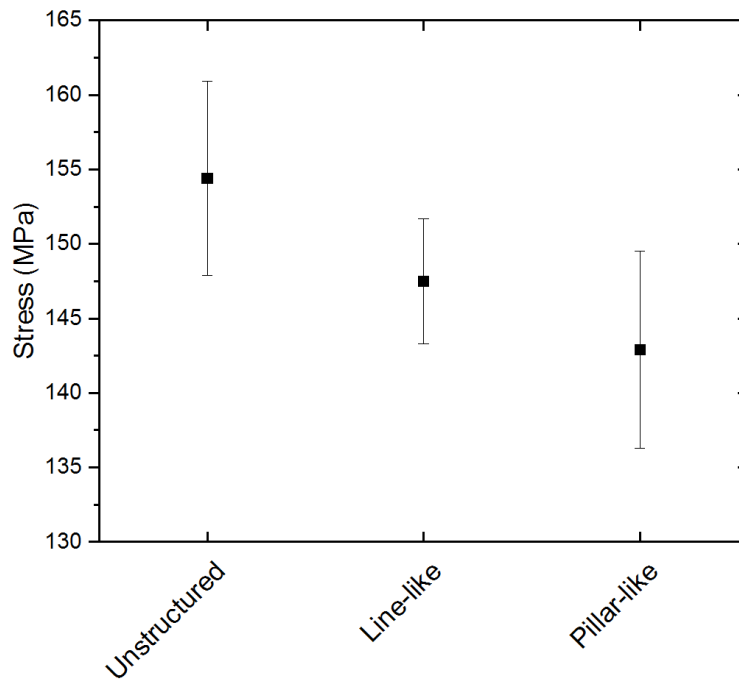
Fig. 66. Representation of stress range measured on unstructured, line- and pillar-like structured Ti6Al4V samples using ps-DLIP and parameters of $\Lambda = 5.20$ μm, OV = 99 %, $f = 10$ kHz and $F = 0.74$ J/cm². The parameters were kept constant for the second irradiation step for pillar-like structures.

The load increasing testing method was used for the analysis of the results which were monitored and observed with a camera system during the fatigue tests [245]. The outcomes are summarized in Table 3, where the mean load capacity value for a long term stress in the line-like structures was reduced to 95.5 % and for the pillar-like structures 92.6 %, if they are compared with the unstructured samples.

Table 3. Mean load capacity values of unstructured sample, line-like and pillar-like structures fabricated by ps-DLIP using a $\Lambda = 5.20$ μm, OV = 99 %, $f = 10$ kHz and $F = 0.74$ J/cm².

	Unstructured samples	Line-like structures	Pillar-like structures
Mean load capacity (MPa)	154.4	147.5	142.9
Percentage strength in long-term stress (%)	100	95.5	92.6
Standard deviation	6.5	4.2	6.6

The results show a slightly impact from the ps-DLIP process on the mean load capacity. For the pillar- and line-like structures mean load capacity values of 147.4 MPa and 142.9 MPa were measured, respectively. It is noticeable a lower mean load capacity on the pillar-like structures, which can be correlated with the microstructure depth fabricated due to the two irradiation steps. The mean structure depth of 3.40 µm was fabricated at the interference maxima-maxima positions, while the mean depth of 2.21 µm was achieved on the line-like structures. This difference in depth must be considered as a notch factor on the cross-like structures which can promote a crack initiation.

In accordance with the results, the influence of the ps-DLIP process on the long term stress of the material is not significant. However, due to the small number of evaluated samples, it is difficult to make an absolute statistically reliable statement about the exact influence of the laser structuring. Furthermore, possible influences of the DLIP process on the crystal structure which could result in a different mechanical behaviour must be investigated in the future.

8.   Conclusions and outlook

Surface texture homogeneity

A strategy for the fabrication of homogeneous microstructures using ns-DLIP based on Gaussian beams (TEM00) was developed. It was shown that homogeneous microstructures can be fabricated on large areas if the hatch distance (h) and the pulse-to-pulse overlap (OV) (values between successive laser pulses) are optimised. A quantitative measurement scheme of the pattern homogeneity based on topographical measurements such as standard deviation (Sd), mean structure height (RcA) and kurtosis (Rku) was introduced. Furthermore, the influence of a second produced periodic modulation ($RcMod$) arising from the utilised hatch distance was identified as the most sensitive parameter during the surface assessment. As quantitative parameter, the surface error ($Surf\ Err\ \%$) was introduced and employed for the characterisation of the surface homogeneity.

Based on the measured experimental data, the effect of different laser process parameters on the produced surface texture homogeneity can be summarised as follows:

- h has a relevant importance on the second produced periodic modulation; it must be a multiple of the spatial period and smaller than the laser interference area ($\varnothing$) (~ 18 % of the Gaussian intensity distribution in order to achieve a high surface homogeneity > 75%).
- OV has a strong influence on the structure depth. The observed trend is that samples treated with high OV values depict a higher surface homogeneity.
- Rku values cannot be used strictly to quantify homogeneity, but they can provide an idea of the kind of topographic profile. Samples with Rku values corresponding to a sinus shape (~1.5) have in general, a high surface homogeneity.

The here presented processing strategy is of significant relevance to assure in the future a certain homogeneity performance over the whole treated area. In addition, the used parameters for the quantitative characterisation of the surface texture homogeneity could be fundamental in relevant industrial processes, especially for quality management.

Hierarchical periodic micro/nano structures

In this work, the fabrication of periodic microstructures produced by ps-DLIP on metallic surfaces was also investigated. The surface treatment of metallic samples with a two-beam interference configuration and a picosecond laser source allowed producing hierarchical micro and nano surface structures. They consist of line- and pillar-like microstructures combined with LIPSS features, which mimic the surface textures observed on different leafs with superhydrophobic properties. These mimetic hierarchical microstructures were fabricated on stainless steel and titanium.

Line- and pillar-like periodic surface microstructures with high Aspect Ratio (AR) were fabricated on stainless steel using ps-DLIP. For the line-like microstructures, depths up to 4.90 µm and

2.50 μm can be obtained using the spatial periods of Λ = 5.20 μm and the Λ = 2.60 μm, respectively. Pillar-like microstructures were produced using a two-step irradiation process. Thereby, a surface characterisation method was implemented. It considers three different depths in the micro-pillars, corresponding to the interception of an interference maxima with an interference minima (in both *x* and *y* direction) and the interception of two interference maxima. Subsequently, the intersection depth in the micro-pillars (interference maxima-maxima) provides ARs up to 2.21. In addition to the microstructures that correspond to the intensity distribution of the interference patterns, also LSFL and HSFL were observed with spatial periods of approximately 800 nm and 200 nm, respectively. The orientation of such sub-microstructures was investigated by using the linear and the circular laser beam polarisations.

The findings of this section are summarised as follows:

- DLIP microstructures combined with LIPSS can be fabricated simultaneously in a single-step irradiation process using picosecond laser sources.

- Hierarchical micro-pillars with interception depths up to 11.50 μm and spatial period of Λ = 5.20 μm can be fabricated by ps-DLIP.

- A determined linear beam polarisation state used during ps-DLIP processes, permits controlling the orientation of LSFL and HSFL.

- For the circular beam polarisation state, the HSFL denote an aleatory orientation, while LSFL are not well-defined.

Multi-scale periodic structures combining DLIP and DLW

The combination of two laser-based methods allows producing multi-scale hierarchical microstructures on Ti6Al4V and Al2024. The first step process based on nanosecond DLW permits the fabrication of squared shaped micro-cells which consist in a succession of lines intersecting themselves at 90°. Afterwards, picosecond DLIP was used to generate pillars-like structures in the micro-cells. In general, independently of the substrate material, the fluence should be reduced during the second ps-DLIP process in order to fabricate micro-pillars.

Analytical ablation model

In the framework of throughput using infrared ps-DLIP in the two-beam configuration, the following remarks are pointed out.

An analytical ablation model used to estimate the microstructure depth as a function of the diameter of the laser interference area and OV was developed. In consequence, the optimised process parameters to reach a certain structure depth at the maximal possible throughput were determined. The proposed model predicts a wide range of structure depths that can be reached. These results indicate that for a given laser power, the laser interference area and OV must be controlled in order to achieve

the highest throughput of the DLIP process. Moreover, the model results are in a good agreement with the experiments. For instance, in order to achieve 500 nm in depth on stainless steel using the $\Lambda = 5.50\ \mu m$, $f = 1$ kHz, $\varnothing = 160\ \mu m$ and OV = 91.1 % the achieved throughput is 2.5 cm^2/min, while increasing the $\varnothing = 740\ \mu m$ and OV = 97.6% the throughput also increases to 7.9 cm^2/min which is 3.1 time faster.

As a general trend, during the laser texturing processes the use of a fixed $\varnothing$ and high OV values led to an increase in the processing times. Nevertheless, due to the intrinsic characteristic of the DLIP method, processing times at least three times shorter compared to the state of the art could be achieved, even for the smallest $\varnothing$ here used.

Wetting behaviour

The microstructures fabricated by ps-DLIP were tested in relation to their wetting behaviours. In this context, WCA measurements allowed determining the influence of the topography on the increase of SWCA. Pillar-like structures with the largest AR (i.e. lowest Filling Factor (FF)) exhibit better hydrophobic behaviour (WCA ~ 140 °); it highlights the influence of microstructures with high AR on stainless steel in order to reduce the wetting contact area.

In order to understand the contribution of the different surface features sizes on the SWCA and the CAH, an approach based on the isolation of the primary microstructure produced by ps-DLIP was developed by selectively melting the nano-texture related to LIPSS. This procedure permitted an evaluation of whether nano-scale periodic structures have an impact on wetting. Thus, the wettability properties of two analogous laser-treated samples were evaluated over time, showing that hierarchical microstructures reach a higher SWCA compared to single-scale microstructures. Moreover, the chemical analysis of the two morphologies was compared, where an increased ratio of C/Fe on the surfaces was found 53 days after the laser treatment, which also contributed to the SWCA on both samples. In addition, high water droplet adhesion was identified on the hierarchical microstructures, which leads to high SWCA and high CAH. This wetting regime was correlated with the rose petal effect.

Additionally, the laser processed samples were treated with a hydrophobizing agent in order to confirm the influence of the different feature size on the WCA. In this case, the hierarchical microstructures not only achieved the superhydrophobic condition but also presented a 31 ° higher SWCA than the single-scale micro-pillars.

Lastly, the SWCA measurements on multi-scale hierarchical structures also showed a wetting transition (from the hydrophilic to the hydrophobic state) over time on Ti6Al4V and Al2024. In this context, a positive influence of the multi-scale periodic microstructures (DLW+DLIP) on the enhancement of WCA was also observed. Precisely, SWCA values up to 110° ± 5° on Ti6Al4V were

measured after 90 days the DLIP irradiation, while for the laser treated aluminium surfaces the superhydrophobic state was measured after the same period of time.

Reduction of friction coefficient

In the case of friction reduction, pillar-like microstructures fabricated by ps-DLIP exhibit 40 % reduction of the CoF compared to the untreated stainless steel samples. It was achieved mainly for sliding speeds below 1 cm/s (speed associated with a boundary lubricated regime). The results suggest that the micro-pillars can act as micro reservoirs for oil retention, which can potentially avoid starvation in the tribocontact.

Fatigue

Fatigue tests carried out on Ti6Al4V allowed determining that under a long term stress of the material, pillar and line-like structures fabricated by ps-DLIP do not have a negative impact on fatigue properties. However, possible influences of the ps-DLIP process on the crystal structure, which could result in a different mechanical behaviour, must be investigated in the future.

Outlook

The promising option of quantify the surface functionality performance in terms of surface texture homogeneity of a treated laser area, would be a useful tool for the development of DLIP processes and its use with in-line monitoring systems. It is important to highlight that the method for characterising a surface highly depends on the topography shape (e.g. line-, dot-, pillar-like). In this context, it must be considered that 2D profiles allow evaluating micro and nano features variation, while 3D surface texture parameters are not designed for the evaluation of heights deviations in local regions. However, investigations of the 3D surface parameters in connection with homogeneity must be carried out, in order to obtain more robust data for the industrial area and develop standard parameters schemes that describe homogeneous surface textures.

Through this work, a general trend was observed when ps-DLIP was used to fabricate pillar-like structures with spatial periods smaller than 3 μm. The depths at the intersections were significantly smaller than the depths in the line-like patterns. Investigations to determine optimal fluences for the second ps-DLIP process in terms of absorption increase are needed. Furthermore, simulations using a large number of laser pulses (e.g. OV > 90%) for the first and second ps-DLIP processes must be carried out to understand the limits of achievable depths as a function of spatial period.

The method here used to fabricate pillar-like structures consists in the fluence reduction for the second ps-DLIP step process. However, another possible approach can be the OV reduction during the second step process. Both methods could be compared from the perspective of the cumulative fluence, in order to improve throughputs for the fabrication of micro-pillars.

Moreover, the impact of the LIPSS direction must be investigated for the fabrication of pillar-like structures with high OV values, e.g. 99 %. It can have a strong influence on the achievable depth and the homogeneity of the micro-pillars.

Finally, it was shown that the results of the analytical model were confirmed by the experiments carried out using the spatial period of 5.50 µm. However, in the future other spatial periods must be used in order to determine the limits of the model.

References

[1] B.-C. Yoseph, *Biomimetics: biologically inspired technologies*, vol. 9, no. 3. 2006.

[2] W. Barthlott, M. Mail, and C. Neinhuis, "Superhydrophobic hierarchically structured surfaces in biology : evolution , structural principles and biomimetic applications," *Philos. Trans. R. Soc. A*, vol. 374, no. 20160191, 2016.

[3] R. Spolenak, S. Gorb, and E. Arzt, "Adhesion design maps for bio-inspired attachment systems," vol. 1, pp. 5–13, 2005.

[4] W. M. Steen and M. J., *Laser Material Processing*, Springer-V., vol. 1, no. 0. London, 2010.

[5] D. Kleppner, "Rereading Einstein," *Phys. Today*, no. February, 2005.

[6] A. Einstein, "On the quantum theory of radiation (Translated version by D. ter Haar,"The Old Quantum Theory", Pergamon Press, New York (1967), p.167)," *Phys. Z.*, vol. 18, no. 121, 1917.

[7] T. H. Maiman, "Stimulated optical radiation in ruby," vol. 187, no. 4736, pp. 493–494, 1960.

[8] R. Crafer, *Laser Processing in Manufacturing Engineering*. Great Britain: Chapmann & hall, 1993.

[9] M. Fox, *Optical Properties of Solids*. New York: Oxford university press, 2001.

[10] P. Johnson and R. Christy, "Optical constants of transition metals: Ti, V, Cr, Mn, Fe, Co, Ni, and Pd," *Phys. Rev. B*, vol. 9, no. 12, pp. 5056–5070, 1974.

[11] A. D. Rakic, "Algorithm for the determination of intrinsic optical constants of metal films: application to aluminum," *Appl. Opt.*, vol. 35, no. 22, pp. 4755–4767, 1995.

[12] R. C. Hilborn, "Einstein coefficients, cross sections, f values, dipole moments, and all that," *Am. J. Phys.*, vol. 50, pp. 982–986, 1982.

[13] M. S. Brown and C. B. Arnold, *Laser Precision Microfabrication, Chapter 4*. Springer Berlin Heidelberg, 2010.

[14] D. W. Bäuerle, *Laser Processing and Chemistry*. 1996.

[15] J. C. Ion, *Laser Processing of Engineering Materials: Principles, Procedure and Industrial Application*. 2005.

[16] V. V Semak, W. D. Bragg, B. Damkroger, V. Semak, and A. Matsunawa, "The role of recoil pressure in energy balance during laser materials processing," 1997.

[17] A. H. Hamad, "Effects of Different Laser Pulse Regimes (Nanosecond, Picosecond and Femtosecond) on the Ablation of Materials for Production of Nanoparticles in Liquid Solution," Manchester, UK: Intech open science, 2016, pp. 309–316.

[18] P. Gečys, A. Vinčiunas, M. Gedvilas, A. Kasparaitis, R. Lazdinas, and G. Račiukaitis, "Ripple formation by femtosecond laser pulses for enhanced absorptance of stainless steel," *J. Laser Micro Nanoeng.*, vol. 10, no. 2, pp. 129–133, 2015.

[19] D. Wang *et al.*, "Both antireflection and superhydrophobicity structures achieved by direct laser interference nanomanufacturing," *J. Appl. Phys.*, vol. 115, no. 23, 2014.

[20] D. S. Milovanović *et al.*, "Titanium alloy surface modification by excimer laser irradiation," *Opt. Laser Technol.*, vol. 54, pp. 419–427, 2013.

[21] C. Momma, S. Nolte, B. N. Chichkov, F. V. Alvensleben, and A. Tünnermann, "Precise laser ablation with ultrashort pulses," *Appl. Surf. Sci.*, vol. 109–110, pp. 15–19, 1997.

[22] B. N. Chichkov, C. Momma, S. Nolte, F. von Alvensleben, and A. Tünnermann, "Femtosecond, picosecond and nanosecond laser ablation of solids," *Appl. Phys. A Mater. Sci. Process.*, vol. 63, no. 2, pp. 109–115, 1996.

[23] P. T. Mannion, J. Magee, E. Coyne, G. M. O'Connor, and T. J. Glynn, "The effect of damage accumulation behaviour on ablation thresholds and damage morphology in ultrafast laser micro-machining of common metals in air," *Appl. Surf. Sci.*, vol. 233, no. 1–4, pp. 275–287, 2004.

[24] J. Byskov-Nielsen, J. M. Savolainen, M. S. Christensen, and P. Balling, "Ultra-short pulse laser ablation of metals: Threshold fluence, incubation coefficient and ablation rates," *Appl. Phys. A Mater. Sci. Process.*, vol. 101, no. 1, pp. 97–101, 2010.

[25] G. H. Seward, *Basic Physical Optics*. 2008.

[26] H. Van Wolferen and L. Abelmann, "Laser Interference Lithography," in *Lithography: pronciples, process and materials*, 2011, pp. 133–148.

[27] V. Furlan, M. Biondi, A. G. Demir, G. Pariani, B. Previtali, and A. Bianco, "Sub-micrometric surface texturing of AZ31 Mg-alloy through two-beam direct laser interference patterning with a ns-pulsed green fiber laser," *Appl. Surf. Sci.*, vol. 423, pp. 619–629, 2017.

[28] T. Jähnig, A. Mousavi, V. Lang, K. Tim, A. Brosius, and A. F. Lasagni, "High-speed Direct Laser Interference Patterning of sheet metals for friction High-speed Direct Laser Interference Patterning of sheet metals for friction reduction in deep drawing processes," *Dry Met. Form.*, vol. 4, no. August, pp. 62–67, 2018.

[29] R. N. Wenzel, "Resistance of solid surfaces to wetting by water," *Ind. Eng. Chem.*, vol. 28, no. 8, pp. 988–994, 1936.

[30] A. B. D. Cassie and S. Baxter, "Wettability of porous surfaces," *Trans. Faraday Soc.*, vol. 40, no. 5, pp. 546–551, 1944.

[31] L. Mahadevan and Y. Pomeau, "Rolling droplets," *Phys. Fluids*, vol. 11, no. 9, pp. 2449–2453, 1999.

[32] K. Mittal, *Advances in Contact Angle, Wettability and Adhesion*, vol. 2. 2015.

[33] R. Blossey, "Self-cleaning surfaces - virtual realities," *Nat. Mater.*, vol. 2, no. 5, pp. 301–306, 2003.

[34] H. K. Webb, R. J. Crawford, and E. P. Ivanova, "Wettability of natural superhydrophobic surfaces," *Adv. Colloid Interface Sci.*, vol. 210, pp. 58–64, 2014.

[35] J. Long *et al.*, "Superhydrophobic surfaces fabricated by femtosecond laser with tunable water adhesion: From lotus leaf to rose petal," *ACS Appl. Mater. Interfaces*, vol. 7, no. 18, pp. 9858–

9865, 2015.

[36] B. Bhushan and M. Nosonovsky, "The rose petal effect and the modes of superhydrophobicity," *Philos. Trans. R. Soc. A Math. Phys. Eng. Sci.*, vol. 368, no. 1929, pp. 4713–4728, 2010.

[37] M. Nosonovsky and B. Bhushan, *Multiscale Dissipative Mechanisms and Hierarchical Surfaces*. 2008.

[38] B. Bhushan, *Introduction to tribology*. 2013.

[39] P. B. Abe and J. Ferrante, "Surface physics in tribology," *Mod. Tribol. Handb. Vol. One Princ. Tribol.*, pp. 5–47, 2000.

[40] K. Holmberg and A. Erdemir, "Global impact of friction on energy consumption, economy and environment," *FME Trans.*, vol. 43, no. 3, pp. 181–185, 2015.

[41] K. Holmberg, P. Andersson, and A. Erdemir, "Global energy consumption due to friction in passenger cars," *Tribol. Int.*, vol. 47, pp. 221–234, 2012.

[42] M. Sedlaček, L. M. S. Vilhena, B. Podgornik, and J. Vižintin, "Surface topography modelling for reduced friction," *Stroj. Vestnik/Journal Mech. Eng.*, vol. 57, no. 9, pp. 674–680, 2011.

[43] W. Tang, Y. Zhou, H. Zhu, and H. Yang, "The effect of surface texturing on reducing the friction and wear of steel under lubricated sliding contact," *Appl. Surf. Sci.*, vol. 273, pp. 199–204, 2013.

[44] Y. H. Chae, "Effect of Size for Micro-Scale Dimples on Surface under Lubricated Sliding Contact," *Key Eng. Mater.*, vol. 345–346, pp. 765–768, 2009.

[45] C. H. Tai, J. C. Leong, and C. Y. Lin, "Effects of golf ball dimple configuration on aerodynamics, trajectory, and acoustics," *J. Flow Vis. Image Process.*, vol. 14, no. 2, pp. 183–200, 2007.

[46] D. Gropper, L. Wang, and T. J. Harvey, "Hydrodynamic lubrication of textured surfaces: A review of modeling techniques and key findings," *Tribol. Int.*, vol. 94, pp. 509–529, 2016.

[47] U. Zerbst, M. Madia, M. Vormwald, and H. T. Beier, "Fatigue strength and fracture mechanics – A general perspective," *Eng. Fract. Mech.*, vol. 198, pp. 2–23, 2018.

[48] ISO 12107, *Metallic materials-Fatigue testing-Statistical planning and analysis of data*, no. Second edition. 2012.

[49] F. Walther, "Microstructure-oriented fatigue assessment of construction materials and joints using short-time load increase procedure," *Mater. Test.*, vol. 56, no. 7–8, pp. 519–527, 2014.

[50] W. Barthlott and C. Neinhuis, "Purity of the sacred lotus, or escape from contamination in biological surfaces," *Planta*, vol. 202, no. 1, pp. 1–8, 1997.

[51] W. Barthlott, M. Mail, B. Bhushan, and K. Koch, "Plant surfaces: Structures and functions for biomimetic innovations," *Nano-Micro Lett.*, vol. 9, no. 2, pp. 1–40, 2017.

[52] T. Wagner, C. Neinhuis, and W. Barthlott, "Wettability and Contaminability of Insect Wings as a Function of Their Surface Sculptures," vol. 77, no. 3, pp. 213–225, 1996.

[53]   J. Oeffner and G. V. Lauder, "The hydrodynamic function of shark skin and two biomimetic applications," *J. Exp. Biol.*, vol. 215, no. 5, pp. 785–795, 2012.

[54]   D. Y. Zhang, Y. H. Luo, X. Li, and H. W. Chen, "Numerical simulation and experimental study of drag-reducing surface of a real shark skin," *J. Hydrodyn.*, vol. 23, no. 2, pp. 204–211, 2011.

[55]   Z. W. Han *et al.*, "Antireflective surface inspired from biology: A review," *Biosurface and Biotribology*, vol. 2, no. 4, pp. 137–150, 2016.

[56]   G. D. Bixler and B. Bhushan, "Rice- and butterfly-wing effect inspired self-cleaning and low drag micro/nanopatterned surfaces in water, oil, and air flow," vol. 6, no. 76, pp. 76–96, 2014.

[57]   R. Helbig, J. Nickerl, C. Neinhuis, and C. Werner, "Smart skin patterns protect springtails," *PLoS One*, vol. 6, no. 9, pp. 2–7, 2011.

[58]   R. Hensel, R. Helbig, S. Aland, A. Voigt, C. Neinhuis, and C. Werner, "Tunable nano-replication to explore the omniphobic characteristics of springtail skin," *NPG Asia Mater.*, vol. 5, no. 1, 2013.

[59]   H. J. Ensikat, P. Ditsche-Kuru, C. Neinhuis, and W. Barthlott, "Superhydrophobicity in perfection: The outstanding properties of the lotus leaf," *Beilstein J. Nanotechnol.*, vol. 2, no. 1, pp. 152–161, 2011.

[60]   P. Wagner, R. Fürstner, W. Barthlott, and C. Neinhuis, "Quantitative assessment to the structural basis of water repellency in natural and technical surfaces," *J. Exp. Bot.*, vol. 54, no. 385, pp. 1295–1303, 2003.

[61]   C. W. Extrand and S. I. Moon, "Repellency of the lotus leaf: Contact angles, drop retention, and sliding angles," *Langmuir*, vol. 30, no. 29, pp. 8791–8797, 2014.

[62]   L. Feng, Y. Zhang, Y. Cao, X. Ye, and L. Jiang, "The effect of surface microstructures and surface compositions on the wettabilities of flower petals," *Soft Matter*, vol. 7, no. 6, pp. 2977–2980, 2011.

[63]   P. Wagner, R. Fürstner, W. Barthlott, and C. Neinhuis, "Quantitative assessment to the structural basis of water repellency in natural and technical surfaces," *J. Exp. Bot.*, vol. 54, no. 385, pp. 1295–1303, 2003.

[64]   Y. T. Cheng, D. E. Rodak, C. A. Wong, and C. A. Hayden, "Effects of micro- and nano-structures on the self-cleaning behaviour of lotus leaves," *Nanotechnology*, vol. 17, no. 5, pp. 1359–1362, 2006.

[65]   G. D. Bixler and B. Bhushan, "Shark skin inspired low-drag microstructured surfaces in closed channel flow," *J. Colloid Interface Sci.*, vol. 393, no. 1, pp. 384–396, 2013.

[66]   Y. Luo, D. Zhang, and Y. Liu, "Recent Drag Reduction Developments Derived From Different Biological Functional Surfaces: a Review," *J. Mech. Med. Biol.*, vol. 16, no. 02, p. 1630001, 2016.

[67]   A. Y. Vorobyev and C. Guo, "Colorizing metals with femtosecond laser pulses," *Appl. Phys.*

Lett., vol. 92, no. 4, pp. 2006–2009, 2008.

[68] B. Sharma, R. R. Frontiera, A. I. Henry, E. Ringe, and R. P. Van Duyne, "SERS: Materials, applications, and the future," *Mater. Today*, vol. 15, no. 1–2, pp. 16–25, 2012.

[69] Y. Fainman, L. P. Lee, D. Psaltis, and C. Yang, *Optofluidics Fundamentals, Devices and Applications*. Mc Graw Hill, 2010.

[70] F. Martín and J. Bonache, "Application of RF-MEMS-Based split ring resonators (SRRs) to the implementation of reconfigurable stopband filters: A review," *Sensors (Switzerland)*, vol. 14, no. 12, pp. 22848–22863, 2014.

[71] H. K. Raut, V. A. Ganesh, A. S. Nair, and S. Ramakrishna, "Anti-reflective coatings: A critical, in-depth review," *Energy Environ. Sci.*, vol. 4, no. 10, pp. 3779–3804, 2011.

[72] E. Fadeeva, A. Deiwick, B. Chichkov, and S. Schlie-Wolter, "Impact of laser-structured biomaterial interfaces on guided cell responses," *Interface Focus*, vol. 4, no. 1, 2014.

[73] O. Tricinci, T. Terencio, B. Mazzolai, N. M. Pugno, F. Greco, and V. Mattoli, "3D Micropatterned Surface Inspired by Salvinia molesta via Direct Laser Lithography," *ACS Appl. Mater. Interfaces*, vol. 7, no. 46, pp. 25560–25567, 2015.

[74] A. Chen, S. J. Chua, P. Chen, X. Y. Chen, and L. K. Jian, "Fabrication of sub-100 nm patterns in SiO2 templates by electron-beam lithography for the growth of periodic III-V semiconductor nanostructures," *Nanotechnology*, vol. 17, no. 15, pp. 3903–3908, 2006.

[75] D. Xia, Z. Ku, S. C. Lee, and S. R. J. Brueck, "Nanostructures and functional materials fabricated by interferometric lithography," *Adv. Mater.*, vol. 23, no. 2, pp. 147–179, 2011.

[76] V. Grigali *et al.*, "Microlens fabrication by 3D electron beam lithography combined with thermal reflow technique," vol. 164, pp. 23–29, 2016.

[77] B. Bhushan, *Nanotribology and Nanomechanics*, 2nd ed. Springer, 2008.

[78] N. J. Shirtcliffe, G. McHale, S. Atherton, and M. I. Newton, "An introduction to superhydrophobicity," *Adv. Colloid Interface Sci.*, vol. 161, no. 1–2, pp. 124–138, 2010.

[79] M. C. Kim, S. H. Yang, J. Boo, and J. G. Han, "Surface treatment of metals using an atmospheric pressure plasma jet and their surface characteristics," vol. 175, pp. 839–844, 2003.

[80] B. Qian and Z. Shen, "Fabrication of Superhydrophobic Surfaces by Dislocation-Selective Chemical Etching on Aluminum , Copper , and Zinc Substrates," no. 19, pp. 9007–9009, 2005.

[81] A. Rockett, *The Materials Science of Semiconductors*. 2008.

[82] Y. Y. Yan, N. Gao, and W. Barthlott, "Mimicking natural superhydrophobic surfaces and grasping the wetting process: A review on recent progress in preparing superhydrophobic surfaces," *Adv. Colloid Interface Sci.*, vol. 169, no. 2, pp. 80–105, 2011.

[83] V. M. Volgin, T. B. Kabanova, and A. D. Davydov, "Modeling of local maskless electrochemical deposition of metal microcolumns," *Chem. Eng. Sci.*, vol. 183, pp. 123–135, 2018.

[84] H. Wang, N. Wang, T. Hang, and M. Li, "Morphologies and wetting properties of copper film

with 3D porous micro-nano hierarchical structure prepared by electrochemical deposition," *Appl. Surf. Sci.*, vol. 372, pp. 7–12, 2016.

[85] R. J. Klein, P. M. Biesheuvel, B. C. Yu, C. D. Meinhart, and F. F. Lange, "Producing super-hydrophobic surfaces with nano-silica spheres," *Z.Metallkd*, vol. 94, no. 4, pp. 377–380, 2003.

[86] G. L. Hornyak, J. Dutta, H. F. Tibbals, and A. Rao, *Introduction to Nanoscience*. CRC Press, 2008.

[87] S. Zhang, J. Qin, C. Yang, X. Zhang, and R. Liu, "Effect of Zr addition on the microstructure and tribological property of the anodization of Ti-6Al-4V alloy," *Surf. Coatings Technol.*, vol. 356, no. September, pp. 38–48, 2018.

[88] N. Sue, "Artificial Lotus Leaf by Nanocasting," no. 20, pp. 8978–8981, 2005.

[89] S. Y. Chou, P. R. Krauss, and P. J. Renstrom, "Imprint of sub-25 nm vias and trenches in polymers," *Appl. Phys. Lett.*, vol. 67, no. 1995, p. 3114, 1995.

[90] L. P. Yeo, S. H. Ng, Z. Wang, Z. Wang, and N. F. de Rooij, "Micro-fabrication of polymeric devices using hot roller embossing," *Microelectron. Eng.*, vol. 86, no. 4–6, pp. 933–936, 2009.

[91] A. Rank, V. Lang, and A. F. Lasagni, "High-Speed Roll-to-Roll Hot Embossing of Micrometer and Sub Micrometer Structures Using Seamless Direct Laser Interference Patterning Treated Sleeves," *Adv. Eng. Mater.*, vol. 19, no. 11, pp. 1–8, 2017.

[92] V. Lang, A. Rank, and A. F. Lasagni, "Large Area One-Step Fabrication of Three-Level Multiple-Scaled Micro and Nanostructured Nickel Sleeves for Roll-to-Roll Hot Embossing," *Adv. Eng. Mater.*, vol. 19, no. 8, pp. 1–9, 2017.

[93] A. Y. Vorobyev and C. Guo, "Direct femtosecond laser surface nano/microstructuring and its applications," *Laser Photonics Rev.*, vol. 7, no. 3, pp. 385–407, 2013.

[94] A. Dunn *et al.*, "Nanosecond laser texturing for high friction applications," *Opt. Lasers Eng.*, vol. 62, pp. 9–16, 2014.

[95] D. Bäuerle, "Laser chemical processing: An overview to the 30th anniversary," *Appl. Phys. A Mater. Sci. Process.*, vol. 101, no. 2, pp. 447–459, 2010.

[96] A. J. Antonczak, D. Kocon, M. Nowak, P. Koziol, and K. M. Abramski, "Laser-induced colour marking - Sensitivity scaling for a stainless steel," *Appl. Surf. Sci.*, vol. 264, pp. 229–236, 2013.

[97] T. Yong Hwang and C. Guo, "Polarization and angular effects of femtosecond laser-induced conical microstructures on Ni," *J. Appl. Phys.*, vol. 111, no. 8, 2012.

[98] B. H. Luo, P. W. Shum, Z. F. Zhou, and K. Y. Li, "Preparation of hydrophobic surface on steel by patterning using laser ablation process," *Surf. Coatings Technol.*, vol. 204, no. 8, pp. 1180–1185, 2010.

[99] R. Gokhale *et al.*, "Laser synthesized super-hydrophobic conducting carbon with broccoli-type morphology as a counter-electrode for dye sensitized solar cells," *Nanoscale*, vol. 4, no. 21, p. 6730, 2012.

[100] V. Y. Balandin and R. Niedrig, "Simulation of transformations laser pulses of thin metal films heated by nanosecond pulses," *J. Appl. Phys.*, vol. 135, no. 1995, 1995.

[101] M. Duocastella and C. B. Arnold, "Bessel and annular beams for materials processing," *Laser Photonics Rev.*, vol. 6, no. 5, pp. 607–621, 2012.

[102] A. Dunn *et al.*, "Applied Surface Science Comment on ' Nanosecond laser textured superhydrophobic metallic surfaces and their chemical sensing applications ' by Duong V . Ta ," *Appl. Surf. Sci.*, vol. 379, pp. 111–113, 2016.

[103] V. D. Ta *et al.*, "Laser textured superhydrophobic surfaces and their applications for homogeneous spot deposition," *Appl. Surf. Sci.*, vol. 365, pp. 153–159, 2016.

[104] R. Jagdheesh and J. L. Ocaña, "One-Step Generation of Ultrahydrophobic Aluminum Surface Patterns by Nanosecond Lasers," *Proceeding LIM*, 2015.

[105] X. Wang, H. Zheng, Y. Wan, W. Feng, and Y. C. Lam, "Picosecond Laser Surface Texturing of a Stavax Steel Substrate for Wettability Control," *Engineering*, vol. 4, no. 6, pp. 816–821, 2018.

[106] Z. Yang, C. Zhu, N. Zheng, D. Le, and J. Zhou, "Superhydrophobic Surface Preparation and Wettability Transition of Titanium Alloy with Micro/Nano Hierarchical Texture," *Materials (Basel).*, vol. 11, no. 11, p. 2210, 2018.

[107] M. V. Rukosuyev, J. Lee, S. J. Cho, G. Lim, and M. B. G. Jun, "One-step fabrication of superhydrophobic hierarchical structures by femtosecond laser ablation," *Appl. Surf. Sci.*, vol. 313, pp. 411–417, 2014.

[108] B. Zheng, W. Wang, G. Jiang, and X. Mei, "Fabrication of broadband antireflective black metal surfaces with ultra-light-trapping structures by picosecond laser texturing and chemical fluorination," *Appl. Phys. B Lasers Opt.*, vol. 122, no. 6, pp. 1–15, 2016.

[109] X. Wang, C. Li, W. Hong, C. Ma, Y. Xing, and J. Feng, "Fabrication of ordered hierarchical structures on stainless steel by picosecond laser for modified wettability applications," *Opt. Express*, vol. 26, no. 15, p. 18998, 2018.

[110] V. Lang, T. Roch, and A. F. Lasagni, "World record in high speed laser surface microstructuring of polymer and steel using direct laser interference patterning," vol. 9736, no. 0, p. 97360Z, 2016.

[111] Y. Nakata, K. Momoo, T. Hiromoto, and N. Miyanaga, "Generation of superfine structure smaller than 10 nm by interfering femtosecond laser processing," *Laser Appl. Microelectron. Optoelectron. Manuf. XVI*, vol. 7920, p. 79200B, 2011.

[112] T. Tavera, N. Pérez, A. Rodríguez, P. Yurrita, S. M. Olaizola, and E. Castaño, "Periodic patterning of silicon by direct nanosecond laser interference ablation," *Appl. Surf. Sci.*, vol. 258, no. 3, pp. 1175–1180, 2011.

[113] A. Rodriguez *et al.*, "Laser interference lithography for nanoscale structuring of materials: From laboratory to industry," *Microelectron. Eng.*, vol. 86, no. 4–6, pp. 937–940, 2009.

[114] M. Bieda, C. Schmädicke, T. Roch, and A. Lasagni, "Ultra-low friction on 100Cr6-steel surfaces after direct laser interference patterning," *Adv. Eng. Mater.*, vol. 17, no. 1, pp. 102–108, 2015.

[115] A. Rosenkranz, T. Heib, C. Gachot, and F. Mücklich, "Oil film lifetime and wear particle analysis of laser-patterned stainless steel surfaces," *Wear*, vol. 334–335, pp. 1–12, 2015.

[116] A. Rosenkranz, M. Hans, C. Gachot, A. Thome, S. Bonk, and F. Mücklich, "Direct Laser Interference Patterning: Tailoring of Contact Area for Frictional and Antibacterial Properties," *Lubricants*, vol. 4, no. 1, p. 2, 2016.

[117] L. Gao *et al.*, "Fabrication of hydrophobic structures on stent by direct three-beam laser interference lithography," *Optik (Stuttg).*, vol. 127, no. 13, pp. 5211–5214, 2016.

[118] B. Raillard, J. Rémond, E. Ramos-Moore, N. Souza, C. Gachot, and F. Mücklich, "Wetting properties of steel surfaces modified by laser interference metallurgy," *Adv. Eng. Mater.*, vol. 15, no. 5, pp. 341–346, 2013.

[119] K. Paivasaari, J. J. J. Kaakkunen, M. Kuittinen, and T. Jaaskelainen, "Enhanced optical absorptance of metals using interferometric femtosecond ablation," *Opt. Express*, vol. 15, no. 21, p. 13838, 2007.

[120] M. Hans, C. Gachot, F. Müller, and F. Mücklich, "Direct laser interference structuring as a tool to gradually tune the wetting response of titanium and polyimide surfaces," *Adv. Eng. Mater.*, vol. 11, no. 10, pp. 795–800, 2009.

[121] S. Heilmann, C. Zwahr, A. Knape, J. Zschetzsche, A. F. Lasagni, and U. Füssel, "Improvement of the Electrical Conductivity between Electrode and Sheet in Spot Welding Process by Direct Laser Interference Patterning," *Adv. Eng. Mater.*, vol. 1700755, pp. 1–8, 2018.

[122] C. Zwahr *et al.*, "Laser Surface Pattering of Titanium for Improving the Biological Performance of Dental Implants," *Adv. Healthc. Mater.*, vol. 6, no. 3, 2017.

[123] A. Lasagni *et al.*, "Bringing the direct laser interference patterning method to industry: A one tool-complete solution for surface functionalization," *J. Laser Micro Nanoeng.*, vol. 10, no. 3, pp. 340–344, 2015.

[124] T. Tamulevičius, M. Ju, T. Klinavičius, and A. Paulauskas, "Dot-Matrix Hologram Rendering Algorithm and its Validation through Direct Laser Interference Patterning," *Sci. reports, Nat.*, vol. 8:14245, pp. 1–11, 2018.

[125] Z. Zhou, Z. Song, L. Li, J. Zhang, and Z. Wang, "Fabrication of periodic variable-sized Pt nanoparticles via laser interference patterning," *Appl. Surf. Sci.*, vol. 335, pp. 65–70, 2015.

[126] D. Yuan *et al.*, "Heteroepitaxial patterned growth of vertically aligned and periodically distributed ZnO nanowires on GaN using laser interference ablation," *Adv. Funct. Mater.*, vol. 20, no. 20, pp. 3484–3489, 2010.

[127] Y. Nakata, N. Miyanaga, K. Momoo, and T. Hiromoto, "Solid-liquid-solid process for forming free-standing gold nanowhisker superlattice by interfering femtosecond laser irradiation," *Appl.*

Surf. Sci., vol. 274, pp. 27–32, 2013.

[128] L. E. Scriven and C. V. Sternling, "The Marangoni Effects," *Nature*, vol. 187, no. 4733, pp. 186–188, 1960.

[129] S. Sharma, Y. Pachaury, S. N. Akhtar, and M. Jabalpur, "A study on hydrodynamics of melt expulsion in pulsed Nd : YAG laser drilling of titanium," *Proc. 2015 COMSOL Conf.*, 2015.

[130] A. Lasagni, M. D'Alessandria, R. Giovanelli, and F. Mücklich, "Advanced design of periodical architectures in bulk metals by means of Laser Interference Metallurgy," *Appl. Surf. Sci.*, vol. 254, no. 4, pp. 930–936, 2007.

[131] M. Bieda, M. Siebold, and A. F. Lasagni, "Fabrication of sub-micron surface structures on copper, stainless steel and titanium using picosecond laser interference patterning," *Appl. Surf. Sci.*, vol. 387, pp. 175–182, 2016.

[132] M. Bieda, E. Beyer, and A. F. Lasagni, "Direct Fabrication of Hierarchical Microstructures on Metals by Means of Direct Laser Interference Patterning," *J. Eng. Mater. Technol.*, vol. 132, no. 3, p. 031015, 2010.

[133] M. Birnbaum, "Semiconductor Surface Damage Produced by Ruby Lasers," *J. Appl. Phys.*, vol. 36, no. 3688, 1965.

[134] S. Gräf and F. A. Müller, "Polarisation-dependent generation of fs-laser induced periodic surface structures," *Appl. Surf. Sci.*, vol. 331, pp. 150–155, 2015.

[135] S. Schwarz, S. Rung, C. Esen, and R. Hellmann, "Homogeneous Low Spatial Frequency LIPSS on Dielectric Materials Generated by Beam-Shaped Femtosecond Pulsed Laser Irradiation," *JLMN-Journal of Laser Micro/Nanoengineering*, vol. 13, no. 2, pp. 90–94, 2018.

[136] N. Tsutsumi, A. Fujihara, and K. Nagata, "Fabrication of laser induced periodic surface structure for geometrical engineering," *Thin Solid Films*, vol. 517, no. 4, pp. 1487–1492, 2008.

[137] J. B. S. Höhm and A. R. J. Krüger, "Sub-100-nm laser-induced periodic surface structures upon irradiation of titanium by Ti : sapphire femtosecond laser pulses in air," pp. 547–551, 2013.

[138] G. R. B. E. Römer, J. Z. P. Skolski, J. V. Oboňa, V. Ocelík, J. T. M. De Hosson, and A. J. Huis In't Veld, "Laser-induced periodic surface structures, modeling, experiments, and applications," *Proc. SPIE - Int. Soc. Opt. Eng.*, vol. 8968, no. c, 2014.

[139] R. A. Ganeev, "Optical Modification of Semiconductor Surfaces Through the Nanoripples Formation Using Ultrashort Laser Pulses : Experimental Aspects," vol. 117, no. 2, pp. 320–340, 2014.

[140] J. Z. P. Skolski, G. R. B. E. Römer, J. Vincenc Obona, and A. J. Huis In 'T Veld, "Modeling laser-induced periodic surface structures: Finite-difference time-domain feedback simulations," *J. Appl. Phys.*, vol. 115, no. 10, 2014.

[141] F. Fraggelakis, G. Mincuzzi, J. Lopez, I. Manek-hönninger, and R. Kling, "Applied Surface Science Controlling 2D laser nano structuring over large area with double femtosecond pulses," *Appl. Surf. Sci.*, vol. 470, no. November 2018, pp. 677–686, 2019.

[142] F. Fraggelakis and J. Lopez, "Generation of micro- and nano-morphologies on femtosecond laser pulses," *RSC Adv.*, vol. 8, no. 29, pp. 16082–16087, 2018.

[143] L. Orazi, I. Gnilitskyi, and A. P. Serro, "Laser Nanopatterning for Wettability Applications," *J. Micro Nano-Manufacturing*, vol. 5, no. 2, p. 021008, 2017.

[144] K. M. Tanvir Ahmmed, C. Grambow, and A. M. Kietzig, "Fabrication of micro/nano structures on metals by femtosecond laser micromachining," *Micromachines*, vol. 5, no. 4, pp. 1219–1253, 2014.

[145] F. Fraggelakis, G. Mincuzzi, J. Lopez, I. Manek-Hönninger, and R. Kling, "Controlling 2D laser nano structuring over large area with double femtosecond pulses," *Appl. Surf. Sci.*, vol. 470, no. November 2018, pp. 677–686, 2019.

[146] E. Skoulas, A. Manousaki, C. Fotakis, and E. Stratakis, "Biomimetic surface structuring using cylindrical vector femtosecond laser beams," *Sci. Rep.*, vol. 7, no. November 2016, pp. 1–11, 2017.

[147] F. Zacharatos *et al.*, "Laser Direct Write micro-fabrication of large area electronics on flexible substrates," *Appl. Surf. Sci.*, vol. 374, pp. 117–123, 2016.

[148] S. Schlie *et al.*, "Laser-based nanoengineering of surface topographies for biomedical applications," *Photonics Nanostructures - Fundam. Appl.*, vol. 9, no. 2, pp. 159–162, 2011.

[149] D. W. Hamilton, K. S. Wong, and D. M. Brunette, "Microfabricated discontinuous-edge surface topographies influence osteoblast adhesion, migration, cytoskeletal organization, and proliferation and enhance matrix and mineral deposition in vitro," *Calcif. Tissue Int.*, vol. 78, no. 5, pp. 314–325, 2006.

[150] D. Arnaldo, D. E. L. Cerro, G. R. B. E. Römer, and A. J. H. I. N. T. Veld, "Picosecond laser machined designed patterns with anti-ice effect," *Lpm*, pp. 9–12, 2010.

[151] M. J. Kreder, J. Alvarenga, P. Kim, and J. Aizenberg, "Design of anti-icing surfaces: Smooth, textured or slippery?," *Nat. Rev. Mater.*, vol. 1, no. 1, 2016.

[152] J. Schille *et al.*, "Highspeed laser micro processing using ultrashort laser pulses," *J. Laser Micro Nanoeng.*, vol. 9, no. 2, pp. 161–168, 2014.

[153] B. Wu, M. Zhou, J. Li, X. Ye, G. Li, and L. Cai, "Superhydrophobic surfaces fabricated by microstructuring of stainless steel using a femtosecond laser," *Appl. Surf. Sci.*, vol. 256, no. 1, pp. 61–66, 2009.

[154] G. Mincuzzi, L. Gemini, M. Faucon, and R. Kling, "Extending ultra-short pulse laser texturing over large area," *Appl. Surf. Sci.*, vol. 386, pp. 65–71, 2016.

[155] U. Loeschner *et al.*, "High-rate laser microprocessing using a polygon scanner system," *J. Laser Appl.*, vol. 27, no. S2, p. S29303, 2015.

[156] L. Penning, "Advanced scanning solutiosn for micromachining," no. 82, pp. 30–32, 2016.

[157] A. J. Meuler, S. S. Chhatre, A. R. Nieves, J. M. Mabry, R. E. Cohen, and G. H. McKinley, "Examination of wettability and surface energy in fluorodecyl POSS/polymer blends," *Soft*

Matter, vol. 7, no. 21, pp. 10122–10134, 2011.

[158] Y. Liu, X. Chen, and J. H. Xin, "Super-hydrophobic surfaces from a simple coating method: A bionic nanoengineering approach," *Nanotechnology*, vol. 17, no. 13, pp. 3259–3263, 2006.

[159] A. Mohammad Rabea, M. Mohseni, H. Yari, and B. Ramezanzadeh, "Fabrication of low surface free energy automotive clear coats: Mechanical and surface chemistry studies," *J. Appl. Polym. Sci.*, vol. 128, no. 6, pp. 4067–4076, 2013.

[160] M. Nosonovsky and B. Bhushan, "Roughness-induced superhydrophobicity: A way to design non-adhesive surfaces," *J. Phys. Condens. Matter*, vol. 20, no. 22, 2008.

[161] X. Fu and X. He, "Fabrication of super-hydrophobic surfaces on aluminum alloy substrates," *Appl. Surf. Sci.*, vol. 255, no. 5 PART 1, pp. 1776–1781, 2008.

[162] J. Drzymala, "Hydrophobicityand collectorless flotation of inorganic materials," *Adv. Colloid Interface Sci.*, vol. 50, no. C, pp. 143–185, 1994.

[163] M. M. Gentleman and J. A. Ruud, "Role of hydroxyls in oxide wettability," *Langmuir*, vol. 26, no. 3, pp. 1408–1411, 2010.

[164] W. Choi, A. Tuteja, S. Chhatre, J. M. Mabry, R. E. Cohen, and G. H. McKinley, "Fabrics with tunable oleophobicity," *Adv. Mater.*, vol. 21, no. 21, pp. 2190–2195, 2009.

[165] N. Verplanck, Y. Coffinier, V. Thomy, and R. Boukherroub, "Wettability switching techniques on superhydrophobic surfaces," *Nanoscale Res. Lett.*, vol. 2, no. 12, pp. 577–596, 2007.

[166] T. Sen Lin, C. F. Wu, and C. Te Hsieh, "Enhancement of water-repellent performance on functional coating by using the Taguchi method," *Surf. Coatings Technol.*, vol. 200, no. 18–19, pp. 5253–5258, 2006.

[167] N. Valipour M., F. C. Birjandi, and J. Sargolzaei, "Super-non-wettable surfaces: A review," *Colloids Surfaces A Physicochem. Eng. Asp.*, vol. 448, no. 1, pp. 93–106, 2014.

[168] X. Fu and X. He, "Fabrication of super-hydrophobic surfaces on aluminum alloy substrates," *Appl. Surf. Sci.*, vol. 255, no. 5 PART 1, pp. 1776–1781, 2008.

[169] L. Afferrante and G. Carbone, "The effect of drop volume and micropillar shape on the apparent contact angle of ordered microstructured surfaces," *Soft Matter*, vol. 10, no. 22, pp. 3906–3914, 2014.

[170] M. Belhadjamor, M. El Mansori, S. Belghith, and S. Mezlini, "Anti-fingerprint properties of engineering surfaces: a review," *Surf. Eng.*, vol. 34, no. 2, pp. 85–120, 2018.

[171] B. Zhang, J. Wang, and X. Zhang, "Effects of the hierarchical structure of rough solid surfaces on the wetting of microdroplets," *Langmuir*, vol. 29, no. 22, pp. 6652–6658, 2013.

[172] T. Koishi, K. Yasuoka, S. Fujikawa, T. Ebisuzaki, and X. C. Zeng, "Coexistence and transition between Cassie and Wenzel state on pillared hydrophobic surface," *Proc. Natl. Acad. Sci.*, vol. 106, no. 21, pp. 8435–8440, 2009.

[173] P. Bizi-Bandoki, S. Valette, E. Audouard, and S. Benayoun, "Time dependency of the hydrophilicity and hydrophobicity of metallic alloys subjected to femtosecond laser

irradiations," *Appl. Surf. Sci.*, vol. 273, pp. 399–407, 2013.

[174] C. Sciancalepore, L. Gemini, L. Romoli, and F. Bondioli, "Study of the wettability behavior of stainless steel surfaces after ultrafast laser texturing," *Surf. Coatings Technol.*, vol. 352, no. July, pp. 370–377, 2018.

[175] J. T. Cardoso *et al.*, "Influence of ambient conditions on the evolution of wettability properties of an IR-, ns-laser textured aluminium alloy," *RSC Adv.*, vol. 7, no. 63, pp. 39617–39627, 2017.

[176] J. Long, M. Zhong, H. Zhang, and P. Fan, "Superhydrophilicity to superhydrophobicity transition of picosecond laser microstructured aluminum in ambient air," *J. Colloid Interface Sci.*, vol. 441, pp. 1–9, 2015.

[177] P. Gregorčič, M. Conradi, L. Hribar, and M. Hočevar, "Long-term influence of laser-processing parameters on (Super)hydrophobicity development and stability of stainless-steel surfaces," *Materials (Basel).*, vol. 11, no. 11, 2018.

[178] A. M. Kietzig, S. G. Hatzikiriakos, and P. Englezos, "Patterned superhydrophobic metallic surfaces," *Langmuir*, vol. 25, no. 8, pp. 4821–4827, 2009.

[179] G. Römer, D. A. del Cerro, R. C. J. Sipkema, M. N. W. Groenendijk, and A. J. Huis in 't Veld, "Ultra Short Pulse Laser Generated Surface Textures for Anti-ice Applications in Aviation," *29th Int. Congr. Appl. Lasers Electro-Optics, ICALEO*, pp. 1356–1360, 2010.

[180] M. Martínez-Calderon, A. Rodríguez, A. Dias-Ponte, M. C. Morant-Miñana, M. Gómez-Aranzadi, and S. M. Olaizola, "Femtosecond laser fabrication of highly hydrophobic stainless steel surface with hierarchical structures fabricated by combining ordered microstructures and LIPSS," *Appl. Surf. Sci.*, vol. 374, pp. 81–89, 2016.

[181] C. V. Ngo and D. M. Chun, "Control of laser-ablated aluminum surface wettability to superhydrophobic or superhydrophilic through simple heat treatment or water boiling post-processing," *Appl. Surf. Sci.*, vol. 435, pp. 974–982, 2018.

[182] Y. Cai, W. Chang, X. Luo, A. M. L. Sousa, K. H. A. Lau, and Y. Qin, "Superhydrophobic structures on 316L stainless steel surfaces machined by nanosecond pulsed laser," *Precis. Eng.*, vol. 52, no. January, pp. 266–275, 2018.

[183] J. Long, M. Zhong, H. Zhang, and P. Fan, "Superhydrophilicity to superhydrophobicity transition of picosecond laser microstructured aluminum in ambient air," *J. Colloid Interface Sci.*, vol. 441, pp. 1–9, 2015.

[184] A. Y. Vorobyev and C. Guo, "Multifunctional surfaces produced by femtosecond laser pulses," *J. Appl. Phys.*, vol. 117, no. 3, 2015.

[185] A. Kietzig and M. N. Mirvakili, "Laser-Patterned Super- Hydrophobic Pure Metallic Substrates : Cassie to Wenzel Wetting Transitions," *J. Adhes. Sci. Technol.*, vol. 25, no. October 2013, pp. 2789–2809, 2011.

[186] M. H. Kwon, H. S. Shin, and C. N. Chu, "Fabrication of a super-hydrophobic surface on metal

using laser ablation and electrodeposition," *Appl. Surf. Sci.*, vol. 288, pp. 222–228, 2014.

[187] V. D. Ta *et al.*, "Laser textured surface gradients," *Appl. Surf. Sci.*, vol. 371, pp. 583–589, 2016.

[188] M. Hans, C. Gachot, F. Müller, and F. Mücklich, "Direct laser interference structuring as a tool to gradually tune the wetting response of titanium and polyimide surfaces," *Adv. Eng. Mater.*, vol. 11, no. 10, pp. 795–800, 2009.

[189] P. H. Wu, C. W. Cheng, C. P. Chang, T. M. Wu, and J. K. Wang, "Fabrication of large-area hydrophobic surfaces with femtosecond-laser- structured molds," *J. Micromechanics Microengineering*, vol. 21, no. 11, 2011.

[190] G. Römer, D. A. del Cerro, R. C. J. Sipkema, M. N. W. Groenendijk, and A. J. Huis in 't Veld, "Ultra short pulse laser generated surface textures for anti-ice applications in aviation," *29th Int. Congr. Appl. Lasers Electro-Optics, ICALEO*, pp. 1356–1360, 2010.

[191] A. M. Kietzig, M. N. Mirvakili, S. Kamal, P. Englezos, and S. G. Hatzikiriakos, "Laser-patterned super-hydrophobic pure metallic substrates: Cassie to Wenzel wetting transitions," *J. Adhes. Sci. Technol.*, vol. 25, no. 20, pp. 2789–2809, 2012.

[192] Y. Cai, W. Chang, X. Luo, A. M. L. Sousa, K. H. A. Lau, and Y. Qin, "Superhydrophobic structures on 316L stainless steel surfaces machined by nanosecond pulsed laser," *Precis. Eng.*, vol. 52, no. October 2017, pp. 266–275, 2018.

[193] J. Schille *et al.*, "Experimental study on laser surface texturing for friction coefficient enhancement," *J. Laser Micro Nanoeng.*, vol. 10, no. 3, pp. 245–253, 2015.

[194] C. Gachot, A. Rosenkranz, S. M. Hsu, and H. L. Costa, "A critical assessment of surface texturing for friction and wear improvement," *Wear*, vol. 372–373, pp. 21–41, 2017.

[195] S. Akbarzadeh and M. M. Khonsari, "Effect of surface pattern on stribeck curve," *Tribol. Lett.*, vol. 37, no. 2, pp. 477–486, 2010.

[196] F. P. Mezzapesa, M. Scaraggi, G. Carbone, D. Sorgente, A. Ancona, and P. M. Lugarà, "Varying the geometry of laser surface microtexturing to enhance the frictional behavior of lubricated steel surfaces," *Phys. Procedia*, vol. 41, pp. 677–682, 2013.

[197] A. Kovalchenko, O. Ajayi, A. Erdemir, G. Fenske, and I. Etsion, "The effect of laser surface texturing on transitions in lubrication regimes during unidirectional sliding contact," *Tribol. Int.*, vol. 38, no. 3, pp. 219–225, 2005.

[198] A. dos Santos *et al.*, "Influence of a Femtosecond Laser Surface Modification on the Fatigue Behavior of Ti-6Al-4V ELI Alloy," *Mater. Res.*, vol. 22, no. 4, 2019.

[199] X. Zhao, H. Zhang, and Y. Liu, "Effect of laser surface remelting on the fatigue crack propagation rate of 40Cr steel," *Results Phys.*, vol. 12, no. December 2018, pp. 424–431, 2019.

[200] D. J. Thomas, "Optimising laser cut-edge durability for steel structures in high stress applications," *J. Constr. Steel Res.*, vol. 121, pp. 40–49, 2016.

[201] D. S. Milovanović, B. B. Radak, B. M. Gaković, D. Batani, M. D. Momčilović, and M. S.

Trtica, "Surface morphology modifications of titanium based implant induced by 40 picosecond laser pulses at 266 nm," *J. Alloys Compd.*, vol. 501, no. 1, pp. 89–92, 2010.

[202] V. N. Moiseyev, *Titanium Alloys: Russian Aircraft and Aerospace Applications*. Florida, Press, 2006.

[203] W. J. Askeland, D.R. Fulay, P. P. Wright, *The science and engineering of materials*, vol. sixth edit. 2010.

[204] J. M. Liu, "Simple technique for measurements of pulsed Gaussian-beam spot sizes," *Optics Letters*, vol. 7, no. 5. p. 196, 1982.

[205] J. Drezet and S. Pellerin, "Modelling the Marangoni convection in laser heat treatment," *J. Phys. IV*, vol. 120, pp. 299–306, 2004.

[206] J. Cheng *et al.*, "Single-pulse drilling study on Au, Al and Ti alloy by using a picosecond laser," *Appl. Phys. A Mater. Sci. Process.*, vol. 95, no. 3, pp. 739–746, 2009.

[207] M. K. Khalaf, H. F. Al-Taay, and D. S. Ali, "Effect of radio frequency magnetron sputtering power on structural and optical properties of Ti6Al4V thin films," *Photonic Sensors*, vol. 7, no. 2, pp. 163–170, 2017.

[208] R. Leach, "Characterisation of areal surface texture," vol. Chapter 2, pp. 15–41, 2013.

[209] J. O. Johansson, "Measuring homogeneity of planar point-patterns by using kurtosis," *Pattern Recognit. Lett.*, vol. 21, no. 13–14, pp. 1149–1156, 2000.

[210] A. Forbes, P. Tomlins, E. Gurdak, M. Illsely, S. James, and E. James, "Methodologies for assessing local surface texture features that are relevant to cell attachment," *J. Mater. Sci. Mater. Med.*, vol. 21, no. 8, pp. 2463–2477, 2010.

[211] M. Wang, L. Xi, and S. Du, "3D surface form error evaluation using high definition metrology," *Precis. Eng.*, vol. 38, no. 1, pp. 230–236, 2014.

[212] C. He, K. Vannahme, and A. Gillner, "High-efficiency sub-micrometer multi-beam interference structuring for large-scale surface using ultrashort laser pulses," *J. Laser Micro Nanoeng.*, vol. 14, no. 1, pp. 95–99, 2019.

[213] *ISO 4287 1997 Geometrical product specifications (GPS)*, no. Surface Texture: Profile Method-Terms, Definitions and Surface Texture Parameters (International Organization for Standardization). 1998.

[214] E. S. Gadelmawla, M. M. Koura, T. M. A. Maksoud, I. M. Elewa, and H. H. Soliman, "Roughness parameters," *J. Mater. Process. Technol.*, vol. 123, no. 1, pp. 133–145, 2002.

[215] P. Westfall H, "Kurtosis as Peakedness, 1905-2014. R.I.P.," vol. 68, no. 3, pp. 191–195, 2014.

[216] M. Vadali, C. Ma, N. A. Duffie, X. Li, and F. E. Pfefferkorn, "Pulsed laser micro polishing: Surface prediction model," *J. Manuf. Process.*, vol. 14, no. 3, pp. 307–315, 2012.

[217] M. G. Bulmer, *Principles of Statistics*. New York: Dover, 1979.

[218] K. P. Balanda and H. L. Macgillivray, "Kurtosis: A critical review," *Am. Stat.*, vol. 42, no. 2, pp. 111–119, 1988.

[219] M. D'Alessandria, A. Lasagni, and F. Mücklich, "Direct micro-patterning of aluminum substrates via laser interference metallurgy," *Appl. Surf. Sci.*, vol. 255, no. 5 PART 2, pp. 3210–3216, 2008.

[220] C. Rainieri and G. Fabbricino, "Operational Modal Analysis of Civil Engineering Structures," no. D, p. 340, 2014.

[221] B. Bhushan, *Wear*. 2013.

[222] K. H. Leitz, B. Redlingshöer, Y. Reg, A. Otto, and M. Schmidt, "Metal ablation with short and ultrashort laser pulses," *Phys. Procedia*, vol. 12, no. PART 2, pp. 230–238, 2011.

[223] "British Standards Institution. Stainless Steels - Part1: List of stainless steels," no. BS EN 100088-1:2005, 2005.

[224] A. Rank, T. Kunze, T. Hoffmann, and A. F. Lasagni, "Direct Laser Interference Patterning of Nickel Molds for Hot Embossing of Polymers," *Adv. Eng. Mater.*, vol. 18, no. 7, pp. 1280–1288, 2016.

[225] J. Reif, O. Varlamova, and F. Costache, "Femtosecond laser induced nanostructure formation: Self-organization control parameters," *Appl. Phys. A Mater. Sci. Process.*, vol. 92, no. 4, pp. 1019–1024, 2008.

[226] N. Yasumaru, K. Miyazaki, and J. Kiuchi, "Femtosecond-laser-induced nanostructure formed on hard thin films of TiN and DLC," *Appl. Phys. A Mater. Sci. Process.*, vol. 76, no. 6, pp. 983–985, 2003.

[227] J. Wang and C. Guo, "Numerical study of ultrafast dynamics of femtosecond laser-induced periodic surface structure formation on noble metals," *J. Appl. Phys.*, vol. 102, no. 5, pp. 1–5, 2007.

[228] C. A. Zuhlke, T. P. Anderson, and D. R. Alexander, "Formation of multiscale surface structures on nickel via above surface growth and below surface growth mechanisms using femtosecond laser pulses," *Opt. Express*, vol. 21, no. 7, p. 8460, 2013.

[229] S. Milles, M. Soldera, B. Voisiat, and A. F. Lasagni, "Fabrication of superhydrophobic and ice-repellent surfaces on pure aluminium using single and multiscaled periodic textures," *Sci. Rep.*, vol. 9, no. 1, pp. 1–13, 2019.

[230] B. Jaeggi, B. Neuenschwander, M. Zimmermann, R. De Loor, and L. Penning, "High throughput ps-laser micro machining with a synchronized polygon line scanner," *8th Int. Conf. Photonic Technol. LANE 2014*, no. c, pp. 1–8, 2014.

[231] E. Hecht, *Optics*. San Francisco: Addison-Wesley, 2002.

[232] Y. Jee, M. F. Becker, and R. M. Walser, "Laser-induced damage on single-crystal metal surfaces," *J. Opt. Soc. Am. B*, vol. 5, no. 3, p. 648, 2008.

[233] G. Raciukaitis, M. Brikas, P. Gecys, and M. Gedvilas, "Accumulation effects in laser ablation of metals with high-repetition-rate lasers," *High-Power Laser Ablation VII*, vol. 7005, p. 70052L, 2008.

[234] D. A. Del Cerro, "Picosecond Pulsed Laser Microstructuring of Metals for Microfluidics," Universtity of Twente, The Netherlands (Doctoral thesis) Retrieved from: http://doc.utwente.nl/91964/., 2014.

[235] N. Cui and N. M. D. Brown, "Modification of the surface properties of a polypropylene of a polypropylene (PP) film using an air dielectric barrier discharge plasma," vol. 189, pp. 31–38, 2002.

[236] L. Gemini, M. Faucon, L. Romoli, and R. Kling, "High throughput laser texturing of super-hydrophobic surfaces on steel," *Laser-based Micro- Nanoprocessing XI*, vol. 10092, no. March 2017, p. 100921G, 2017.

[237] C. V. Ngo and D. M. Chun, "Fast wettability transition from hydrophilic to superhydrophobic laser-textured stainless steel surfaces under low-temperature annealing," *Appl. Surf. Sci.*, vol. 409, pp. 232–240, 2017.

[238] J. Zhang, L. Huang, L. Yu, and P. Zhang, "Synthesis and tribological behaviors of diamond-like carbon films by electrodeposition from solution of acetonitrile and water," vol. 254, pp. 3896–3901, 2008.

[239] J. Long, M. Zhong, P. Fan, D. Gong, and H. Zhang, "Wettability conversion of ultrafast laser structured copper surface," *J. Laser Appl.*, vol. 27, no. S2, p. S29107, 2015.

[240] Z. Li, Y. Zheng, J. Zhao, and L. Cui, "Wettability of atmospheric plasma sprayed Fe, Ni, Cr and their mixture coatings," *J. Therm. Spray Technol.*, vol. 21, no. 2, pp. 255–262, 2012.

[241] J. T. Cardoso *et al.*, "Influence of ambient conditions on the evolution of wettability properties of an IR-, ns-laser textured aluminium alloy," *RSC Adv.*, vol. 7, no. 63, pp. 39617–39627, 2017.

[242] E. Andablo-Reyes, R. Hidalgo-Álvarez, and J. De Vicente, "Controlling friction using magnetic nanofluids," *Soft Matter*, vol. 7, no. 3, pp. 880–883, 2011.

[243] T. Stark, T. Kiedrowski, H. Marschall, and A. F. Lasagni, "Avoiding starvation in tribocontact through active lubricant transport in laser textured surfaces," *Lubricants*, vol. 7, no. 6, pp. 1–18, 2019.

[244] A. F. Lasagni, "Laser interference patterning methods: Possibilities for high-throughput fabrication of periodic surface patterns," *Adv. Opt. Technol.*, vol. 6, no. 3–4, pp. 265–275, 2017.

[245] P. Kossack, "Experimentelle Ermittlung der Ermüdungsfestigkeit von laserstrukturierten Proben aus Ti-6Al-4V inkl . Beobachtung der Schädigungsentwicklung mittels optischer Bildkorrelation," TU Dresden, 2019.

Curriculum Vitae

Alfredo Ismael Aguilar Morales

Birth date and place: **20/06/1986 in Mexico City**

Marital Status: **Married**

Academic training

04/2016 – 04/2021 Dresden, Germany	Ph.D. student Technical University of Dresden. • *Microfabrication and development of multi-scaled metallic surfaces using Direct Laser Interference Patterning.*
07/2013 – 08/2015 Mexico city, Mexico	Master degree in advanced technology (Photonics area) Centre of Research and Technological Innovation CIITEC. IPN. • *Photomechanical ablation effects in laser-obsidian interaction.*
08/2004 – 12/2008 Mexico city, Mexico	Engineering degree in industrial robotics. ESIME UA. IPN.
08/2001 – 07/2004 Mexico city, Mexico	Technician in electrical control systems. CECYT #1. IPN.

Professional experience

09/2020 – Currently Weilheim, Germany	Development engineer at Huawei, WMTC.
04/2016 – 06/2020 Dresden, Germany	Research fellow at Fraunhofer Institute for Material and Beam Technology IWS. Surface material processing by Direct Laser Interference Patterning • *Surfaces properties achieved: superhydrophobicity, anti-icing, friction reduction, decorative effects on large areas, primarily on titanium, aluminium and stainless steel.* • *Optimisation of laser process parameters and optical setups.*
01/2016 – 03/2016 Mexico city, Mexico	Design engineer at Potencia Industrial S.A de C.V. • *Designing by Autocad mechanical parts in electrical motors and generators.*

11/2009 – 11/2012	Process technician at Sanmina Corporation, Plant 3.
Jalisco, Mexico	• *Solution of welding problems in Surface Mounting Technology production lines of microelectronic components.*
	• *Implementation of Lean-Six-Sigma method.*
	• *Design and definition of the necessary tools and methods for assembly during NPI projects. Defining Poka Yokes. Creating documentation of the process assembly*
	• *Experience in High Mix Low Volume and High Volume production.*

03/2009 – 10/2009	Engineering process intern at Sanmina Corporation, Plant 3.
Jalisco, Mexico	• *Update and creation of visual aids.*
	• *Creating deviations and alerts.*

| 01/2004 – 06/2004 | Social service work performed at the subway of Mexico City. |
| Mexico city, Mexico | • *Maintenance of electromechanical workshop systems.* |

Key competencies and skills

Languages:
- English: B2
- German: C1
- Italian: B1
- Spanish: Native

Software skills:
- Minitab (basics certified training)
- Auto cad
- Mechanical desktop
- Matlab
- Origin
- 3D Max studio
- Robot studio
- KUKA Sunrise.Workbench

Others:
- Project management Practical knowledge

Hobbies:
- Fitness training
- Craftsmanship of jewellery

List of publications

Publications in peer-reviewed journals

Aguilar-Morales, A.I., Alamri, S., Voisiat, B., Kunze, T., Lasagni, A. F., "The Role of the Surface Nano-Roughness on the Wettability Performance of Microstructured Metallic Surface Using Direct Laser Interference Patterning," *Materials*, 12, 2737, pp. 1–14, 2019.

Aguilar Morales, A.I., Alamri, S., Kunze, T., Lasagni, A. F., "Influence of processing parameters on surface texture homogeneity using Direct Laser Interference Patterning," *Opt Laser Technol*, 107, pp. 216- 227, 2018.

Aguilar-Morales, A.I., Alamri, S., Lasagni, A. F., "Micro-fabrication of high aspect ratio periodic structures on stainless steel by picosecond direct laser interference patterning," *J Mater Process Tech* 252, pp. 313-321, 2018.

Alamri, S., Vercillo, V., Aguilar-Morales, A.I., Schell, F., Wetterwald, M., Lasagni, A. F., Bonaccurso, E., Kunze, T., "Self-Limited ice formation and efficient de-icing on superhydrophobic micro-structured aurfoils through Direct Laser Interference Patterning," *Adv. Mat. Interfaces*, 7, 2001231, 2020.

Voisiat, B., Aguilar-Morales, A.I., Kunze, T., Lasagni, A. F., "Development of an analytical model for optimization of Direct Laser Interference Patterning," *Materials,* 13, 200, pp. 1 – 10, 2019.

Vercillo, V., Tonnicchia, S., Romano, J-M, Garcia-Girón, A. Aguilar-Morales, A.I., Alamri, S., Dimov, S.S., Kunze, T., Lasagni, A. F., Bonaccurso, E., "Design Rules for Laser-treated Icephobic Metallic Surfaces for Aeronautic Applications," *Adv Func Mat.* 1910268, 2020.

Stark, T., Alamri, S., Aguilar-Morales, A. I., Kiedrowski, T., Lasagni, A. F., "Positive effect of laser structured surfaces on tribological performance," *J Laser Micro/Nanoen,* 14, pp.13-18, 2019.

Alamri, S., El-Khoury, M., Aguilar-Morales, A. I., Kunze, T., Lasagni, A. F., "Fabrication of inclined non-symmetrical periodic micro-structures using Direct Laser Interference Patterning," *Sci Rep,* 9, 5455, 2019.

Cardoso J.T., Aguilar-Morales, A.I., Alamri, S., Huerta-Murillo, D., Cordovilla, F., Lasagni, A.F., Ocaña, J.L., "Superhydrophobicity on hierarchical periodic surface structures fabricated via direct laser writing and direct laser interference patterning on an aluminium alloy," *Opt Laser Eng,* 111, pp. 193–200, 2018.

Lasagni, A.F., Alamri, S., Aguilar-Morales, A. I., Rößler, F., Voisiat, B., Kunze, T., "Biomimetic surface structuring using laser based interferometric methods," *Appl Sci-basel,* 8, 1260, pp. 1-14, 2018.

Alamri, S., Aguilar-Morales, A. I., Lasagni, A. F., "Controlling the wettability of polycarbonate substrates by producing hierarchical structures using Direct Laser Interference Patterning," *European Journal of Polymers,* 99, pp. 27–37, 2018.

Huerta-Murillo, D., Aguilar-Morales, A.I., Alamri, S., Cardoso, J.T., Jagdheesh, R., Lasagni, A. F., Ocaña J. L., "Fabrication of multi-scale periodic surface structures on Ti-6Al-4V by direct laser writing and direct laser interference patterning for modified wettability applications," *Opt Laser Eng,* 98, pp. 134–142, 2017.

Publications in proceedings

Aguilar-Morales, A.I., Alamri, S., Lasagni, A.F., "Homogeneously distributed microstructures produced by Direct Laser Interference Patterning," in Proceedings of 19th International Symposium on Laser Precision Microfabrication (UK), 1-5, 2018.

Alamri, S., Krupop, B., Steege, T., Aguilar-Morales, A.I., Lang, V., Storm, S., Schell, F., Zwahr, C., Kracht, C., Bieda, M., Voisiat, B., Klotzbach, U., Lasagni, A.F., Kunze T., "Quo Vadis surface functionalization: How direct laser interference patterning tackle productivity and flexibility in industrial applications," Proc. SPIE 10906, Laser-based Micro- and Nanoprocessing XIII, 109060S 2019.

Lasagni, A. F., Aguilar Morales, A. I., Zwahr, C. Rößler, F. Alamri, S. Lang, V. Rank, A. Kunze, T., "High-speed surface structuring using Direct Laser Interference Patterning – fundamentals, applications and technology transfer," in Proc. of LPM2017 - the 18th International Symposium on Laser Precision Microfabrication, 17-01, 1-7, 2017.

Kunze, T., Krupop, B., Alamri, S., Steege, T., Aguilar-Morales, A.I., Trautewig, S., Rößler, F., Lasagni, A.F., "Enhancing surface functionalities by Direct Laser Interference Patterning – Basic principles, industrial approaches and structure lifetime," in Proceedings of 19th International Symposium on Laser Precision Microfabrication (UK), 1-4, 2018.

Alamri, S., Aguilar-Morales, A. I., Lasagni, A. F., "Advanced micro-structuring strategies on polymers using Direct Laser Interference Patterning," in Proceedings of 19th International Symposium on Laser Precision Microfabrication (UK), 1-6, 2018.

Lasagni, A.F., Voisiat, B., Lang, V., Rank, A., Rößler, F., Günther, K., Günther, D., Zwahr, C., Krupop, B., Alamri, S., Steege, T., Aguilar-Morales, A. I., Kunze, T., "Direct Laser Interference Patterning: new possibilities for surface functionalization at high throughputs," in proceedings of Procédés Laser pour L'industrie (JNPLI 2018), 39-44.

Stark, T., Alamri, S., Aguilar-Morales, A. I., Kiedrowski, T., Lasagni, A. F., "Positive effect of laser structured surfaces on tribological performance," in Proceedings of 19th International Symposium on Laser Precision Microfabrication (UK), 1-6, 2018.

Scientific Talks

Aguilar-Morales, A. I., Lasagni, A. F., Fabrication of pillar-like microstructures on stainless steel by picosecond direct laser interference patterning, Euromat 2017, September 2017, Thessaloniki, Greece.

Aguilar-Morales, A. I., Alamri, S., Lasagni, A.F., Homogeneously distributed microstructures produced by Direct Laser Interference Patterning, 19th International Symposium on Laser Precision Microfabrication, June 2018, Edinburgh, Scotland (UK).

Scientific posters

Aguilar-Morales, A. I., Lasagni, A. F., High speed IR-VIS-Direct Laser Interference Patterning of metallic surfaces using pico- and nanosecond laser pulses, 2nd. Annual meeting L4Fun, October 2017, Zaragoza, Spain.

Aguilar-Morales, A. I., Alamri, S., Klotzbach, U., Lasagni, A. F., Mimicking natural superhydrophobic microstructures on Stainless Steel by Picosecond Direct Laser Interference Patterning, 10. Internationales Laser- und Fügesymposium, February 2018, Dresden, Germany.